UNIVERSITY OF OKLAHOMA

GRADUATE COLLEGE

ASSESSING DUAL-DOPPLER VERTICAL VELOCITY RETRIEVALS FROM RAPID-SCAN RADAR DATA

A DISSERTATION

SUBMITTED TO THE GRADUATE FACULTY

in partial fulfillment of the requirements for the

Degree of

DOCTOR OF PHILOSOPHY

By

JOSHUA GREGORY GEBAUER
Norman, Oklahoma
2020

ASSESSING DUAL-DOPPLER VERTICAL VELOCITY RETRIEVALS FROM RAPID-SCAN RADAR DATA

A DISSERTATION APPROVED FOR THE
SCHOOL OF METEOROLOGY

BY THE COMMITTEE CONSISTING OF

Dr. Alan Shapiro, Chair
Dr. Corey Potvin, Co-Chair
Dr. Cameron Homeyer
Dr. Robert Palmer
Dr. Nikola Petrov

Dedication

To Kathryn, we did it.

Acknowledgments

This dissertation has been made possible due to the help of many people. I would first like to thank my advisor Dr. Alan Shapiro who has helped me grow as a scientist over the last five and half years. He has always given me space to make this work my own, and also continued to support my work on a very different topic from my Master's thesis. His grillmaster skills also ensured that I never went hungry during my time in grad school.

I also want to thank Dr. Corey Potvin for being the co-chair for my doctoral committee. He has been an invaluable resource on the analysis techniques used in this dissertation and has been very helpful. I also appreciate Dr. Cameron Homeyer, Dr. Robert Palmer, and Dr. Nikola Petrov for being part of my doctoral committee.

I am incredibly grateful for the radars that the Advanced Radar Research Center (ARRC) provided for this work. Our initial data collection plan fell through and the ARRC radars saved this research. Additionally, thank you to Dr. Mike Biggerstaff for allowing us to use the SMART-R3 for the verification data source. Andrew Mahre, Casey Griffin, David Bodine, Addison Alford, Nathan Dahl, and Gordon Carrie all volunteered to help collect the data used in this dissertation. Many also helped with an unsuccessful data collection attempt that involved staying up all night and sitting at a gas station parking lot off Interstate 35 in northern Oklahoma while we waited for an MCS to come into range for data collection. This MCS decayed before we could collect data, and then we were all sprayed with pesticides that a local farmer was applying to his field close to our deployment site. Despite this disastrous data collection attempt, everyone volunteered again and we were able to collect the dataset seen in this dissertation. I am forever indebted to these people. Andrew Mahre also processed the collected AIR data, and Nathan Dahl was helpful in many discussions on the DDA results. I also want to thank Zach Weinhoff for his insights into the RaXPol jitter problem.

During my time in graduate school, I have grown to appreciate my undergraduate education at California University of Pennsylvania. The professors in the meteorology program, Dr. Chad Kauffman, Dr. Swarn Gill, and Dr. Mario Majcen, were instrumental in preparing me for graduate school. They provided me with an excellent foundation in meteorology and at no time did I fell unprepared for anything I encountered in my graduate studies.

There are many people who have supported me during my time in graduate school. First and foremost, I need to thank my parents Greg and Dana Gebauer, for all of their love and support. They have always supported my goals and have helped me achieve them. Tyler Bell, Katie Bell, Matt Flournoy, Kenzie Krocak, and Eric Loken have all been great friends during my time at OU. I am incredibly grateful for their friendship and they have helped to reduce stress during this long process. Elizabeth Smith and Chris Riedel have been invaluable friends throughout the years. I have known Elizabeth since my time at California University of Pennsylvania and she has helped me numerous times as both a valued colleague and a trusted friend. Chris shares my interest in sports and has helped me expand my taste in craft beer. He was also extremely helpful with the EnKF portion of this work. Both Elizabeth and Chris helped me get through some very difficult times during the last few months of writing my dissertation. Without their friendship there is no way I could have completed this dissertation.

Finally, I need to thank the most important person in my life, my wife Kathryn. She used her excellent editing skills to help me proofread this entire dissertation (almost every hyphen and dash in this document was added after her extensive proofreading), and her support and love have been unwavering during my entire graduate education. I am very lucky to have her in my life.

Table of Contents

List of Tables

List of Figures

Abstract

Vertical velocity is the most difficult wind component to accurately retrieve from dual-Doppler observations. Typical radar scans are conducted with shallow elevation angles and therefore, the radial velocity observations poorly constrain the vertical velocity in retrievals. Traditional dual-Doppler analysis (DDA) uses the anelastic mass conservation equation as a constraint to retrieve vertical velocity. However, procedures that integrate the anelastic mass conservation equation can have large errors in the vertical velocities due to missing low-level data, errors in boundary specification, and the compounding of horizontal divergence errors in the integration. In recent years, it has been proposed to use a vertical vorticity equation as a weak constraint in addition to the mass conservation equation in order to improve vertical velocity retrievals. Prior observation simulation experiments have found that the vorticity equation constraint can improve vertical velocity retrievals in situations with missing low-level data and radar volume scan times that are sufficiently short to calculate the vorticity tendency accurately.

In this study, the vertical vorticity equation constraint DDA was tested using real observations from rapid-scan radars. A dual-Doppler dataset of a convective storm was collected on 4 Sept 2018 with a maximum volume scan time of 30 seconds. An additional radar was positioned under the storm and conducted near-vertical planned-position indicator scans (PPIs), which were used as a verification dataset. In general, the vorticity equation DDA was able to improve vertical velocity retrievels, but the improvement was dependent on the time between volume scans and the technique used to calculate the vorticity tendency. When the time between volume scans was 30 seconds, a simple centered difference of the vorticity calculated from provisional wind retrievals was sufficient for estimating the vorticity tendency, but with greater time between volume scans this method resulted in significantly degraded vertical velocities. A technique that used advection correction to shorten the time difference in the centered difference improved the vertical velocities of these longer volume scan times, but caused the DDAs with 30 seconds between volume

scans to become slightly worse. A new three-dimensional advection correction technique that was developed for the vorticity tendency estimation produced slightly better vertical velocity retrievals than those that used two-dimensional advection correction. One key difference between these results and those of the prior OSSE experiments is that the improvement in the retrieved vertical velocities occurred even though there was not a large data void between the lowest data level and the ground. Additionally, the vorticity equation constraint DDA was more forgiving to radar data errors as it did not produce unphysical vertical velocities in a region of sidelobe contamination that was present in the other DDAs. Considering that observation errors are a common occurrence in radar datasets, these results suggest that the vorticity equation constrained DDA could be more beneficial than what the original OSSE studies indicated.

Another analysis technique that has gained popularity in recent years is ensemble Kalman filter (EnKF) analysis. Prior OSSEs have suggested that EnKF analyses can be more accurate than DDAs. Unfortunately, in this study the EnKF analyses were hampered by catastrophic filter divergence. The adaptive inflation that was used to maintain ensemble spread due to the large number of radial velocity observations being assimilated caused large ensemble spread to develop in data sparse regions, which led to extremely large analysis increments through correlations with regions that had radial velocity observations. Despite the catastrophic filter divergence, EnKF analyses that used radar observations that were thinned to 150-s intervals produced vertical velocities that had better verification statistics than the best DDA. This indicates that if the filter divergence issue is controlled, EnKF analyses could have more accurate vertical velocities than those obtained by DDA.

Most importantly, the results shown in this dissertation highlight that rapid-scan radar data is beneficial to vertical velocity retrievals when that data is paired with a vorticity equation constrained DDA. This DDA technique and the use of rapid-scan radars should be prioritized in future observational studies of convective storms.

Chapter 1

Introduction

1.1 Radar Meteorology Background

Doppler radar has been, and continues to be, a vital tool for research and operational meteorology. Radars are active sensors that transmit pulses of electromagnetic radiation and receive the radiation that is scattered back to the receiver. For weather radar, the scatterers are typically cloud particles and precipitation, but weather radars can also observe clear air returns such as insects and Bragg scatter and these clear air returns have also been used for meteorological applications (e.g. Lhermitte 1966; Klazura and Imy 1993; Banghoff et al. 2018). Most radars used for meteorology are monostatic radars, which have collocated transmitters and receivers, though bistatic radars, where the transmitter and receivers are at separate locations have also been used for meteorological applications.

From the power returned to the radar and using radar constants, the radar obtains radar reflectivity. Weather radars typically have a wavelength large enough that the scattering from cloud particles and precipitation occurs in the Rayleigh regime. Thus radar reflectivity is given by

$$\eta = \frac{|K|^2\pi^5}{\lambda^4}Z, \tag{1.1}$$

where K is the dielectric factor, λ is the radar wavelength, and Z is radar reflectivity factor defined as

$$Z = \int_0^\infty N(D)D^6 dD, \tag{1.2}$$

where $N(D)$ is the drop size distribution and D is the drop diameter. The dielectric factor depends on the phase of scatterers and the phase is not known, so equivalent radar reflectivity factor,

$$Z_e = \frac{\eta\lambda^4}{0.93\pi^5}, \tag{1.3}$$

is the variable calculated from radar reflectivity. Equivalent radar reflectivity factor, expressed in the logrithmic units of decibels relative to Z (dBZ), is the most commonly used radar variable and is often referred to as reflectivity (from this point on, reflectivity will be used to refer to equivalent radar reflectivity factor). Since reflectivity is related to the size and concentration of the scatterers, reflectivity can be used as a measure of precipitation intensity. Doppler radars are also able to measure the velocity of scatterers through the phase shift in the backscattered radiation caused by the Doppler effect. The velocity component measured by the radar, called radial velocity, is the component of the scatterer's velocity that is parallel to the the radar beam. Considering that the horizontal movement of cloud particles and precipitation is due to wind, radial velocities provide information on the kinematics of the atmosphere. For operational meteorology the observations provided by radars are crucial for nowcasting hazardous weather phenomena such as flash flooding, severe thunderstorms, and tornadoes. In fact, current radar networks have been credited with reducing casualties associated with these phenomena (Simmons and Sutter 2005; Cho and Kurdzo 2019, 2020).

Radars have also been used as an atmospheric reasearch tool for over 70 years and have been critical in improving our understanding of the atmosphere, particularly severe convective storms (Brooks et al. 2018). Observations from radars have provided crucial insights into the kinematics of ordinary convection (Mahoney 1988; Lang and Rutledge 2002), squall lines (Rasmussen and Rutledge 1993; Biggerstaff and Houze 1993; Conrad and Knupp 2019), supercells (Browning 1964; Brandes et al. 1988; Kosiba et al. 2013), and hurricanes (Kosiba and Wurman 2014; Alford et al. 2019). Since radars only observe radial velocity, the full three-dimensional wind field is often obtained through some type of retrieval that uses the radial velocities as a constraint. Wind retrievals have been developed for observations from a single radar (Sun and Crook 1994, 2001; Laroche and Zawadzki 1995; Rasmussen and Rutledge 1995; Shapiro et al. 2003; Gao et al. 2001), but these retrievals are prone to errors since radial velocities from a single radar poorly constrain retrieved wind fields. For this reason, most studies that retrieve wind fields from radar data make use of observations from at least two radars at different locations using a technique called dual-Doppler analysis (DDA). More recently, wind fields have been obtained by assimilating radar observations with model forecasts using an ensemble Kalman filter (EnKF). This dissertation focuses on wind retrievals using dual-Doppler analysis and the EnKF.

1.2 Dual-Doppler Analysis

One of the first studies to develop a three-dimensional wind retrieval from radar data was Armijo (1969). Armijo (1969) used data constraints from the radial velocities of multiple radars and the anelastic mass conservation equation in a cylindrical coordinate system (later named the Coplane system) to explicitly solve for the three-dimensional wind field. Later, Brandes (1977) abandoned the cylindrical coordinate system to solve for the wind components using the same constraints as Armijo (1969), but iteratively on a Cartesian grid. This approach gained popularity and was widely used (e.g. Ray et al. 1980; Dowell and Bluestein 1997; Markowski et al. 2012), as this technique does not require the retrieved wind field to be interpolated back to a Cartesian grid. However, it was later shown that the iterative procedure on a Cartesian grid may not always converge (Dowell and Shapiro 2003).

As long as radar cross-beam angles are adequately large, these dual-Doppler retrievals can obtain the horizontal wind components with sufficient accuracy for kinematic analysis, but errors in retrieved vertical velocity can be large (Doviak et al. 1976; Ray and Wagner 1976; Nelson and Brown 1987; Matejka and Bartels 1998; Potvin et al. 2012a). Typical radar scans poorly sample the vertical component of motion since the radar elevation angles are small. The retrieved horizontal wind components are well constrained by the radial velocity constraints when radar cross-beam angles are sufficient for dual-Doppler analysis, but the vertical component is poorly constrained by the observations and has a strong dependence on the anelastic mass conservation equation. Since vertical integration of the mass conservation equation is often used to solve for vertical velocity, errors in the horizontal wind fields accumulate with height when integrating upward, resulting in vertical velocity retrievals degrading with height (Ray et al. 1980). Errors in the integration of the mass conservation equation also come from boundary specification. The impermeability condition ($w = 0$ on a horizontal flat surface) is the simplest boundary condition to impose, however, radar datasets often have missing low-level data due to scan geometry, ground clutter, and the Earth's curvature. When data does not extend down to ground level, large errors can occur if the impermeability condition is applied, as a significant portion of the horizontal wind convergence or divergence in the column could be neglected. One method used to mitigate the effects of missing low-level data is to set the divergence in the data void to some fraction of the divergence at the lowest level with data (Brandes 1977). This fraction is arbitrary and may not be representative of the divergence in the data void. Another technique to overcome missing low-level data is to set vertical velocity to zero at the storm top and integrate downward. Ray et al. (1980) show theoretically that downward integration accumulates less error than upward integration due to density decreasing with height, but also state that this may not be true if the upper boundary condition is not accurate. Radar scans often do not reach storm top and even if they do the assumption that vertical velocity is zero may not be valid. Some techniques set both an upper and lower boundary condition when solving for vertical velocity (O'Brien 1970; Ray et al. 1980; Protat and Zawadzki 1999). These techniques can be more successful, but problems with boundary conditions and error accumulation are still an issue (Potvin et al. 2012a).

Other dual-Doppler retrievals use variational techniques with weak constraints to obtain the wind field. A weak constraint is one where the constraint is imposed in a least-squares error sense (Sasaki 1970). Protat and Zawadzki (1999) applied a weak observational constraint to solve for the horizontal wind components and then used the horizontal winds to integrate the mass conservation equation to obtain vertical velocity. While the Protat and Zawadzki (1999) technique used some variational aspects, it was not a full variational retrieval as the mass conservation equation was still integrated. An example of a fully variational retrieval would be the one used by Gao et al. (1999). For this technique, observational, mass conservation, background, and smoothness constraints are all applied as weak constraints in order to retrieve the wind field. The main benefit of this type of dual-Doppler retrieval is that the mass conservation equation is not explicitly integrated, and therefore vertically compounding errors and errors from boundary-condition specification can be mitigated. It has been shown in observation simulation system experiments (OSSEs) that variational dual-Doppler techniques outperform dual-Doppler techniques that require integration of the mass conservation equation (Potvin et al. 2012a).

Another benefit of the weak-constraint variational approach is non-typical retrieval constraints are easier to implement since the constraint does not have to be fully realized. An example would be using a vertical vorticity equation,

$$\frac{\partial \zeta}{\partial t} + u\frac{\partial \zeta}{\partial x} + v\frac{\partial \zeta}{\partial y} + w\frac{\partial \zeta}{\partial z} + \left(\frac{\partial v}{\partial z}\frac{\partial w}{\partial x} - \frac{\partial u}{\partial z}\frac{\partial w}{\partial y}\right) + \zeta\left(\frac{\partial u}{\partial x} + \frac{\partial v}{\partial y}\right) = 0, \tag{1.4}$$

where $\zeta = \partial v/\partial x - \partial u/\partial y$ is vertical vorticity, and u, v, and w are the x, y, and z components of velocity, respectively. The vertical vorticity constraint has shown promise in improving vertical velocity retrievals. Equation 1.4, like the mass conservation equation, connects vertical velocity to the horizontal wind fields. Mewes and Shapiro (2002) used an anelastic vertical vorticity equation as a weak constraint to solve for vertical velocity boundary conditions. The vertical vorticity constraint was also used by Shapiro et al. (2009) as a weak constraint in a variational procedure similar to the one used by Gao et al. (1999).

One difficulty with using a vertical vorticity constraint in dual-Doppler retrievals is the calculation of the vorticity tendency (the first term in Eq. 1.4). The vertical vorticity tendency has been calculated several ways. The simplest approach is to calculate the tendency from two or more consecutive provisional retrievals of u and v. This approach, however, can lead to large errors when the volume scan time of the radar is long due to translation and evolution of the vorticity field. Shapiro et al. (2009) suggested using pattern translation components of the radar field to account for the translation of the vertical vorticity field, but this technique cannot account for the evolution of vertical vorticity. Expanding on the technique used by Shapiro et al. (2009), Potvin et al. (2012b) used spatially variable pattern translation components computed from the spatially variable advection correction technique developed by Shapiro et al. (2010) to estimate the translational component of the vorticity tendency, and attempted to account for evolution by calculating the vorticity tendency from provisional dual-Doppler retrievals in a moving reference frame. However, accounting for evolution in this manner only slightly improved retrievals when the time between volume scans was short and degraded the analyses when volume scan times exceeded 5 minutes. More recently, Dahl et al. (2019) calculated the vertical vorticity tendency using a centered difference of provisional retrievals from consecutive volume scans, but used the Shapiro et al. (2010) spatially variable advection correction technique on the provisional wind retrievals before and after the analysis time to spatially shift the wind fields to their positions at times closer to the analysis time to reduce the time step in the centered difference.

A consistent theme from dual-Doppler retrieval studies that have used a vertical vorticity constraint is that the constraint improves vertical velocity retrievals when the time between radar volume scans is relatively small. At longer volume scan times, the benefit of the vertical vorticity constraint is reduced and the constraint can even degrade the analyses as it becomes more difficult to accurately estimate the vertical vorticity tendency. Additionally, the improvements when using a vorticity constraint are more pronounced when there is missing low-level data or when low-reflectivity regions are excluded (Shapiro et al. 2009; Potvin et al. 2012b). Potvin et al. (2012b) found that the vorticity constraint provided benefits for volume scan times extending out to 5 minutes, but more recently, Dahl et al.

(2019) indicated that 30-second volume scan times may be needed for the vorticity constraint dual-Doppler technique to improve vertical velocity retrievals. One limitation of the previously mentioned vertical vorticity constraint dual-Doppler studies is that they were primarily OSSEs, so the variational dual-Doppler technique that uses a vertical vorticity constraint has not previously been tested using actual observations from a rapid-scan radar to determine if the OSSE results apply to real data cases.

1.3 Ensemble Kalman Filter

With the increase in computing power and resources, EnKF data assimilation (Evensen 1994) has been used more frequently for radar-data wind retrievals. Data assimilation operates on the premise that a background analysis (typically a model forecast) has some amount of error, while observations themselves are not dense enough to fully capture the atmospheric state and also have errors. The optimal analysis (i.e., the one closest to the truth) will be somewhere in between the background analysis and observations. The closeness of the final analysis to the background or observations depends on the relative errors of the background and observations. In data assimilation, the errors in the background are represented by the background error covariance. The background error covariance enables one type of observation at one location to update all variables and points in the background state that have a non-zero error covariance with the background value at the observation location. In a 3DVAR data assimilation approach, the background error covariance is prescribed and static (Johnson et al. 2015), so it is difficult to obtain realistic covariances. In EnKF data assimilation, the background error covariance is calculated from an ensemble of perturbed model forecasts. Therefore, background error covariances in EnKF data assimilation are flow dependent and cross-variable, and the covariances that develop are more physically meaningful as long as the ensemble size is large enough. These flow-dependent and cross-variable background error covariances are necessary for accurate convective-scale analyses (Johnson et al. 2015).

Initial studies on EnKF radar data assimilation focused on assimilating radial velocity from radars, as this is the easier observation to assimilate (versus reflectivity) since the wind components forecast by the model are used to calculate radial velocity from the background (Snyder and Zhang 2003; Zhang et al. 2004). Reflectivity is more difficult to assimilate as model reflectivity has to be calculated using variables from cloud physics parameterizations, which can vary in their accuracy and complexity. Additionally, reflectivity is nonlinearly related to the model state, which violates the assumptions that underpin EnKF data assimilation (Dowell et al. 2011). Nevertheless, several studies have assimilated both radial velocity and reflectivity observations with success (Aksoy et al. 2009; Snook et al. 2011; Jung et al. 2012; Tanamachi et al. 2013, 2014; Skinner et al. 2015).

One advantage of EnKF analyses over dual-Doppler retrievals is that the thermodynamic variables are inherently part of the retrieval. Thermodymamic retrievals from dual-Doppler analyses (Gal-Chen 1978; Hane et al. 1981) can have significant errors due to the difficulties with obtaining accurate vertical velocities, while the thermodynamic variables retrieved with EnKF data assimilation are constrained by the model forecast. EnKF retrievals can handle missing low-level data more gracefully than dual-Doppler retrievals. Even in cases of missing low-level data, upper-level observations may update the low levels due to the background error covariances, and errors due to boundary specification are completely avoided. EnKF analyses can also easily incorporate observations from other data sources, such as surface mesonet stations, which can be used to improve the analyses in regions where radar data may be unavailable. Despite the potential benefits of EnKF analyses, the accuracy of EnKF analysis is affected by several factors such as model errors, inaccurate forward operators, correlated observation errors, and other situations that violate the optimality conditions of the EnKF. Potvin and Wicker (2012) compared 3DVAR dual-Doppler retrievals to EnKF wind analyses and found that when radar cross-beam angles were sufficient, dual-Doppler retrievals produced better low-level wind retrievals, but the EnKF analyses were more accurate in mid- and upper levels of the storm and at low-levels with poor cross-beam angles. This was true even when observations from only one radar were assimilated. However, Potvin and Wicker (2012) did not use a vorticity constraint in their dual-Doppler retrievals, so it is unknown if EnKF retrievals with rapid-scan data are better than dual-Doppler retrievals with rapid-scan radar data and a vertical vorticity constraint. EnKF retrievals are also significantly more computationally expensive than dual-Doppler retrievals so it remains pertinent to determine if EnKF analyses are worth the additional time and computer resources.

1.4 Research Questions

While prior OSSE studies were important first steps in evaluating the DDA and EnKF retrievals, real-data tests are needed. For example, the OSSE studies may not include representative observation errors that are common in radar datasets, and these errors may significantly affect the accuracy of the wind retrievals. These potential effects can only be addressed by using real rapid-scan data. Up until now, testing the vertical vorticity constraint dual-Doppler retrieval and the EnKF retrievals with rapid-scan radar data has not occurred as rapid-scan dual-Doppler datasets have not been available. Advances in weather radar technology have made rapid-scan radars more common, and it is now possible to easily collect rapid-scan dual-Doppler datasets. The results of such real-data tests can significantly affect the design of future meteorological studies. Observational field projects are often quite costly, so it is important to maximize the quality of the data that is collected on these projects. If rapid-scan radar data can improve wind retrievals then there is reason to prioritize rapid-scanning radars in project design of appropriate field experiments. Additionally, positive results with rapid-scan radar data can be used as motivation to continue the development and construction of rapid-scan radars.

Even with rapid-scan radars, estimation of the vertical vorticity tendency in dual-Doppler retrievals is a difficult problem. Ideally, the vorticity tendency estimation in retrievals can be improved so that the benefits of using a vorticity constraint can be realized with even non-rapid-scanning radars. There are many dual-Doppler datasets that have been collected with radars without rapid-scan capabilities. If the vorticity constraint dual-Doppler technique can be improved for radar datasets with longer volume scan times, then it may be possible to leverage older datasets to improve our understanding of many atmospheric phenomena.

Ultimately, this dissertation aims to use rapid-scan radar data to answer the following questions:

1. Do the results of the OSSEs of the vorticity constraint dual-Doppler retrieval hold up when using real, rapid-scan radar data?
2. Can estimation of the vorticity tendency be improved for longer volume scan times by improving upon the vorticity tendency estimation technique used by Dahl et al. (2019)?
3. Is EnKF-analysis quality affected by using rapid-scan radar data?
4. Do EnKF or dual-Doppler retrievals produce better wind analyses — particularly focusing on the vertical velocity component — and does this depend on the radar volume scan time?

Chapter 2 discusses the radar used, the data collection, meteorological conditions on the day of data collection, and quality control of the dataset. In Chapter 3, the three-dimensional advection correction technique used when estimating the vorticity tendency is presented. The dual-Doppler technique and the results of the DDA tests are shown in Chapter 4. The EnKF tests are discussed in Chapter 5, and finally, conclusions are presented in Chapter 6.

Chapter 2

Data Collection and Quality Control

2.1 Radar Instrumentation

In order to test if the DDA technique used in the Dahl et al. (2019) OSSE study produces similar results with real data, the radars used for data collection needed to collect a full volume of data in at most thirty seconds. Two radars from the Advanced Radar Research Center (ARRC) — the rapid-scanning, X-band, polarimetric radar (RaXPol; Pazmany et al. 2013) and the Atmospheric Imaging Radar (AIR; Isom et al. 2013; Kurdzo et al. 2017) — meet this requirement and were used to collect the dual-Doppler dataset for this study. RaXPol is capable of collecting a 360° azimuth scan in 2 seconds. Due to the mechanical rapid-scanning, RaXPol employs frequency hopping (Girardin-Gondeau et al. 1991; Doviak and Zrnić 1993) to obtain sufficiently independent samples with the short dwell times. Another impact of the rapid-scanning is beam smearing. RaXPol has a beamwidth of 1°, but the rapid-scanning increases the effective beamwidth to $\sim$1.5°. Since development, RaxPol has been used largely for studying supercells and tornadoes (e.g., Bluestein et al. 2015, 2018; Houser et al. 2016) and has been used before in a dual-Doppler analysis (Wienhoff et al. 2018). For more information on RaXPol see Pazmany et al. (2013).

The AIR is a rather unique rapid-scan radar. As an imaging radar, the AIR transmits a $20^\circ \times 1^\circ$ beam and receives using a 36-element array to collect 36 simultaneous channels of receive data (Kurdzo et al. 2017). In post-processing, digital beamforming is performed to obtain 20 $1^\circ \times 1^\circ$ beams in the vertical. Since the AIR obtains data in the vertical simultaneously, mechanical steering of the array in azimuth allows the radar to rapidly collect a volume of data. The AIR is capable of collecting $20^\circ \times 180^\circ$ volume of data in 9 seconds. However, the scanning technique used by the AIR does come with the tradeoffs of reduced sensitivity and increased vertical sidelobes (Kurdzo et al. 2017). The reduced sensitivity is mitigated by using pulse compression, but even so, the sensitivity is still less than other traditional mobile radars. Because of this, the AIR has been primarily used for close-range observations of tornadoes (e.g., Mahre et al. 2018; Griffin et al. 2019), as the scanning is rapid enough to adequately observe tornado development, maintenance, and dissipation. The author is unaware of any previous dual-Doppler studies that have used data from the AIR, so this study may be the first to use the AIR in this manner. See Isom et al. (2013) for more details on the design of the AIR.

In addition to the two rapid-scan radars used for collecting the dual-Doppler dataset, the Shared-Mobile Atmospheric Research and Teaching Radar 3 (SMART-R3; Biggerstaff et al. 2005) was used as a verification source for the dual-Doppler and EnKF retrievals. SMART-R3 is the newest in the series of mobile, C-band radars and was completed in 2018. As a C-band radar, SMART-R3 is less prone to attenuation than mobile X-band radars, but has a larger beamwidth. The SMART-R radars have been used to study a wide variety of atmospheric features such as drylines (Buban et al. 2007), supercells (Davenport and Parker 2015), and tropical cyclones (Knupp et al. 2006).

2.2 Data Collection

2.2.1 Meteorological Overview

Data collection for this study occurred on 4 September 2018 in central Oklahoma. On this day, upper-level flow over Oklahoma was mainly southerly as a broad upper-level ridge was located over the eastern half of the continental United States (CONUS), and a trough associated with the subtropical jet stream was positioned over the southwestern CONUS (Fig. 2.1). The southerly flow throughout the depth of the troposphere advected anomalously high moisture values over the region. Both the 1200 UTC 4 Sept 2018 and 0000 UTC 5 Sept 2018 soundings from Norman, OK had high precipitable water suggestive of an almost tropical environment (Fig. 2.2). In fact, the precipitable water value of 2.2 inches observed by the 1200 UTC sounding broke the daily record for precipitable water at the site. With these high moisture values, the environment was quite unstable. The soundings at the Norman, OK sounding site likely bracketed the time of peak instability since the two soundings occurred before sunrise and after the precipitation occurred, but the 1200 UTC sounding showed no CIN and a CAPE value of 1068 J kg^{-1}. This instability, combined with the minimal vertical wind shear and high precipitable water, led to widespread structurally complex convection over central Oklahoma.

At 1200 UTC on 4 Sept 2018, the Next Generation Weather Radar (NEXRAD) Weather Surveillance Radar-1998 Doppler (WSR-88D; Crum and Alberty 1993; Crum et al. 1998) network observed a north–south line of weak convection over central Oklahoma (Fig. 2.3a). Over the next 3 hours the original convection weakened and became remnant stratiform precipitation (Fig. 2.3b). The instability created by diurnal heating helped to initiate convection over western Oklahoma, and by 1800 UTC, convection was widespread in the western half of the state (Fig. 2.3c). The convection developed later in the central part of the state due to the early morning convection, but by 2100 UTC new convection was beginning to develop in central Oklahoma (Fig. 2.3d). A small storm initiated near Chickasha, OK and was moving northward. This storm was the focus for the dual-Doppler data collection. For the next hour, this storm grew in size as it moved through the dual-Doppler domain (Fig. 2.4). The storm began to dissipate around 2200 UTC, but by this time, the storm was located on the northern edge of the dual-Doppler lobe.

2.2.2 Radar Positioning and Scanning Strategies

The mobile radars positions during data collection are shown in Fig. 2.4. The AIR was positioned north of the target storm and RaXPol was located 15.48 km at 121.66° from the AIR. SMART-R3 was positioned in the dual-Doppler lobe 12.35 km and 14.76 km away from RaXPol and the AIR, respectively. RaXPol began data collection at 2055 UTC and continued scanning until 2159 UTC. Each volume scan consisted of 360° plan-position indicator (PPI) scans at 13 elevation angles from 1–19.5°, so vertical beam spacing was

1.5°. With this scanning strategy, RaXPol collected a full volume of data every 30 seconds. The AIR began data collection at 2120 UTC and ended data collection at 2209 UTC. The AIR was performing 165° sector scans, obtaining a $165^\circ \times 20^\circ$ volume of data oversampled in elevation to 0.5° spacing every 9 seconds. Finally, SMART-R3 began scanning at 2122 UTC and finished data collection at 2218 UTC. SMART-R3 was serving as the verification point for the vertical velocity retrievals. It obtained PPIs at 88° elevation every 18 seconds. While a 90° PPI would have been optimal for the study, radar pedestal constraints limited the maximum elevation angle to 88°. Additionally, the SMART-R3 periodically performed a low-altitude (2°) PPI to remove rainwater from the radar antenna. Gaps exist in the verification dataset when this shallow angle PPI was performed (Fig. 2.5).

2.3 Data Quality Control

2.3.1 Basic Quality Control

Post–data collection, quality control was done on all three radar datasets. The wind speeds associated with this storm were not high and neither the AIR nor the RaXPol had aliased radial velocities. However, since SMART-R3 was vertically pointing, the radial velocities were a combination of particle terminal fall velocity and air vertical velocity, so aliasing occurred in some of the stronger downdrafts. This aliasing was easy to correct for as large positive vertical velocities would not be possible in falling precipitation (at least in this storm), so regions of aliased velocities were identified by high reflectivity and strong positive radial velocities. When this pattern was found, the correction to dealias the velocities was applied to those radar bins.

The RaXPol data were quality controlled using the Solo3 software (Oye et al. 1995). This consisted of using Solo3's despeckling algorithm, and then the remaining radar artifacts were removed through manual editing. The full AIR dataset consisted of 14,220 sweeps, so it was not feasible to use the Solo3 software for manual editing. Therefore, the data were quality controlled using automated routines. In the initial processing of the AIR data a ground clutter filter was applied. This substantially reduced the ground clutter in the AIR dataset, but some still remained. Ground clutter maps were created from the first few volume scans when there was little precipitation in range for the AIR to observe. These clutter maps were then used to remove the remaining ground clutter throughout the entire dataset. The remaining speckles in the AIR dataset where removed with the following routine: An approximately 600-m square averaging region was centered on the radar bin being analyzed. Then five time levels centered on the time currently being quality controlled were considered. At each time level, it was determined if greater than 30% of the averaging region contained radar echoes. If fewer than three time levels had greater than 30% echo coverage, the radar bin being evaluated was considered a speckle and was removed. After despeckling some bad radial velocity bins were still present. To remove these, the same despeckling averaging window was used. The mean radial velocity in this averaging window was calculated and if the radial velocity at the point of interest differed from the area-averaged radial velocity by more than 5 m s^{-1} the bin was removed. This procedure was highly tailored to this particular dataset, and the thresholds used for this dataset would likely not be applicable for other datasets, especially in more vigorous convection.

Finally, a high bias in the SMART-R3 reflectivities needed to be corrected so the reflectivity could be used to estimate terminal fall velocity. The WSR-88Ds are subject to calibration standards, so the KTLX reflectivity can be used as the true reflectivity for correcting this bias. Data from KTLX was too coarse in elevation and time to be used directly, so the KTLX reflectivities were first compared to the RaXPol reflectivities. There was very little difference between the KTLX and RaXPol reflectivities at common data times around the SMART-R3 location, suggesting that the RaXPol reflectivities were relatively unbiased. The RaXPol reflectivities were then compared to the SMART-R3 reflectivities to estimate the SMART-R3 reflectivity bias. This bias was then removed from the dataset (Fig. 2.6).

2.3.2 RaXPol Azimuth Correction

While reviewing animations of the RaXPol data, it was discovered that there were sudden azimuthal displacements in the dataset (Fig. 2.7). The displacements cause the storm to appear to jitter when an animation of the dataset is played. These azimuthal displacements were sometimes large, often over 1°. Complicating matters, the azimuthal displacements are not constant within the same sweep. For example, radar echoes east of the radar may be shifted in a positive direction, while echoes west of the radar are shifted in a negative direction. If the change in the azimuthal displacements occurred at an azimuth where radar echoes were present, the radar echo appeared to expand or contract in that location. These azimuthal displacements also varied with each elevation in the volume.

The cause of these azimuthal displacements is unknown. The stabilizers on the radar truck were deployed during data collection, but the vigorous mechanical scanning of a heavy radar antenna still may have caused the truck to shake. Other operators of RaXPol have noticed similar azimuthal displacements in other RaXPol datasets (Weinhoff 2018; personal communication), so this may be a common issue in RaXPol datasets. Nevertheless, these displacements needed to be corrected before using the data in any analyses.

Correcting for azimuthal displacement errors of various forms is somewhat common with mobile radar datasets and can even be necessary with fixed position radars. Some azimuthal displacement errors can be corrected using ground clutter (Rico-Ramirez et al. 2009) or the radiation emitted by the sun (Arnott et al. 2003; Muth et al. 2012). However, these techniques correct errors that are constant or slowly changing and uniform throughout the radar volume. For this dataset, the ground clutter technique may be applicable for the low elevation scans, but since the azimuthal displacements vary with elevation, this technique would not work for higher elevation scans where there is less ground clutter. The uniqueness of the azimuthal displacements in the RaXPol dataset required a new correction technique to be developed.

Azimuthal displacements cause apparent deviations in storm motions. More specifically, the displacements cause perturbations in the azimuthal velocity of the storm in a polar coordinate system centered on the radar. Therefore, if the true azimuthal velocity is known (even coarsely) and the deviations from the true azimuthal velocity can be determined, the azimuthal displacements can potentially be corrected. This is the premise of the azimuthal displacement correction technique that was developed in this study for the RaXPol dataset.

For this study, the radar echo's azimuthal velocities are calculated from the Cartesian pattern translation velocities retrieved by the Shapiro et al. (2010) advection correction routine. A brief overview of the routine will be presented here, but for more detail on the procedure see Shapiro et al. (2010). This technique uses the frozen turbulence hypothesis (Taylor 1938) as a weak constraint to solve for the pattern translation components that minimize the following cost function:

$$J = \iiint \left[\alpha \left(\frac{\partial R}{\partial t} + U\frac{\partial R}{\partial x} + V\frac{\partial R}{\partial y} \right)^2 + \beta \left|\nabla_h U\right|^2 + \beta \left|\nabla_h V\right|^2 \right] dxdydt, \tag{2.1}$$

where α is a binary footprint function that indicates where data is available, R is reflectivity, and U and V are the pattern translation components in the x and y directions. The technique allows for spatially variable pattern translation components, so the cost function includes first order spatial smoothness constraints. The parameter β is a smoothing parameter that is specified by the user. A larger smoothing parameter will result in pattern translation components that are less spatially variable. Minimizing (2.1) leads to three Euler–Lagrange equations for the pattern translation components and the reflectivity:

$$\frac{\partial^2 U}{\partial x^2} + \frac{\partial^2 U}{\partial y^2} - \frac{1}{\beta T}\left[\int \alpha \frac{\partial R}{\partial t}\frac{\partial R}{\partial x} dt + U \int \alpha \left(\frac{\partial R}{\partial x} \right)^2 dt + V \int \alpha \frac{\partial R}{\partial x}\frac{\partial R}{\partial y} dt \right] = 0, \tag{2.2}$$

$$\frac{\partial^2 V}{\partial x^2} + \frac{\partial^2 V}{\partial y^2} - \frac{1}{\beta T}\left[\int \alpha \frac{\partial R}{\partial t}\frac{\partial R}{\partial y} dt + U \int \alpha \frac{\partial R}{\partial x}\frac{\partial R}{\partial y} dt + V \int \alpha \left(\frac{\partial R}{\partial y} \right)^2 dt \right] = 0, \tag{2.3}$$

$$\alpha\left(\frac{\partial}{\partial t}+U\frac{\partial}{\partial x}+V\frac{\partial}{\partial y}\right)^2 R+\alpha\left(\frac{\partial U}{\partial x}+\frac{\partial V}{\partial y}\right)\left(\frac{\partial R}{\partial t}+U\frac{\partial R}{\partial x}+V\frac{\partial R}{\partial y}\right) + \left(\frac{\partial \alpha}{\partial t}+U\frac{\partial \alpha}{\partial x}+V\frac{\partial \alpha}{\partial y}\right)\left(\frac{\partial R}{\partial t}+U\frac{\partial R}{\partial x}+V\frac{\partial R}{\partial y}\right)=0. \tag{2.4}$$

The advection correction retrieval requires the reflectivity field to be specified at two input times. From these input times, first-guess spatially constant pattern translation components are found using the Gal-Chen (1982) procedure. These first-guess pattern translation components are then used in (2.4) to advect the reflectivity to its position at intermediate time steps between the two input times. Using the advected reflectivity, (2.2) and (2.3) are solved using successive relaxation. The procedure is repeated using the new pattern translation velocities for the advection step. This loop continues until the change in pattern translation components between iterations falls below a specified tolerance. The advection-corrected reflectivity field and the pattern translation components are then output. However, for this application we are only interested in the pattern translation components.

The Shapiro et al. (2010) advection correction technique requires the input data to be on a Cartesian grid, so a Cressman filter (Cressman 1959) with a 400-m Cressman radius was used to put the data from every PPI scan on a 125-m grid. Then for each elevation angle, the pattern translation components between consecutive scans were found for the entire RaXPol data collection period using the Shapiro et al. (2010) procedure. The true pattern translation components are not known, however, the randomness of the azimuthal displacements suggests that the mean pattern translation components from a large number of sweeps should lead to a reasonably accurate estimate of the true pattern translation components. For this dataset, the pattern translation is remarkably uniform in both time and space, so the mean pattern translation components for the entire data collection period is used as the estimate of the true pattern translation components. For a more complex storm environment with variable storm motion, smaller averaging windows would need to be used.

Once the Cartesian pattern translation components are retrieved, they are converted to the radial and azimuthal pattern translation components for the polar coordinate system centered on the radar. The perturbation azimuthal velocity is calculated by subtracting the local azimuthal velocity computed from the mean pattern translation components from the local azimuthal velocity of each sweep. From these perturbation azimuthal velocities, the azimuthal displacements can be calculated by first calculating perturbation angular velocity and then multiplying the perturbation angular velocity by the time between volume scans. The last step before correcting the azimuthal displacements is to calculate a 15° azimuthal mean of the azimuthal displacements centered on each azimuth in the sweep. The 15° mean azimuthal displacements are used for the final correction to prevent large distortions in the spacing between azimuths.

The correction of the azimuthal displacements starts with the second sweep for each elevation scan and then proceeds sequentially. If the previous sweep's displacement for a particular azimuth was of the opposite sign, the previous sweep's correction is subtracted from the current sweep's correction to account for the calculated displacement actually representing the data shifting back to its correct position. This prevents over-correcting of the displacements. Then, for the next sweep, the sign of the previous displacement does not matter for the correction since the displacement should be a shift from the true location. The procedure continues in this manner until all sweeps are corrected.

This azimuthal correction technique is able to reduce the azimuthal displacements, but it does not completely eliminate the issue (Fig. 2.8). The success of the azimuthal displacement correction is largely dependent on the accuracy of the pattern translation component retrieval from the Shapiro et al. (2010) advection correction technique. Inaccurate advection correction results can occur due to solution non-uniqueness, or due to small gradients in the reflectivity in the direction of the pattern translation vectors. Additionally, since each elevation scan was corrected independently, the quality of the correction can vary in elevation scan in a volume. Overall, this technique is most successful at reducing the largest azimuthal displacements where the precision of the advection correction technique is less important. The described azimuthal displacement correction shows promise with this dataset, but it is unknown if the correction will be as successful for other, more complex datasets.

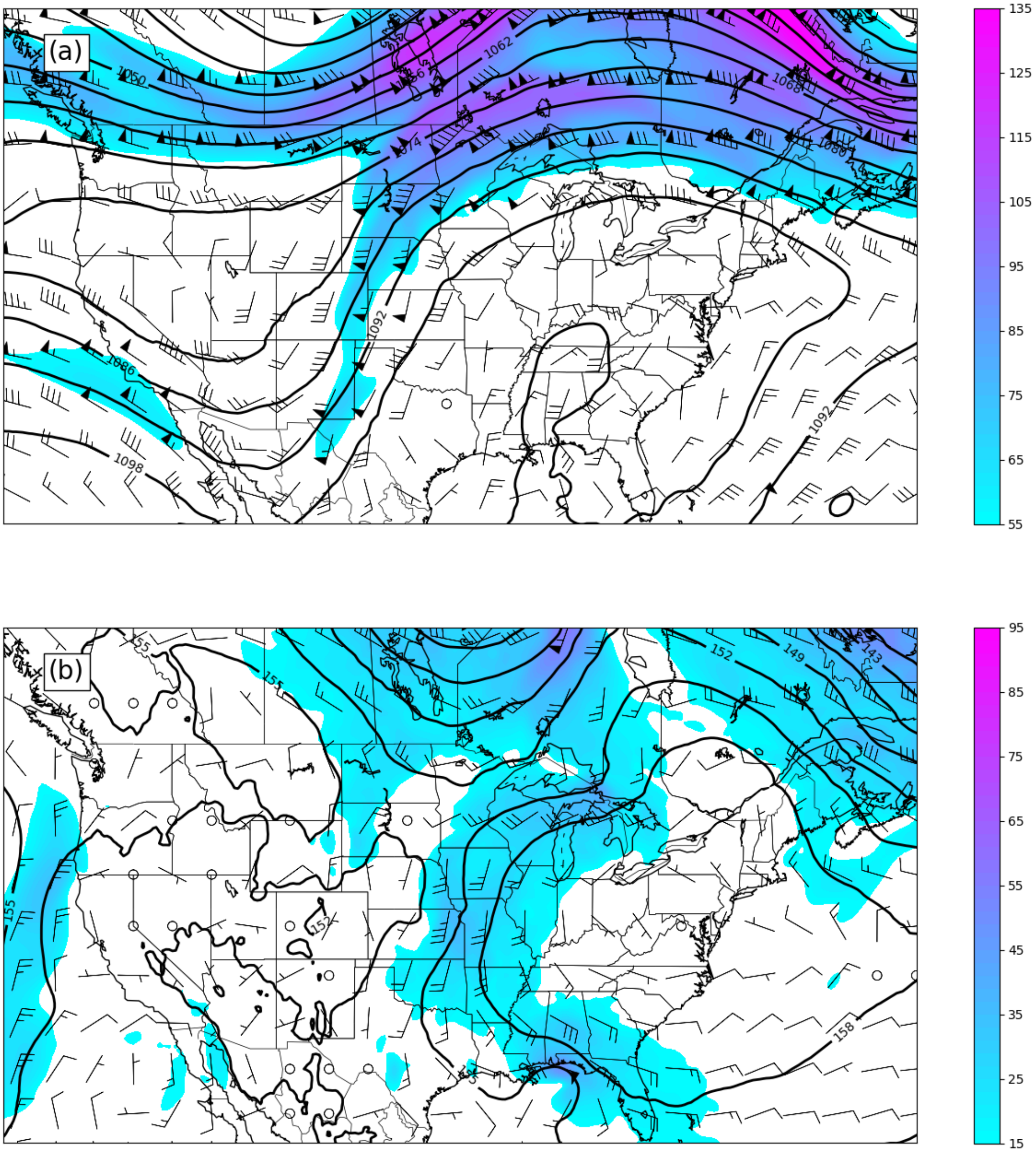

Figure 2.1: Geopotential height (dam) and winds (kts) at (a) 250 hPa and (b) 850 hPa from the ERA5 reanalysis Hersbach et al. (2020) valid for 1800 UTC on 4 Sept 2018. Wind speeds above (a) 50 kts and (b) 15 kts are shaded.

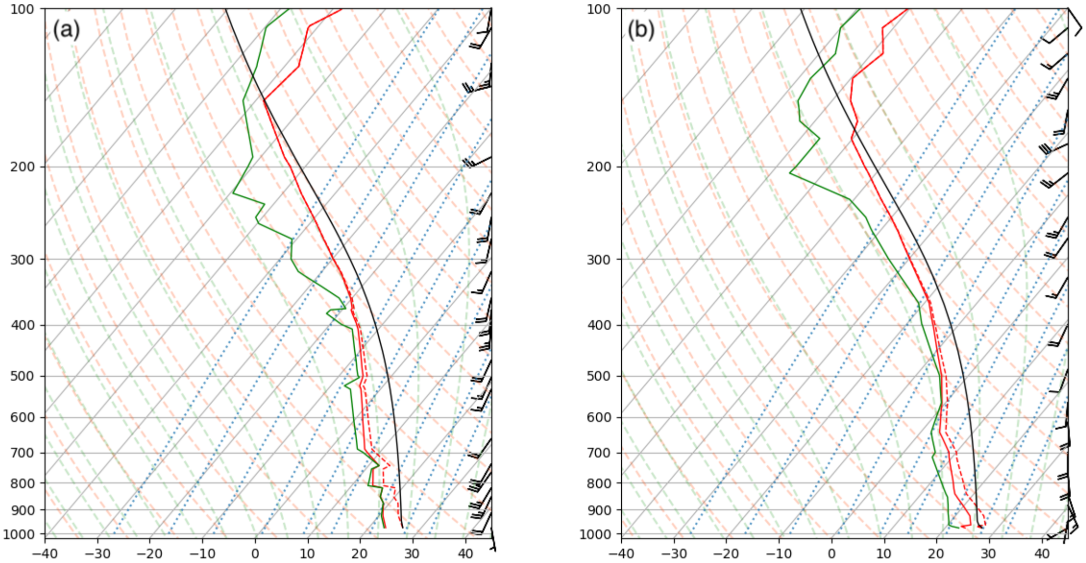

Figure 2.2: Radiosonde profiles at (a) 1200 UTC 4 Sept 2018 and (b) 0000 UTC 5 Sept 2018 from Norman, OK. The solid red line is temperature (°C) and the green line is dewpoint (°C). The dashed red line is virtual temperature (°C) and the black line is virtual temperature corrected surface parcel profile (°C). The plotted wind barbs are in knots.

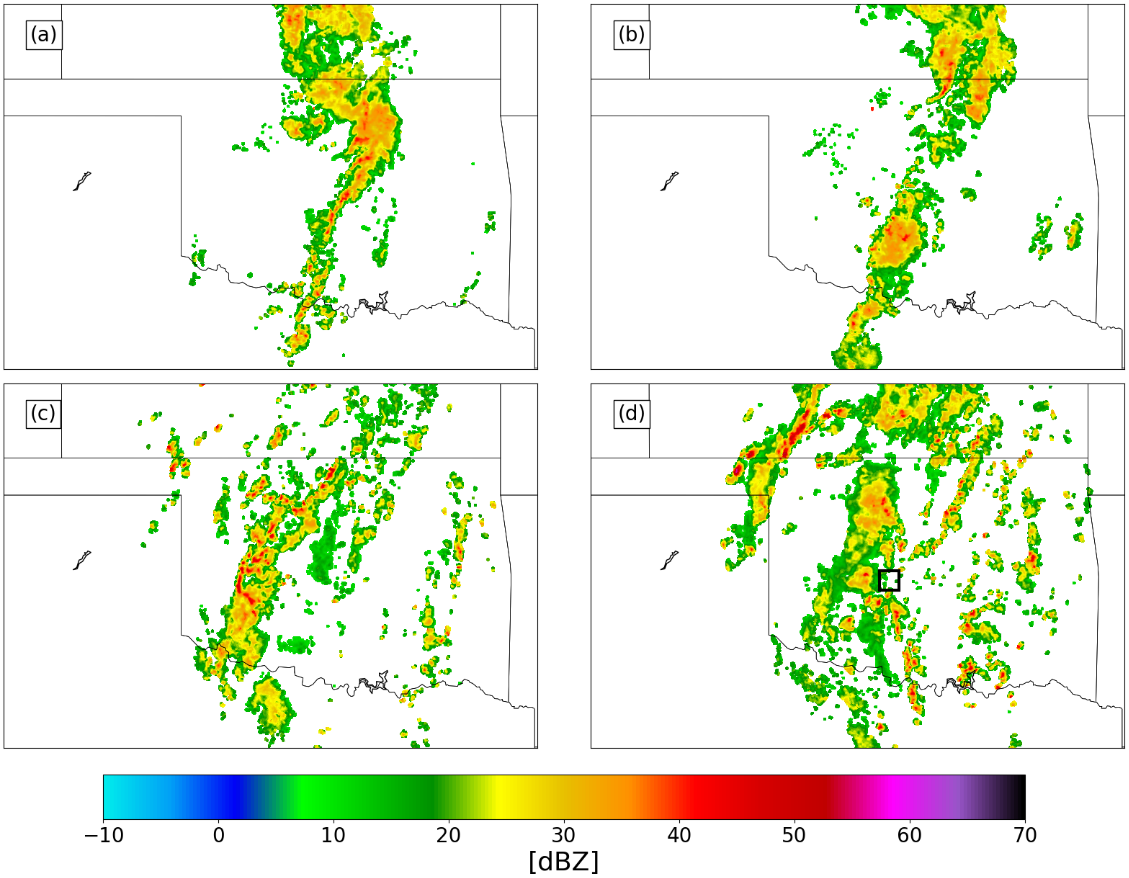

Figure 2.3: Mosaic radar reflectivity (dBZ) from the KTLX, KVNX, and KINX WSR-88D radars at (a) 1200, (b) 1500, (c) 1800, and (d) 2100 UTC. The black square in (d) represents the area observed by the mobile radars during dual-Doppler data collection, which is shown in Fig. 2.4

.

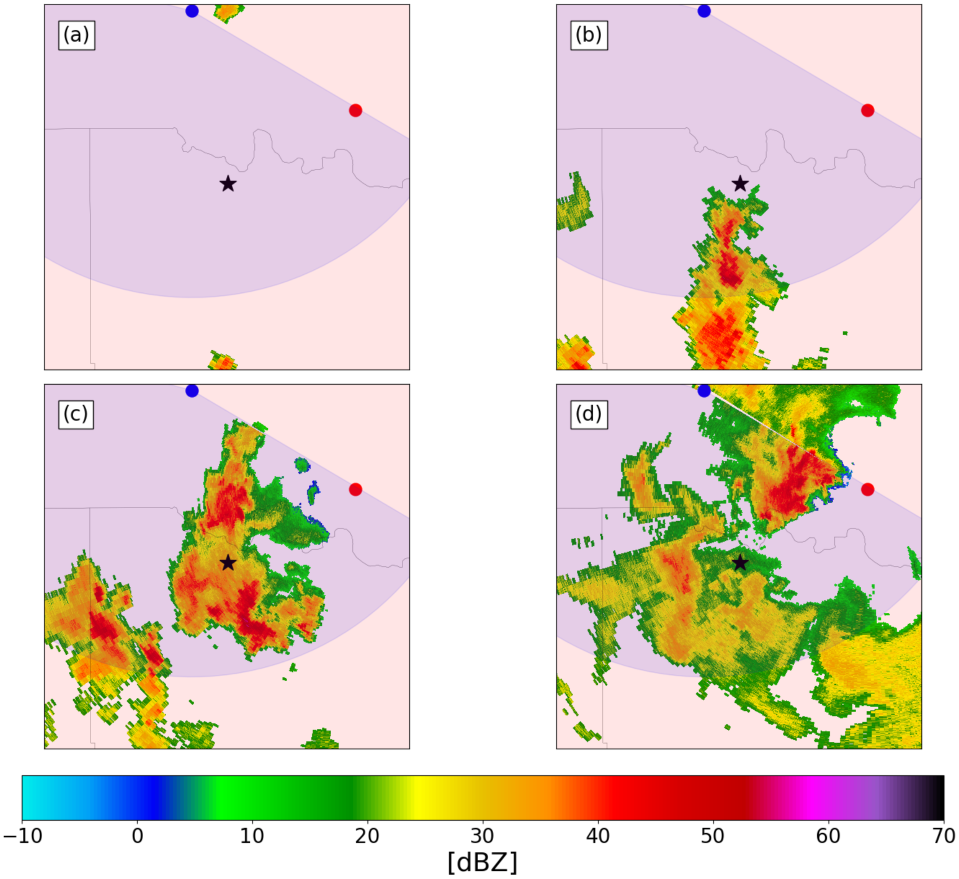

Figure 2.4: Radar reflectivity (dBZ) from RaXPol at (a) 2100, (b) 2120, (c) 2140, and (d) 2159 UTC. RaXPol and the AIR were located at the red and blue circles, respectively. The position of SMART-R3 is represented by the black star. The area scanned by only RaXPol is shaded red and the area scanned by the AIR and RaXPol is shaded violet.

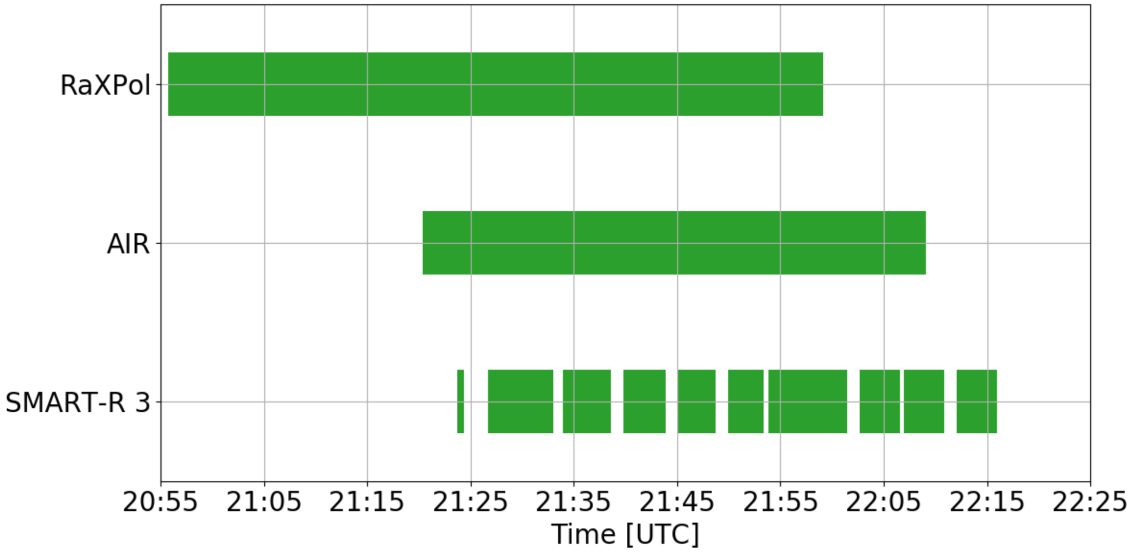

Figure 2.5: Times when data are available for RaXPol, the AIR, and SMART-R3 on the 4 Sept 2018 deployments.

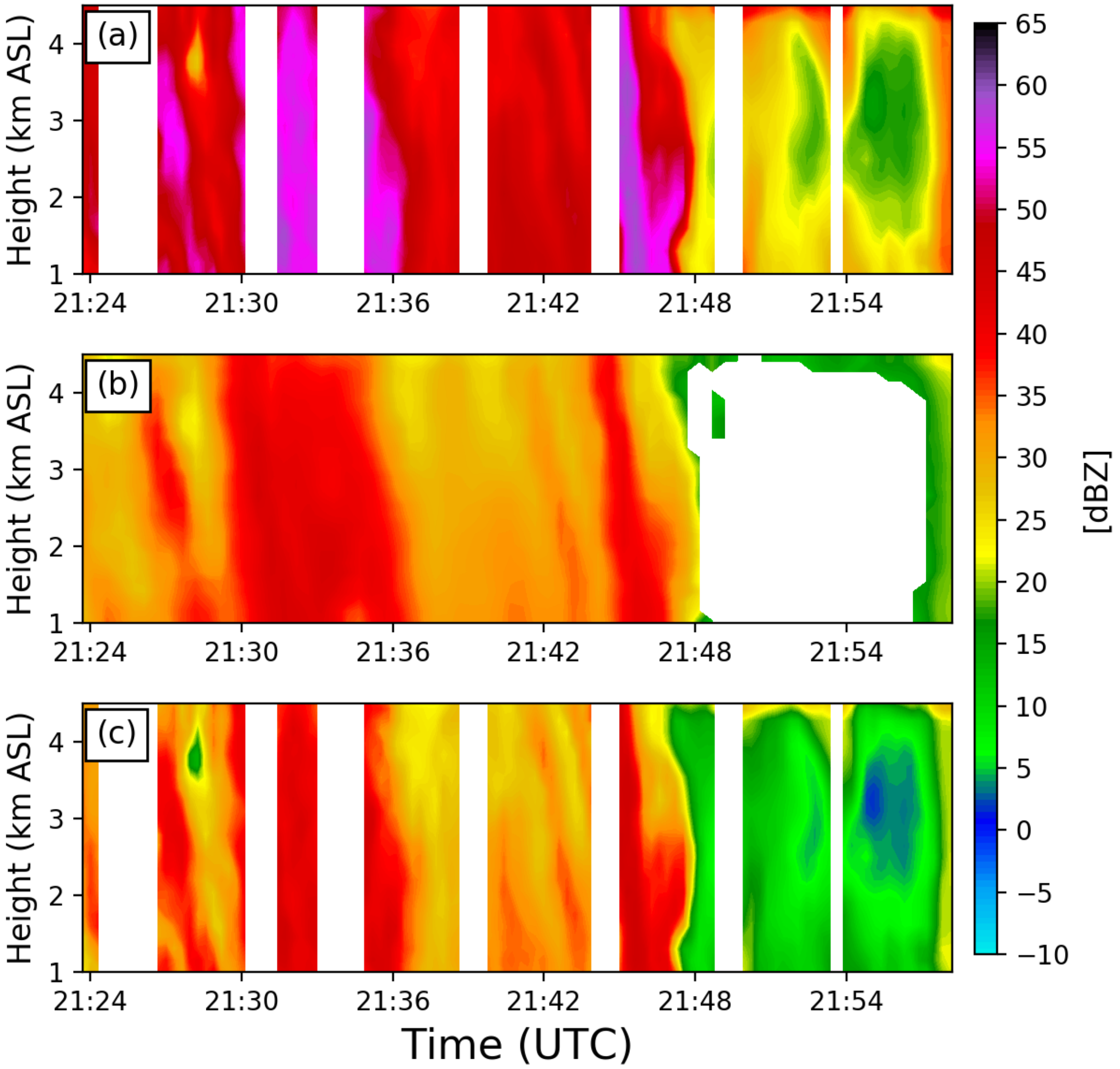

Figure 2.6: 88° elevation angle PPI-scan averaged reflectivity from the SMART-R3 (a) before bias correction and (c) after bias correction. (b) Gridded reflectivity from RaXPol at points above the SMART-R3, which was used for determining the SMART-R3 bias. Missing data in (a) and (c) is due to shallow angle PPIs that were performed to remove water from the SMART-R3 antenna.

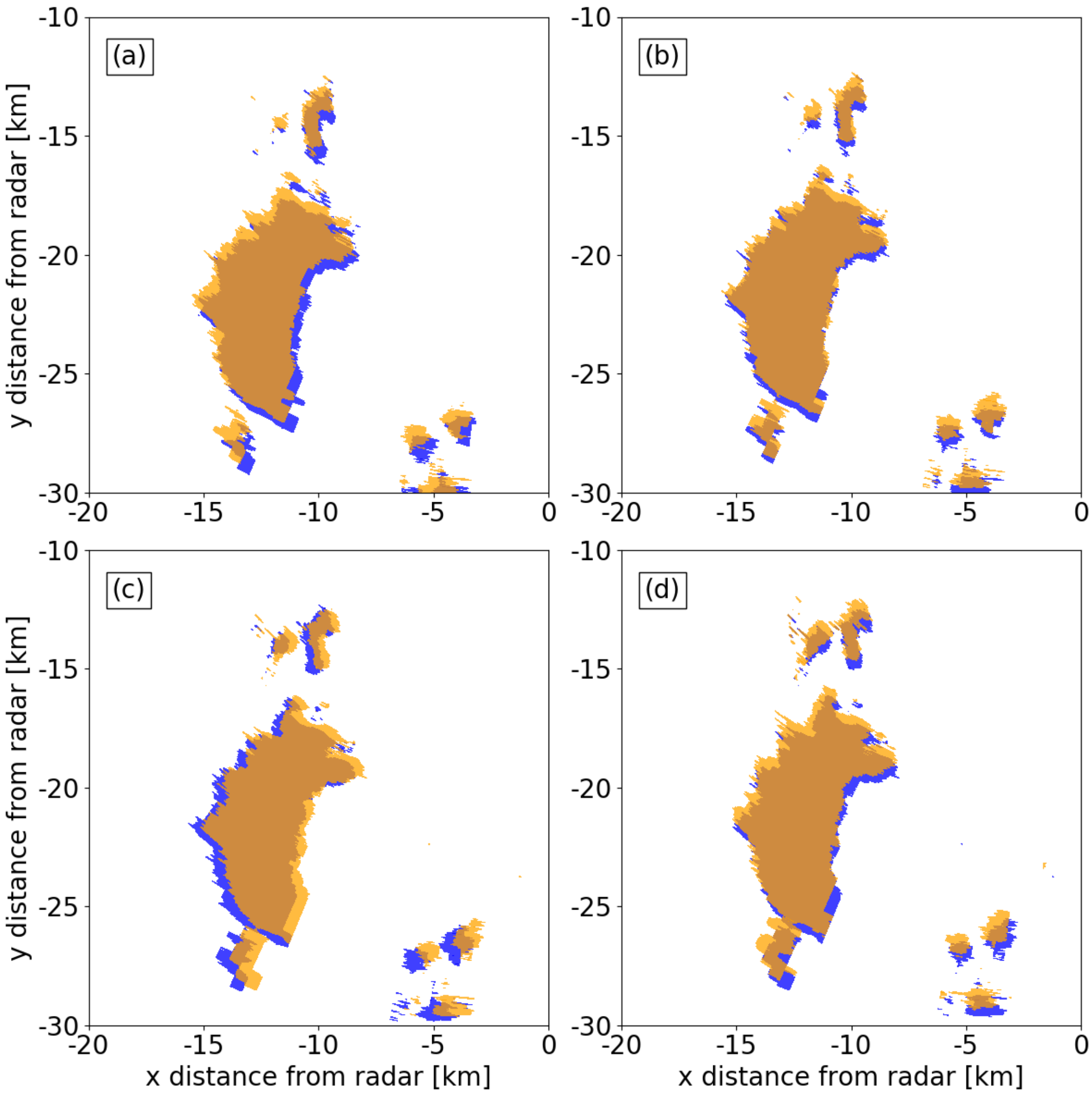

Figure 2.7: Jitter evident in the RaXPol data in consecutive scans. Areas with reflectivity greater than 25 dBZ at (a) 211211 (blue) and 211241 (orange), (b) 211241 (blue) and 211311 (orange), (c) 211311 (blue) and 211341 (orange), (d) 211341 (blue) and 211411 (orange) from the 1° RaXPol PPI scans.

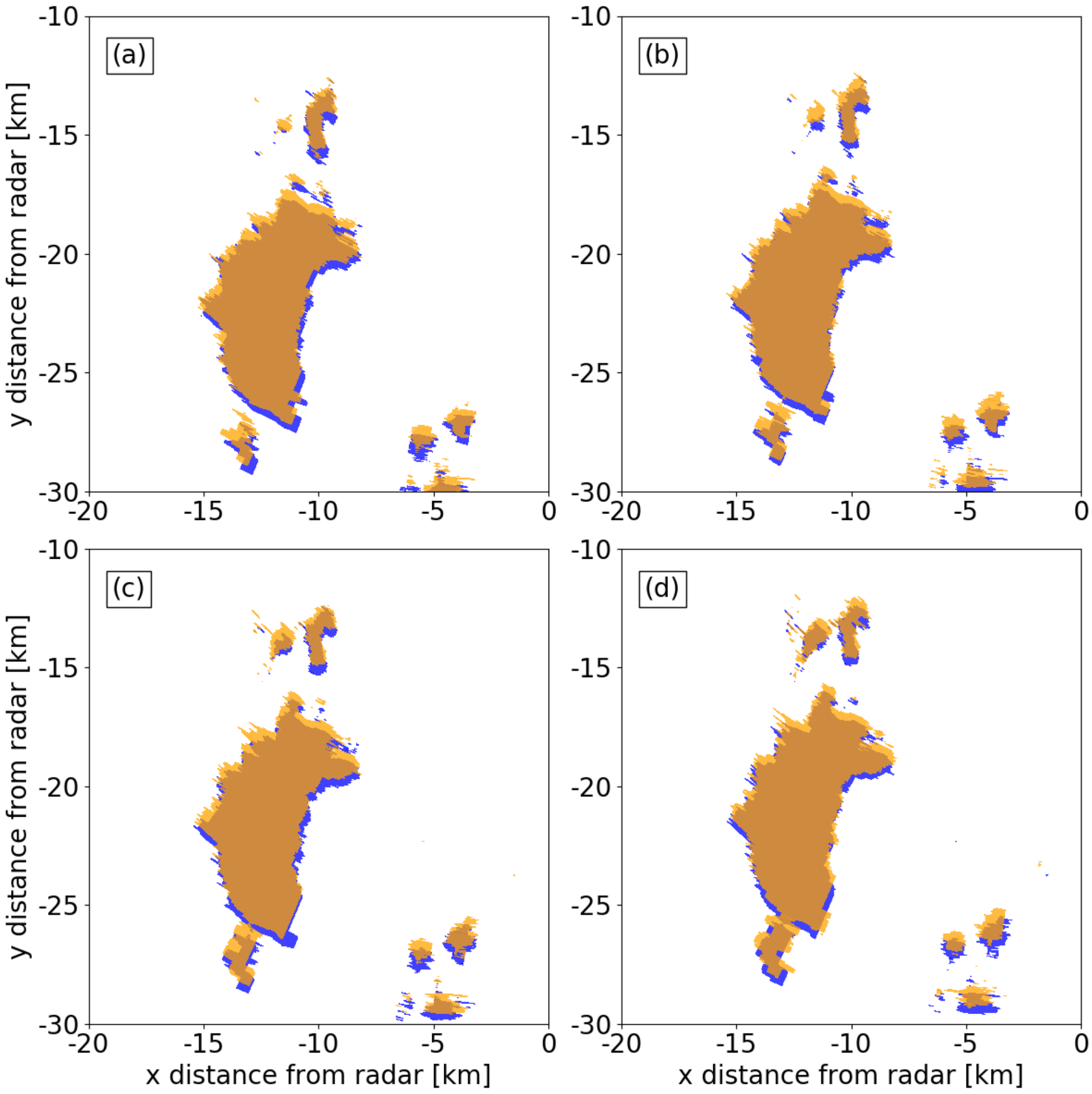

Figure 2.8: Areas with reflectivity greater than 25 dBZ for same scans as in Fig. 2.7, but after the azimuthal displacement correction.

Chapter 3

Three-Dimensional Spatially Variable Advection Correction

3.1 Background

Conventional scanning radars are unable to collect a full volume of data simultaneously. This poses a problem for radar analyses constructed for a single moment in time. The features being observed are both evolving and advecting during the data collection for a full volume, which can cause errors in the radar analyses especially when volume scan times are long. Radar advection correction is a tool that can be used to correct for the advection errors in radar analyses such as accumulated rainfall maps, single-Doppler analysis, and dual-Doppler analysis (Shapiro et al. 2010). Radar advection correction techniques are typically based on the two-dimensional frozen turbulence hypothesis (Taylor 1938),

$$\frac{\partial R}{\partial t} + U\frac{\partial R}{\partial x} + V\frac{\partial R}{\partial x} = 0, \tag{3.1}$$

where U and V are the pattern translation components (not the same as air velocity components u and v) in the x and y directions, respectively, and R is a scalar, which in this case is reflectivity. When this hypothesis is applied to radar data, it is often assumed that the radar field has no evolution and any change in the field at a fixed point is due to advection of the field. Therefore, if U and V are known, the advection in the field can be corrected so all observations are at their proper locations valid at a single analysis time.

A wide range of techniques that vary in complexity have been used to retrieve U and V for advection correction. The simplest but most error prone way to retrieve the pattern translation components is by visually tracking echoes. (e.g., Heymsfield 1978; Austin 1987; Dowell and Bluestein 1997; Wurman et al. 2007). More complex and automated advection correction procedures have used a cross-correlation analysis technique initially developed for single-Doppler wind retrievals (e.g., Rinehart and Garvey 1978; Tuttle and

Foote 1990; Li et al. 1995; Gerstner and Heinemann 2008; Wang et al. 2013a) or variational techniques such as the Shapiro et al. (2010) procedure described and used in Chapter 2. One feature of the variational approach is that the frozen turbulence hypothesis is applied as a weak constraint, so the constraint does not have to be exactly satisfied. This is beneficial when working with real radar data since it is unlikely that the change in the radar field with time is entirely due to advection. Applying the frozen turbulence hypothesis as a weak constraint can help prevent artifacts in the retrieved pattern translation components.

The Shapiro et al. (2010) advection correction procedure has proven to be useful for many radar analysis problems. The technique has been used in a traditional manner to correct for the advection in dual-Doppler datasets (Wienhoff et al. 2018), but it has also been used in nontraditional ways such as the azimuthal displacement correction described in Chapter 2, and for shortening the discretization timestep for vorticity tendency calculations in vertical vorticity constraint dual-Doppler analysis (Dahl et al. 2019). However, one limitation of the Shapiro et al. (2010) advection correction technique is that it can only correct for two components of advection on a two-dimensional surface. Convective storms can have significant vertical advection, and in these cases the two-dimensional advection correction may alias the vertical advection into horizontal advection. Additionally, since the advection correction technique can only be used on a two-dimensional surface, it can only be applied to a volume of data by performing the advection correction separately on each vertical level. This can cause vertical discontinuities in the retrieved pattern translation components, and in the advected corrected field itself.

The potential issues with the two-dimensional Shapiro et al. (2010) advection correction procedure can be shown by using the advection correction procedure on an analytical dataset where the scalar field is described by

$$F(x,y,z) = 20\sin\left[\frac{4\pi(x-U_cT)}{L_x}\right]\sin\left[\frac{4\pi(y-V_cT)}{L_y}\right]\sin\left[\frac{4\pi(z-W_cT)}{L_w}\right], \tag{3.2}$$

where T is time; U_c, V_c, and W_c are the x, y, and z temporally and spatially constant pattern translation components; and L_x, L_y, and L_z are the domain size in in the x, y, and z dimensions. For this dataset, $U_c = 10$ m s^{-1}, $V_c = 7.5$ m s^{-1}, $W_c = 5$ m s^{-1}, and the input times used for the advection correction are at $T = 0$ s and $T = 150$ s. The domain is 50.25×50.25×12.75 km with 250-m grid spacing in all dimensions (Fig. 3.1). Since this is a three-dimensional volume of data, the advection correction is performed separately on each vertical level. Obviously, the two-dimensional advection correction procedure is not able to retrieve W, but exceptionally large errors are present in the retrieved U and V (Fig. 3.2). The retrieved pattern translation components vary from -640.19 to 33.93 m s^{-1} for U and -40.60 to 485.14 m s^{-1} for V (Table 3.1). Figure 3.2 shows that some vertical levels have significant drop-offs in retrieval accuracy. At these vertical levels, the vertical translation causes apparent abrupt changes in the horizontal field at $T = 150$ s. Since the two-dimensional advection correction cannot account for vertical advection, the advection correction aliases the vertical translation into horizontal translation resulting in the bad pattern translation components and vertical discontinuities. These levels also have initially weak horizontal gradients, which makes the estimation of U and V difficult because there is less structure for the procedure to track.

The previous example is quite un-meteorological, but it highlights in an extreme manner the potential problems of the two-dimensional advection correction. A three-dimensional advection correction may be more applicable to volumes of data, and analyses that use advection correction may be improved when three-dimensional advection correction is used. This is also directly relevant to the vertical vorticity equation constrained dual-Doppler analysis as the two-dimensional advection correction has been used to improve DDA results for longer volume scans. Therefore, a three-dimensional advection correction may improve the overall DDA results even more than the two-dimensional advection correction. This chapter describes a three-dimensional spatially variable advection correction procedure and highlights the benefits and some limitations of the spatially variable advection correction approach.

3.2 Methodology

3.2.1 Mathematical Basis

The three-dimensional spatially variable advection correction is a variational approach, similar to the Shapiro et al. (2010) two-dimensional spatially variable advection correction. The goal of the procedure is to obtain the pattern translation components of a scalar field while also retrieving the scalar field valid at analysis times between two input times. The frozen turbulence hypothesis is the main constraint for the retrieval, but because this is a three-dimensional procedure this frozen turbulence constraint includes vertical advection. With this constraint, one wishes to find the U, V, and W that minimize the following cost function:

$$J = \iiiint \left[\alpha \left(\frac{\partial R}{\partial t} + U\frac{\partial R}{\partial x} + V\frac{\partial R}{\partial y} + W\frac{\partial R}{\partial z} \right)^2 + \beta\, |\nabla_h U|^2 + \gamma \left(\frac{\partial U}{\partial z} \right)^2 + \right. \\ \left. \beta\, |\nabla_h V|^2 + \gamma \left(\frac{\partial V}{\partial z} \right)^2 + \eta\, |\nabla_h W|^2 + \lambda \left(\frac{\partial W}{\partial z} \right)^2 \right] dxdydzdt. \tag{3.3}$$

The first term in the cost function is the three-dimensional frozen turbulence constraint applied to a scalar field R. As in the two-dimensional procedure, α is a binary analysis coverage function, which is 1 at locations where data are present and 0 in a data void. The remaining first derivative terms are spatial smoothness constraints. The parameters β, γ, η, and λ are positive constant parameters that control the horizontal smoothness of U and V, the vertical smoothness of U and V, the horizontal smoothness of W, and the vertical smoothness of W, respectively. The Shapiro et al. (2010) procedure only includes the β parameter. However, a three-dimensional retrieval requires separate smoothing parameters as the vertical variations and horizontal variations of pattern translation components may not necessarily be equal. For example, one might expect the vertical smoothness of U and V to be less than the horizontal smoothness due to vertical wind shear. Additionally, the variations in W are likely different than U and V. Ultimately, the three additional smoothing parameters gives the end user greater control over the spatial variability of the retrieval.

As in Shapiro et al. (2010), calculus of variations is used to minimize the cost function to obtain Euler–Lagrange equations for U, V, W, and R. Setting the variation of (3.3) equal to 0 yields

$$\begin{aligned}\iiiint \Bigg[\alpha\left(\frac{\partial R}{\partial t}+U\frac{\partial R}{\partial x}+V\frac{\partial R}{\partial y}+W\frac{\partial R}{\partial z}\right)\left(\frac{\partial \delta R}{\partial t}+U\frac{\partial \delta R}{\partial x}+V\frac{\partial \delta R}{\partial y}+W\frac{\partial \delta R}{\partial z}+\right.\\ \left.\delta U\frac{\partial R}{\partial x}+\delta V\frac{\partial R}{\partial y}+\delta W\frac{\partial R}{\partial z}\right)+\beta\left(\frac{\partial U}{\partial x}\frac{\partial \delta U}{\partial x}+\frac{\partial U}{\partial y}\frac{\partial \delta U}{\partial y}+\frac{\partial V}{\partial x}\frac{\partial \delta V}{\partial x}+\right.\\ \left.\frac{\partial V}{\partial y}\frac{\partial \delta V}{\partial y}\right)+\eta\left(\frac{\partial W}{\partial x}\frac{\partial \delta W}{\partial x}+\frac{\partial W}{\partial y}\frac{\partial \delta W}{\partial y}\right)+\gamma\left(\frac{\partial U}{\partial z}\frac{\partial \delta U}{\partial z}+\frac{\partial V}{\partial z}\frac{\partial \delta V}{\partial z}\right)+\\ \lambda\left(\frac{\partial W}{\partial z}\frac{\partial \delta W}{\partial z}\right)\Bigg]\,dxdydzdt=0.\end{aligned} \tag{3.4}$$

Equation (3.4) is then integrated by parts to obtain

$$I_{tb}+I_{xb}+I_{yb}+I_{zb}+I_{\delta U}+I_{\delta V}+I_{\delta W}+I_{\delta R}=0, \tag{3.5}$$

where

$$I_{tb}=\iiint\left[\alpha\left(\frac{\partial R}{\partial t}+U\frac{\partial R}{\partial x}+V\frac{\partial R}{\partial y}+W\frac{\partial R}{\partial z}\right)\delta R\right]_{t_1}^{t_1+T}dxdydz, \tag{3.6}$$

$$\begin{aligned}I_{xb}=\iiint\Bigg[\alpha U\left(\frac{\partial R}{\partial t}+U\frac{\partial R}{\partial x}+V\frac{\partial R}{\partial y}+W\frac{\partial R}{\partial z}\right)\delta R+\beta\left(\frac{\partial U}{\partial x}\delta U+\frac{\partial V}{\partial x}\delta V\right)+\\ \eta\left(\frac{\partial W}{\partial x}\delta W\right)\Bigg]_{x_1}^{x_2}dydzdt,\end{aligned} \tag{3.7}$$

$$\begin{aligned}I_{yb}=\iiint\Bigg[\alpha V\left(\frac{\partial R}{\partial t}+U\frac{\partial R}{\partial x}+V\frac{\partial R}{\partial y}+W\frac{\partial R}{\partial z}\right)\delta R+\beta\left(\frac{\partial U}{\partial y}\delta U+\frac{\partial V}{\partial y}\delta V\right)+\\ \eta\left(\frac{\partial W}{\partial y}\delta W\right)\Bigg]_{y_1}^{y_2}dxdzdt,\end{aligned} \tag{3.8}$$

$$\begin{aligned}I_{zb}=\iiint\Bigg[\alpha W\left(\frac{\partial R}{\partial t}+U\frac{\partial R}{\partial x}+V\frac{\partial R}{\partial y}+W\frac{\partial R}{\partial z}\right)\delta R+\gamma\left(\frac{\partial U}{\partial z}\delta U+\frac{\partial V}{\partial z}\delta V\right)+\\ \lambda\left(\frac{\partial W}{\partial z}\delta W\right)\Bigg]_{z_1}^{z_2}dxdydt,\end{aligned} \tag{3.9}$$

$$\begin{aligned}I_{\delta U}=\iiiint\Bigg[\alpha\frac{\partial R}{\partial x}\left(\frac{\partial R}{\partial t}+U\frac{\partial R}{\partial x}+V\frac{\partial R}{\partial y}+W\frac{\partial R}{\partial z}\right)-\beta\left(\frac{\partial^2 U}{\partial x^2}+\frac{\partial^2 U}{\partial y^2}\right)-\\ \gamma\left(\frac{\partial^2 U}{\partial z^2}\right)\Bigg]\delta U\,dxdydzdt,\end{aligned} \tag{3.10}$$

$$I_{\delta V} = \iiiint \left[\alpha \frac{\partial R}{\partial y} \left(\frac{\partial R}{\partial t} + U \frac{\partial R}{\partial x} + V \frac{\partial R}{\partial y} + W \frac{\partial R}{\partial z} \right) - \beta \left(\frac{\partial^2 V}{\partial x^2} + \frac{\partial^2 V}{\partial y^2} \right) - \gamma \left(\frac{\partial^2 V}{\partial z^2} \right) \right] \delta V dxdydzdt, \tag{3.11}$$

$$I_{\delta W} = \iiiint \left[\alpha \frac{\partial R}{\partial z} \left(\frac{\partial R}{\partial t} + U \frac{\partial R}{\partial x} + V \frac{\partial R}{\partial y} + W \frac{\partial R}{\partial z} \right) - \eta \left(\frac{\partial^2 W}{\partial x^2} + \frac{\partial^2 W}{\partial y^2} \right) - \lambda \left(\frac{\partial^2 W}{\partial z^2} \right) \right] \delta W dxdydzdt, \tag{3.12}$$

and

$$I_{\delta R} = -\iiiint \left[\alpha \left(\frac{\partial}{\partial t} + U \frac{\partial}{\partial x} + V \frac{\partial}{\partial y} + W \frac{\partial}{\partial z} \right)^2 R + \alpha \left(\frac{\partial U}{\partial x} + \frac{\partial V}{\partial y} + \frac{\partial W}{\partial z} \right) \left(\frac{\partial R}{\partial t} + U \frac{\partial R}{\partial x} + V \frac{\partial R}{\partial y} + W \frac{\partial R}{\partial z} \right) + \left(\frac{\partial \alpha}{\partial t} + U \frac{\partial \alpha}{\partial x} + V \frac{\partial \alpha}{\partial y} + W \frac{\partial \alpha}{\partial z} \right) \left(\frac{\partial R}{\partial t} + U \frac{\partial R}{\partial x} + V \frac{\partial R}{\partial y} + W \frac{\partial R}{\partial z} \right) \right] \delta R dxdydzdt. \tag{3.13}$$

Equations (3.6)–(3.9) are boundary integrals, while Eqs. (3.10)–(3.13) are integrals spanning the spatiotemporal analysis domain. Since this is a minimization problem, all of the above integrals must vanish (the δU, δV, δW, and δR are all arbitrary and independent of each other). The conditions that cause the boundary integrals to vanish are the same as in Shapiro et al. (2010) extended to three dimensions. The time boundary integral, (3.6), will vanish if:

1. $\alpha = 0$ — this occurs when no data is available to estimate R,
2. $\alpha = 1$, $\delta R = 0$ — this occurs when data is available at both analysis times so R is known
3. $\alpha = 1$, $\frac{\partial R}{\partial t} + U \frac{\partial R}{\partial x} + V \frac{\partial R}{\partial y} + W \frac{\partial R}{\partial z} = 0$ — this occurs when there is insufficient data for a direct estimate of R. This natural boundary condition enables data to be advected from another location based on the other input time to estimate R.

For the spatial boundary integrals to vanish, one of the two conditions must be met:

1. $\alpha = 0$,
2. $\alpha = 1$, $\frac{\partial R}{\partial t} + U\frac{\partial R}{\partial x} + V\frac{\partial R}{\partial y} + W\frac{\partial R}{\partial z} = 0$. This is similar to the natural boundary condition described above.

In addition to one of these two conditions, the gradients of the pattern translation components must be equal to zero on all boundaries. It should be noted that applying a zero gradient boundary condition on the lower boundary will allow for non-zero W at the lower boundary, and therefore, this condition would not be appropriate when the lower boundary is the ground. This should not typically be a problem as the lowest data level for radar data is often a couple hundred meters above the ground. Before considering the vanishing of the remaining integrals, (3.10), (3.11), and (3.12) can be rewritten as

$$\begin{aligned}\iiint \Bigg[\int \alpha \frac{\partial R}{\partial t}\frac{\partial R}{\partial x} dt + U \int \alpha \left(\frac{\partial R}{\partial x}\right)^2 dt + V \int \alpha \frac{\partial R}{\partial x}\frac{\partial R}{\partial y} dt + W \int \alpha \frac{\partial R}{\partial x}\frac{\partial R}{\partial z} dt - \\ \beta T\left(\frac{\partial^2 U}{\partial x^2} + \frac{\partial^2 U}{\partial y^2}\right) - \gamma T \frac{\partial^2 U}{\partial z^2}\Bigg] \delta U dxdydz,\end{aligned} \tag{3.14}$$

$$\begin{aligned}\iiint \Bigg[\int \alpha \frac{\partial R}{\partial t}\frac{\partial R}{\partial y} dt + U \int \alpha \frac{\partial R}{\partial x}\frac{\partial R}{\partial y} dt + V \int \alpha \left(\frac{\partial R}{\partial y}\right)^2 dt + W \int \alpha \frac{\partial R}{\partial y}\frac{\partial R}{\partial z} dt - \\ \beta T\left(\frac{\partial^2 V}{\partial x^2} + \frac{\partial^2 V}{\partial y^2}\right) - \gamma T \frac{\partial^2 V}{\partial z^2}\Bigg] \delta V dxdydz,\end{aligned} \tag{3.15}$$

and

$$\begin{aligned}\iiint \Bigg[\int \alpha \frac{\partial R}{\partial t}\frac{\partial R}{\partial z} dt + U \int \alpha \frac{\partial R}{\partial x}\frac{\partial R}{\partial z} dt + V \int \alpha \frac{\partial R}{\partial y}\frac{\partial R}{\partial z} dt + W \int \alpha \left(\frac{\partial R}{\partial z}\right)^2 dt - \\ \eta T\left(\frac{\partial^2 W}{\partial x^2} + \frac{\partial^2 W}{\partial y^2}\right) - \lambda T \frac{\partial^2 W}{\partial z^2}\Bigg] \delta W dxdydz,\end{aligned} \tag{3.16}$$

since U, V, and W are independent of time. The variations, δU, δV, δW, and δR are arbitrary and independent of each other, so the sum of the bracketed terms in (3.13), (3.14), (3.15), and (3.16) should be zero. This provides four equations, which can be used to solve for U, V, W, and R. These equations are

$$\begin{aligned}\beta\left(\frac{\partial^2 U}{\partial x^2}+\frac{\partial^2 U}{\partial y^2}\right)+\gamma\frac{\partial^2 U}{\partial z^2}-\frac{1}{T}\left[\int\alpha\frac{\partial R}{\partial t}\frac{\partial R}{\partial x}dt+U\int\alpha\left(\frac{\partial R}{\partial x}\right)^2dt+\right.\\ \left.V\int\alpha\frac{\partial R}{\partial x}\frac{\partial R}{\partial y}dt+W\int\alpha\frac{\partial R}{\partial x}\frac{\partial R}{\partial z}dt\right]=0,\end{aligned} \tag{3.17}$$

$$\begin{aligned}\beta\left(\frac{\partial^2 V}{\partial x^2}+\frac{\partial^2 V}{\partial y^2}\right)+\gamma\frac{\partial^2 V}{\partial z^2}-\frac{1}{T}\left[\int\alpha\frac{\partial R}{\partial t}\frac{\partial R}{\partial y}dt+U\int\alpha\frac{\partial R}{\partial x}\frac{\partial R}{\partial y}dt+\right.\\ \left.V\int\alpha\left(\frac{\partial R}{\partial y}\right)^2dt+W\int\alpha\frac{\partial R}{\partial y}\frac{\partial R}{\partial z}dt\right]=0,\end{aligned} \tag{3.18}$$

$$\begin{aligned}\eta\left(\frac{\partial^2 W}{\partial x^2}+\frac{\partial^2 W}{\partial y^2}\right)+\lambda\frac{\partial^2 W}{\partial z^2}-\frac{1}{T}\left[\int\alpha\frac{\partial R}{\partial t}\frac{\partial R}{\partial z}dt+U\int\alpha\frac{\partial R}{\partial x}\frac{\partial R}{\partial z}dt+\right.\\ \left.V\int\alpha\frac{\partial R}{\partial y}\frac{\partial R}{\partial z}dt+W\int\alpha\left(\frac{\partial R}{\partial z}\right)^2dt\right]=0,\end{aligned} \tag{3.19}$$

and

$$\begin{aligned}\alpha\left(\frac{\partial}{\partial t}+U\frac{\partial}{\partial x}+V\frac{\partial}{\partial y}+W\frac{\partial}{\partial z}\right)^2R+\alpha\left(\frac{\partial U}{\partial x}+\frac{\partial V}{\partial y}+\frac{\partial W}{\partial z}\right)\left(\frac{\partial R}{\partial t}+U\frac{\partial R}{\partial x}+\right.\\ \left.V\frac{\partial R}{\partial y}+W\frac{\partial R}{\partial z}\right)+\left(\frac{\partial\alpha}{\partial t}+U\frac{\partial\alpha}{\partial x}+V\frac{\partial\alpha}{\partial y}+W\frac{\partial\alpha}{\partial z}\right)\left(\frac{\partial R}{\partial t}+U\frac{\partial R}{\partial x}+\right.\\ \left.V\frac{\partial R}{\partial y}+W\frac{\partial R}{\partial z}\right)=0.\end{aligned} \tag{3.20}$$

For (3.20), it is specified that

$$\frac{\partial\alpha}{\partial t}+U\frac{\partial\alpha}{\partial x}+V\frac{\partial\alpha}{\partial y}+W\frac{\partial\alpha}{\partial z}=0 \tag{3.21}$$

so that α does not change along a trajectory. Applying (3.21) and expanding the total derivative as

$$\frac{D}{Dt}=\frac{\partial}{\partial t}+U\frac{\partial}{\partial x}+V\frac{\partial}{\partial y}+W\frac{\partial}{\partial z}, \tag{3.22}$$

(3.20) becomes,

$$\alpha\frac{D^2R}{Dt^2}+\alpha\left(\frac{\partial U}{\partial x}+\frac{\partial V}{\partial y}+\frac{\partial W}{\partial z}\right)\frac{DR}{Dt}=0. \tag{3.23}$$

Shapiro et al. (2010) showed that when $\alpha = 1$ the solution to an analogous equation is

$$R(t) = R(t_i) + [R(t_i + T) - R(t_i)] \frac{I(t)}{I(t_i + T)}, \tag{3.24}$$

where,

$$I(t) = \int_{t_i}^{t} \exp\left[- \int_{t_i}^{t'} div(t'')dt'' \right] dt'. \tag{3.25}$$

The only difference here from the solution in Shapiro et al. (2010) is that three-dimensional divergence,

$$div = \frac{\partial U}{\partial x} + \frac{\partial V}{\partial y} + \frac{\partial W}{\partial z}, \tag{3.26}$$

is used instead of two-dimensional divergence. It is important to note that (3.23) indicates that the retrieved scalar field will actually have some evolution correction since minimization of the weak constraint form of frozen-turbulence yields a partial differential equation for R that includes a second derivative with respect to time. Therefore, this technique may produce more accurate retrieved scalar fields than a pure advection correction procedure because the retrieved scalar field in this case is found with a linear interpolation of the scalar field from the two input times. Together, (3.17), (3.18), (3.19), and (3.23) provide the basis for the advection correction routine.

3.2.2 Procedure Structure

The advection correction retrieval inputs scalar fields on a three-dimensional Cartesian grid at times t_i and $t_i + T$. The retrieval begins with a first guess estimate of the U, V, and W fields. This first guess can be specified by the user, or a spatially constant pattern translation estimate can be calculated using a three-dimensional version of the Gal-Chen (1982) technique where

$$U = \frac{C(GH - LE) + D(GE - FH) + A\left(FL - G^2\right)}{F(D^2 - BL) + C(CL - DG) + G(BG - CD)}, \tag{3.27}$$

$$V = \frac{C(DH - LA) + G(DA - BH) + E\left(BL - D^2\right)}{F(D^2 - BL) + C(CL - DG) + G(BG - CD)}, \tag{3.28}$$

$$W = \frac{G\left(AC-BE\right)+D\left(CE-FA\right)+H\left(BF-C^{2}\right)}{F\left(D^{2}-BL\right)+C\left(CL-DG\right)+G\left(BG-CD\right)}, \tag{3.29}$$

and

$$A=\int\frac{\partial R}{\partial t}\frac{\partial R}{\partial x}dV_{3D}, \qquad B=\int\left(\frac{\partial R}{\partial x}\right)^{2}dV_{3D}, \qquad C=\int\frac{\partial R}{\partial x}\frac{\partial R}{\partial y}dV_{3D}, \tag{3.30}$$

$$D=\int\frac{\partial R}{\partial x}\frac{\partial R}{\partial z}dV_{3D}, \qquad E=\int\frac{\partial R}{\partial t}\frac{\partial R}{\partial y}dV_{3D}, \qquad F=\int\left(\frac{\partial R}{\partial y}\right)^{2}dV_{3D}, \tag{3.31}$$

$$G=\int\frac{\partial R}{\partial y}\frac{\partial R}{\partial z}dV_{3D}, \qquad H=\int\frac{\partial R}{\partial t}\frac{\partial R}{\partial z}dV_{3D}, \qquad L=\int\left(\frac{\partial R}{\partial z}\right)^{2}dV_{3D}, \tag{3.32}$$

where dV_{3D} signifies integration over the entire volume. Despite the arbitrary nature of the first guess, a reasonably accurate first guess is preferred to prevent the retrieval from converging to a wrong solution due to the non-uniqueness problem discussed by Shapiro et al. (2010). A more accurate first guess can also reduce the number of iterations needed for the procedure to converge, thereby reducing run time.

After the first guess is obtained, the initial U, V, and W are used to calculate forward and backward trajectories launched from every analysis point at every analysis time (such times are separated by small analysis timesteps) using a 4th-order Runge–Kutta scheme. During the trajectory calculations, the three-dimensional divergence at every analysis time is retained, so (3.25) can be evaluated. Once the trajectories reach $t_i + T$ for the forward trajectories or t_i for the backward trajectories, the scalar field value at the end point of the trajectory is obtained. It is unlikely that a trajectory will fall exactly on a grid point, so tri-linear interpolation is used when obtaining values from the grid during the trajectory calculations.

Once the trajectories are completed, (3.24) is used to obtain the analysis scalar field at each analysis time. Next, the forcing terms for (3.17)-(3.19) are calculated and the U, V, and W are found by solving (3.17)-(3.19) using successive over-relaxation. The change in the U, V, and W from the previous iteration (for the first iteration this is the first guess) are compared to a user specified tolerance. If the change in the pattern translation components falls below the tolerance, the procedure is deemed to have converged and the pattern translation components and scalar field at all analysis times are output. If the change is greater than the tolerance, the procedure is repeated with the new U, V, and W used for the trajectory calculations.

It was discovered that occasionally the advection correction retrieval for both two and three-dimensions would not converge and instead the pattern translation components would oscillate between two solutions. To counteract this, an option for “under relaxing” the retrieved pattern translation components was included. This is done by reducing the change in the pattern translation components by linearly weighting the previous and new pattern translation components like so:

$$U = (1-\mu)U_{prev} + \mu U_{new}, \tag{3.33}$$

$$V = (1-\mu)V_{prev} + \mu V_{new}, \tag{3.34}$$

$$W = (1-\mu)W_{prev} + \mu W_{new}, \tag{3.35}$$

where $0 < \mu \leq 1$ is chosen by the user. The specific value of μ needed to help the solution converge is case dependent, but choosing a lower value of μ is a safer choice as too low of a value should only cause the retrieval to perform more iterations than necessary at the optimal value, while too high of a value might not stop the oscillation of the solution, preventing convergence.

3.3 Procedure Tests

The three-dimensional advection correction procedure was tested using the same analytical dataset described in Section 1 that was used to show the deficiencies in the two-dimensional advection correction procedure. Cross-sections of the retrieved U, V, and W fields are shown in Fig. 3.3. The pattern translation fields look unremarkable, but this is the desired result for this constant pattern translation test. The largest error from the actual pattern translation components throughout the entire domain was 0.066 m s^{-1} (Table 3.1), which is a substantial improvement over the two-dimensional advection correction results.

While the analytical dataset test highlights the improvements of the three-dimensional procedure, the test does simulate a rather extreme scenario that is unlikely to occur in a real dataset. Therefore, the advection correction procedures were further tested using the reflectivity data collected by the AIR on 4 Sept 2018. The AIR data were chosen over the RaXPol data due to the uncertainty in the RaXPol dataset associated with the azimuthal displacement errors that were discussed in Chapter 2. The scans at 2138:37 and 2140:42 UTC were selected as the input scans for this test. These scans were chosen because data coverage at these times was high and the majority of the storm of interest was within the domain. A Cressman filter with a 400-m Cressman radius was used to put the data onto a $241 \times 241 \times 57$ grid with 125-m grid spacing in all dimensions. As in the analytical test, the two-dimensional advection correction procedure is run separately on each vertical level in the gridded volume while the three-dimensional procedure only has to be run once. A 6.25-second timestep was used for the trajectory calculation for both procedures. The smoothing parameter, β, for the two-dimensional advection correction was set to 10 dBZ^2. For the three-dimensional advection correction, the smoothing parameters were set as follows: $\beta = 50$ dBZ^2, $\gamma = 5$ dBZ^2, $\eta = 10$ dBZ^2, and $\lambda = 75$ dBZ^2. The smoothing parameters for the procedures were chosen so that they would produce spatial variations in the pattern translation components while still having the procedures converge. The additional smoothing parameters in the three-dimensional procedure were set to values that produced less horizontal variability than vertical variability for the horizontal pattern translation components and greater horizontal variability than vertical variability for the vertical pattern translation.

There are not large differences in the retrieved U and V between the two advection correction procedures, but the three-dimensional U and V have more spatial variability even though the three-dimensional procedure has additional smoothing in the vertical (Figs. 3.5, 3.6). Even though the general pattern of the U and V fields are similar, the upper levels in the two-dimensional procedure have pattern translation components that are significantly different from the levels below. At these levels there is less data coverage, so there is less data that can help constrain the U and V retrievals. The three-dimensional procedure does not have this problem since the additional data from the vertical dimension helps to prevent the abrupt changes in the vertical. The retrieved W from the three-dimensional procedure is fairly uniform and negative throughout most of the domain. This result seems reasonable as high reflectivity areas will typically descend unless collocated with an updraft.

Unfortunately, with real data tests it is impossible to know the true U, V, and W. However, one can compare this advection corrected reflectivity field to the actual reflectivity field observed by the radar. The retrieval that has more accurate pattern translation components should produce a more accurate reflectivity field. Therefore, the retrieved reflectivity field at 63.5 seconds (valid for 2139:40.5 UTC) from the first input time was compared to the gridded AIR reflectivity field from the 2139:40 UTC scan. This volume scan time is halfway between the two input times, so errors in the pattern translation components would result in the largest errors in reflectivity at this time. When comparing the retrieved reflectivity to the actual reflectivity it important to consider that errors in the reflectivity field due to bad pattern translation components are likely to be small. In fact, when pattern translation components are weak, the input reflectivity fields could have fairly low error when compared to another scan 60 seconds later. For this reason, it is useful to compare the reflectivity errors in a relative sense to a persistence analysis. A persistence analysis uses the reflectivity from the first input time as the retrieved reflectivity for the verification time. A small change in error statistics between the advection correction procedures could be large relative to the error statistics of the persistence analysis.

Like the pattern translation components, the retrieved reflectivities for the two procedures are similar (Fig. 3.7). One downside of the three-dimensional retrieval is the loss of data at the upper and lower edges of the volume. This data loss is caused by trajectories leaving the top and bottom of the data-coverage area due to vertical advection. The two-dimensional procedure does not suffer from this problem since trajectories stay on a single vertical level so data is only lost on the horizontal edges of the data coverage area. The bad pattern translation components at the top of the domain in the two-dimensional procedure do not significantly affect the reflectivity since many trajectories leave the data coverage area at these levels and cause there to be no estimate of reflectivity. In terms of root-mean-square error (RMSE), the persistence analysis has an RMSE of 3.049 dBZ. When using two-dimensional advection correction the RMSE drops significantly to 0.645 dBZ, which is a 78.85% error reduction from the persistence analysis. Finally, the RMSE of the three-dimensional reflectivity is 0.640 dBZ, which is a 79.01% reduction in error from the persistence analysis. Therefore, the three-dimensional procedure did not result in a better reflectivity analysis for this case, but it did produce one that was of similar quality. This result indicates that the three dimensional advection correction may not always result in better analyses. This, combined with the additional data loss at the top and bottom of the data coverage area in the three-dimensional procedure, indicates that the two-dimensional procedure may be more useful for advection correcting a scalar field, at least for simple cases with small vertical pattern translation. This test also showed, however, that the two-dimensional procedure can produce vertically inconsistent pattern translation components in real data cases. This suggests that for applications where the pattern translation components themselves are important, the three-dimensional advection correction will likely be more reliable. Overall, this real data test showed that the best advection correction procedure to use will likely be case and application dependent.

3.4 Limitation of Approach

Both spatially variable advection correction techniques can be a powerful tool for radar analysis products, but there is a limitation to the approach that has not been noted in meteorological literature. The procedures described in this chapter can be considered to be variations of the optical flow retrieval created by Horn and Schunck (1981) in the field of image processing. In fact, the cost function used by Horn and Schunck (1981),

$$J = \iint \left[\left(\frac{\partial R}{\partial t} + U\frac{\partial R}{\partial x} + V\frac{\partial R}{\partial y} \right)^2 + \beta \left|\nabla_h U\right|^2 + \beta \left|\nabla_h V\right|^2 \right] dxdy, \tag{3.36}$$

is almost equivalent to the one used by Shapiro et al. (2010) (the symbols used in this equation are different than those used in Horn and Schunck (1981) in order to be consistent with the symbols in the current work). The only differences between the two procedures is that Horn and Schunck (1981) was concerned with retrieving the optical flow (what this work calls pattern translation components) from a sequence of images while the Shapiro et al. (2010) technique and the three-dimensional version described in this chapter retrieve the scalar field at times between the two input times. There is no time integral in the Horn and Schunck (1981) cost function even though the scalar field has an inherent time dependence. The scalar tendency term in (3.36) is treated as a constant for each iteration and the iterations for solving U and V are done using a sequence of data from consecutive input times. Despite the slight differences, the pattern translation components are solved using similar Eular–Lagrange equations and, therefore, the properties of the Horn and Schunck (1981) procedure should apply to the advection correction procedures.

Horn and Schunck (1981) point out that if there are no smoothing terms, then at each grid point only the pattern translation component parallel to the gradient in the scalar field at that grid point can be determined. With the smoothing terms, the component of the pattern translation parallel to the the gradients is spread to other grid points, including those where the gradient is perpendicular to the pattern translation. This allows for the retrieved pattern translation vectors to not be parallel to the gradients in the scalar field. The insight from Horn and Schunck (1981) leads to two important considerations for the advection correction procedure. First, the smoothing parameter does not just control the spatial variability of the pattern translation components, as it has a critical importance for improving pattern translation components in regions with non-optimal gradients. Therefore, it will also control the accuracy of the overall procedure and the values that should be used will depend on the true pattern translation of the field and the orientation of the gradients in the scalar field. For example, if the scalar field has few regions with gradients that are optimally oriented with the pattern translation vector, then a larger smoothing parameter will be needed to obtain the correct orientation of the pattern translation vectors. Obviously, larger smoothing parameters come with the trade off of reduced spatial variability in the pattern translation components. The optimal smoothing parameter will be the value that balances information spreading and spatial variability. This leads into the second consideration, which is that there is an upper limit of accuracy for the procedure that is set by the true pattern translation of the field and the gradients in the field. For this example, consider a feature with only east–west oriented gradients that is surrounded by missing data and is moving towards the north. As is, the advection correction procedures will be unable to retrieve that northward advection. This is an extreme example, but it highlights that even simple pattern translation fields can have inaccurate solutions if the gradients of the scalar field are suboptimally oriented with respect to the pattern translation. Users of these advection correction procedures need to be aware of this limitation when using this approach, as this limitation can produce some confusing results in some circumstances. Future work on the advection correction problem should attempt to relate the gradients of the scalar in the dataset to the optimal value of the smoothing parameter to help automate the selection of the appropriate smoothing parameters.

3.5 Summary

A three-dimensional spatially variable advection correction procedure similar to the original two-dimensional Shapiro et al. (2010) procedure was developed. Two-dimensional spatially variable advection correction is not able to account for vertical advection, and therefore, vertical advection can be aliased into horizontal advection in the procedure. When applied to a volume of data, the two-dimensional procedure can also create nonphysical vertical variations in pattern translation components. The analytical dataset test highlights these potential deficiencies with the two-dimensional advection correction, and shows that the newly created three-dimensional procedure does not suffer from the same problems. However, for a real data test with relatively simple pattern translation components, both procedures produced similar horizontal pattern translation components and negligible differences in the retrieved reflectivity field. This suggests that two-dimensional spatially variable advection correction is a valid approach when the pattern translation field is simple. Even so, the results from the analytical test cannot be ignored. Therefore, the three-dimensional procedure could perform more reliably, but this comes with the trade off of additional data loss at the upper and lower boundaries of the data coverage region. Ultimately, users may have to test both procedures for their particular case and application when deciding which procedure to use.

Table 3.1: Ranges and RMSEs for the pattern translation components retrieved by the two- and three-dimensional spatially varying advection correction procedures for the analytical dataset described by Eq. 3.2.

	2D ADV	3D ADV
U Range	-650.191 – 33.932 m s^{-1}	9.952 – 10.010 m s^{-1}
V Range	-40.603 – 485.136 m s^{-1}	7.458 – 7.513 m s^{-1}
W Range	N/A	4.999 – 5.066 m s^{-1}
U RMSE	133.188 m s^{-1}	0.022 m s^{-1}
V RMSE	94.945 m s^{-1}	0.018 m s^{-1}
W RMSE	N/A	0.045 m s^{-1}

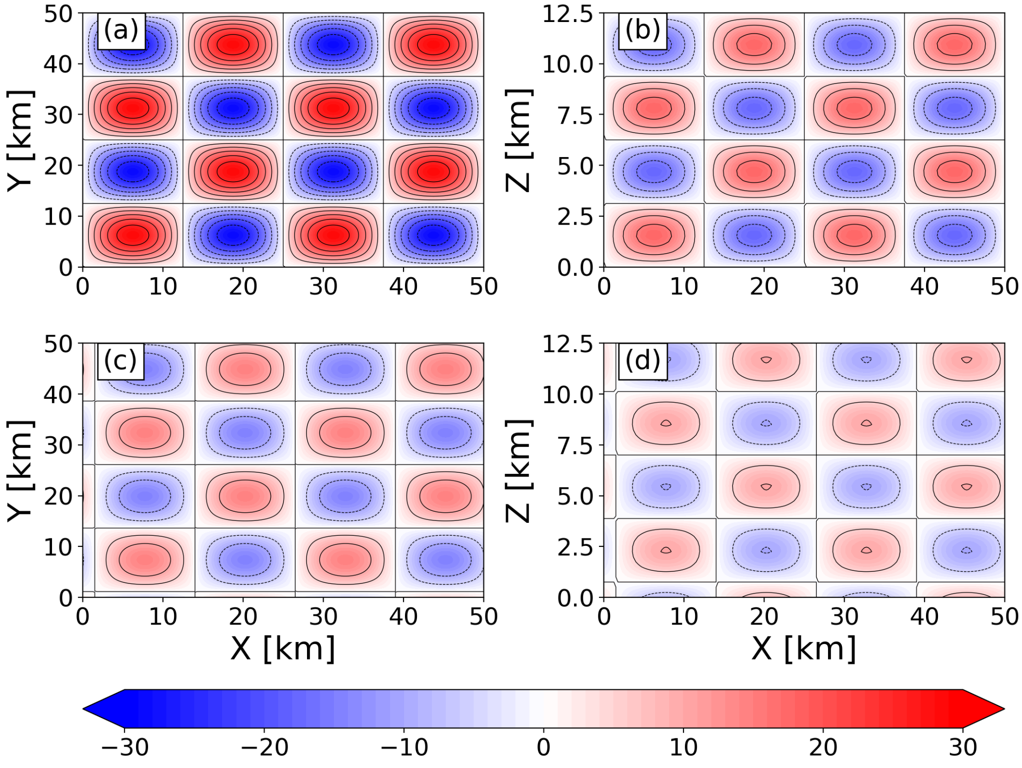

Figure 3.1: Field (unitless) described by Eq. 3.2 for a (left) horizontal cross-section at $z = 7.5$ km at (a) $T = 0$ s and (c) $T = 150$ s and (right) vertical cross-section at $y = 27.5$ km at (b) $T = 0$ s and (d) $T = 150$ s. Black contours are drawn for increments of 5.

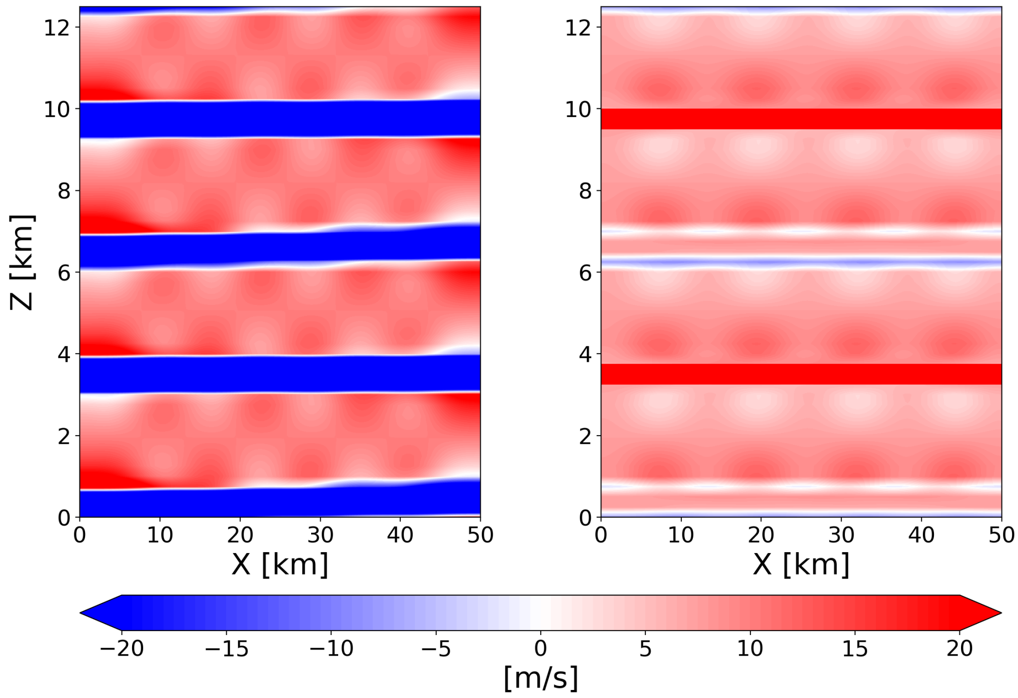

Figure 3.2: Vertical cross-sections at $y = 27.5$ of retrieved (left) U and (right) V from the two-dimensional spatially variable advection correction routine. The correct U is 10 m s^{-1} and the correct V is 7.5 m s^{-1}. The darkest blue and red shaded areas indicate values that exceed the range of the colorbar.

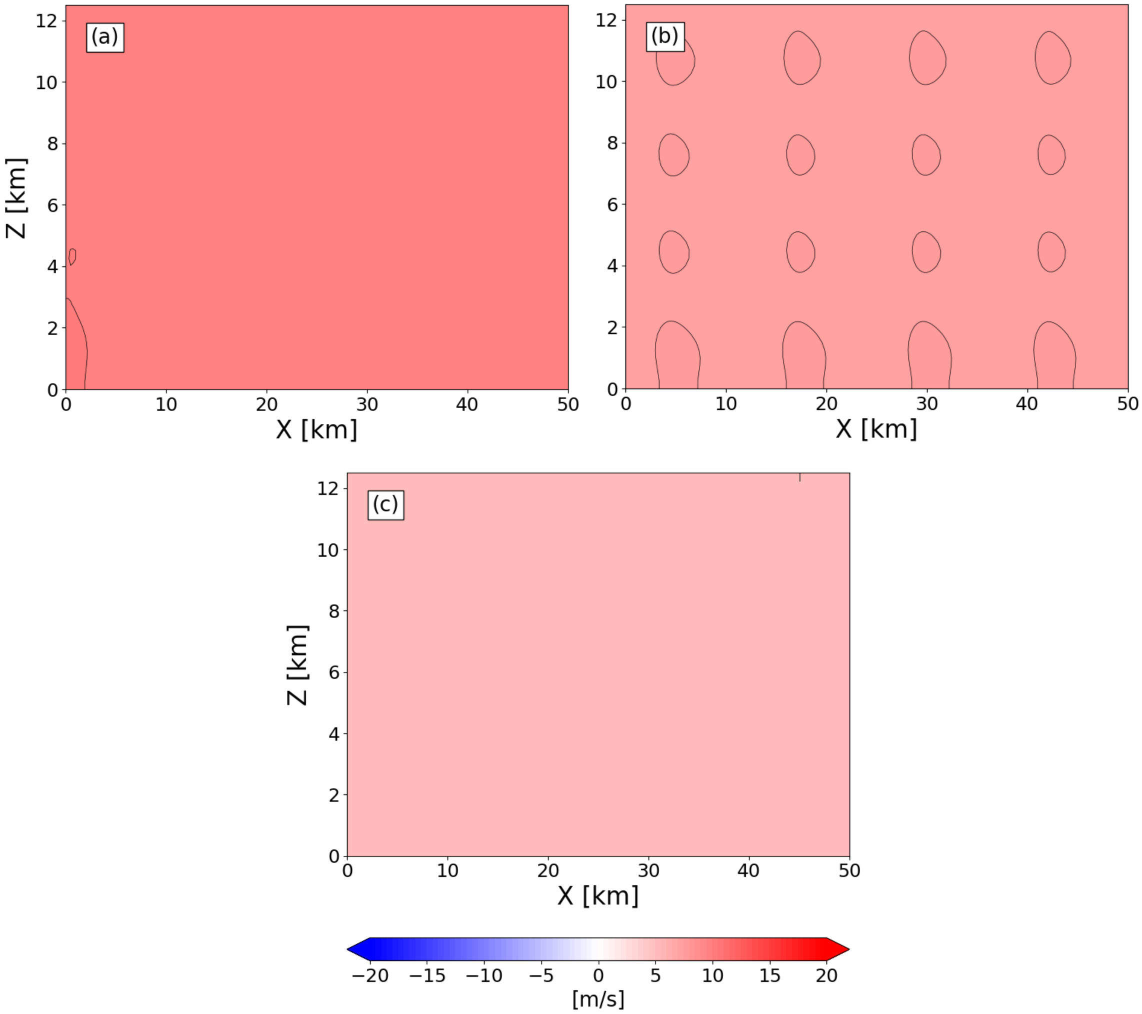

Figure 3.3: Vertical cross-sections at $y = 27.5$ of retrieved (a) U, (b) V, and (c) W from the three-dimensional spatially variable advection correction routine. Black contours are drawn every 0.5 m s^{-1}. The correct U is 10 m s^{-1}, V is 7.5 m s^{-1}, and W is 5 m s^{-1}.

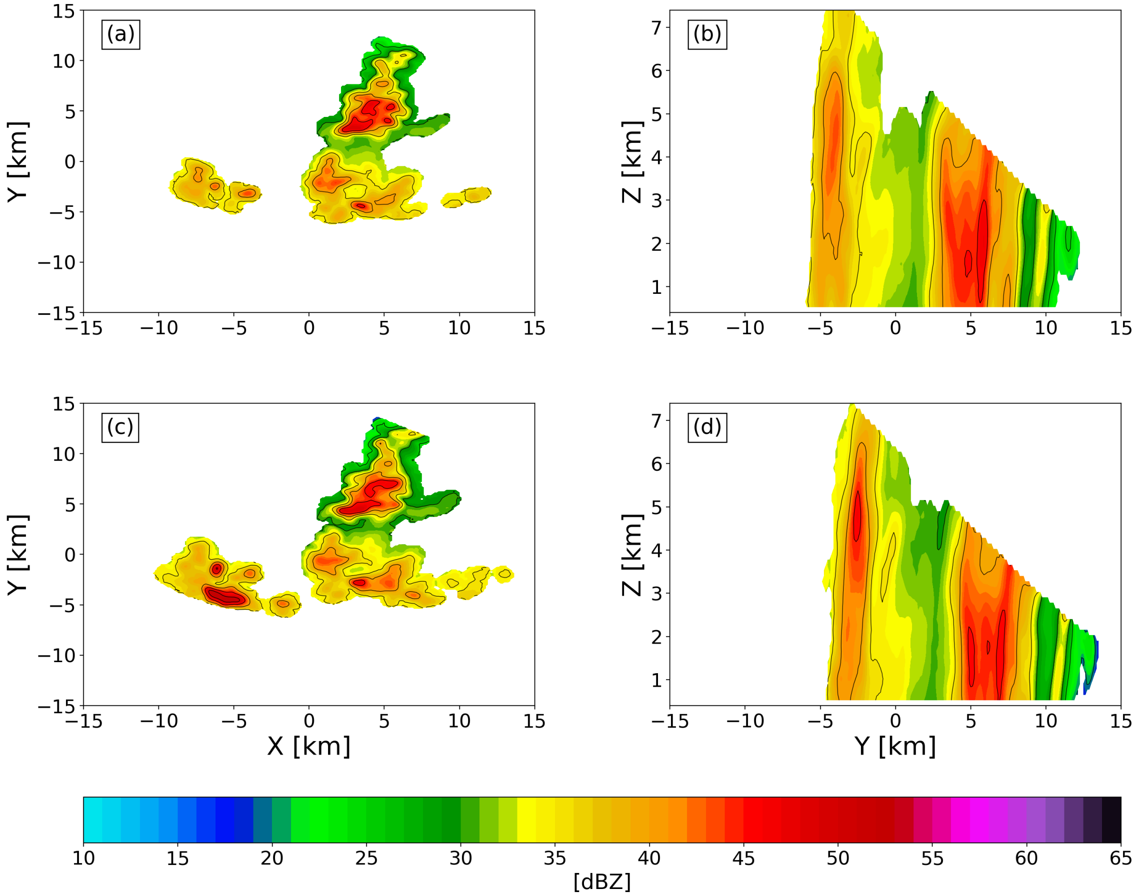

Figure 3.4: Reflectivity from the AIR on 4 Sept 2018 at (a),(c) 2138:37 and (b),(d) 2140:42 UTC. These times are used as the input data for the real data test of the advection correction procedures. (a) and (c) are horizontal cross-sections at $z = 1.25$ km AGL, while (b) and (d) are vertical cross-sections at $x = 3.125$ km.

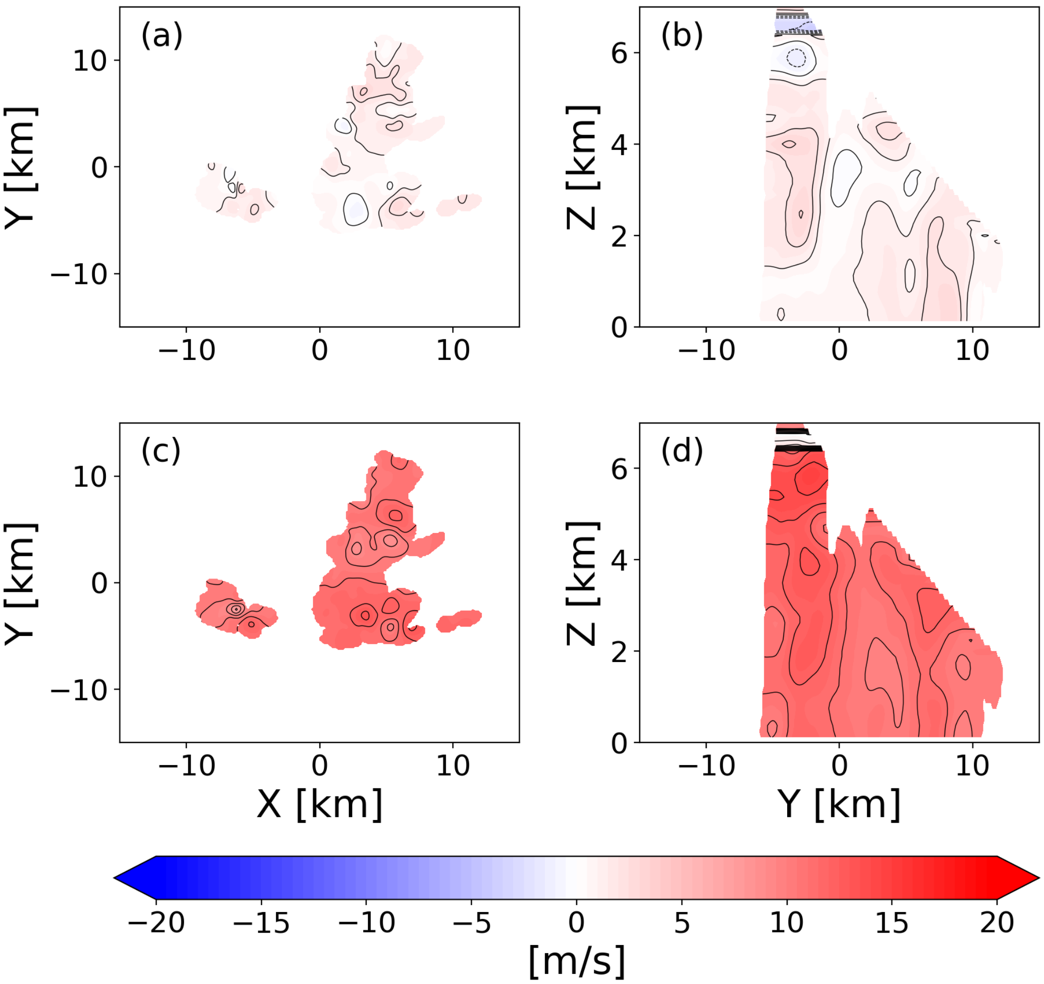

Figure 3.5: Retrieved (a),(b) U and (c),(d) V from the two-dimensional spatially variable advection correction. Cross-sections are located at (a),(c) $z = 1.25$ km AGL and (b),(d) $x = 3.125$ km.

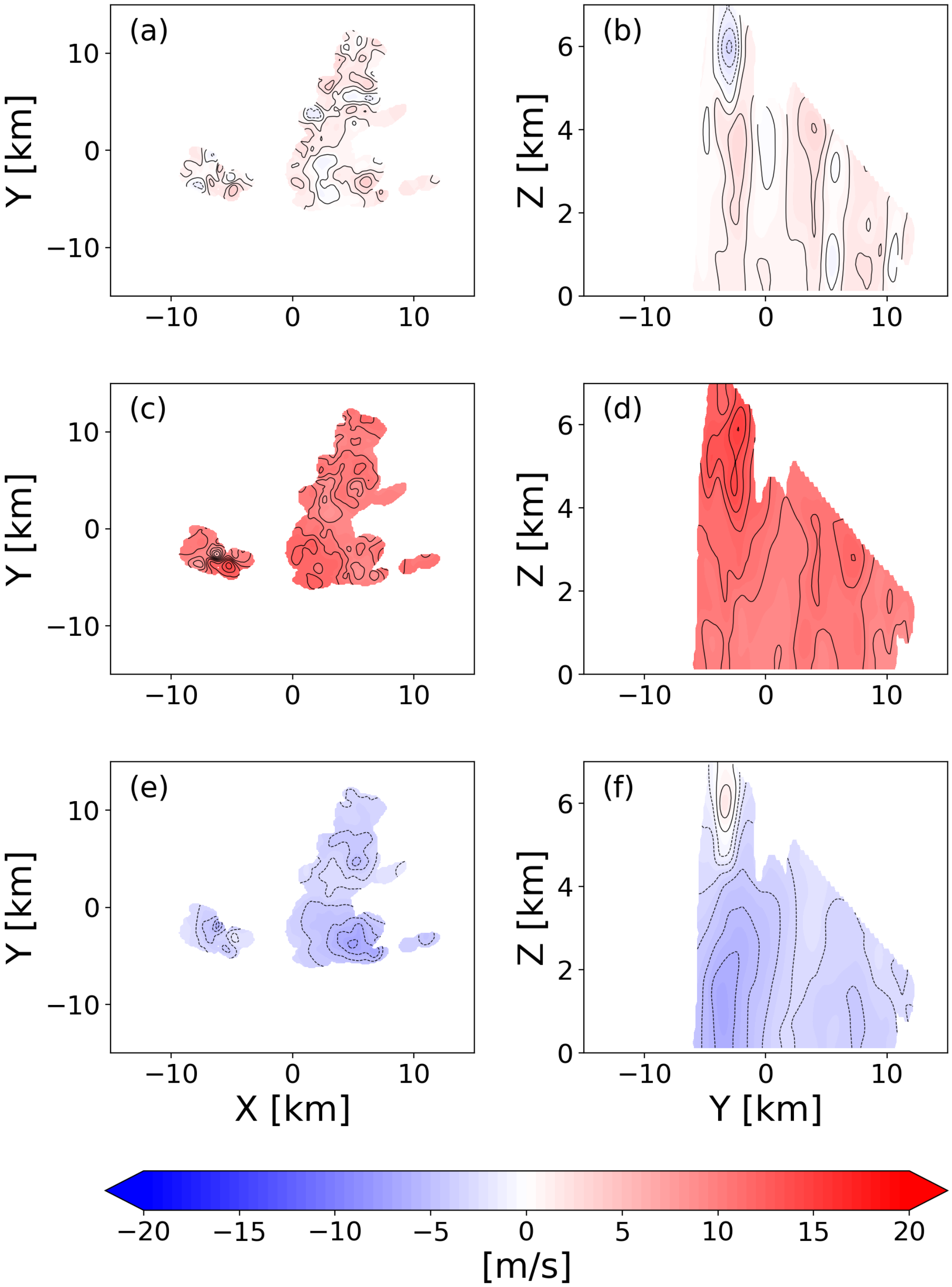

Figure 3.6: Retrieved (a),(b) U, (c),(d) V, and (e),(f) W from the three-dimensional spatially variable advection correction. Cross-sections are located at (a),(c),(e) $z = 1.25$ km AGL and (b),(d),(f) $x = 3.125$ km.

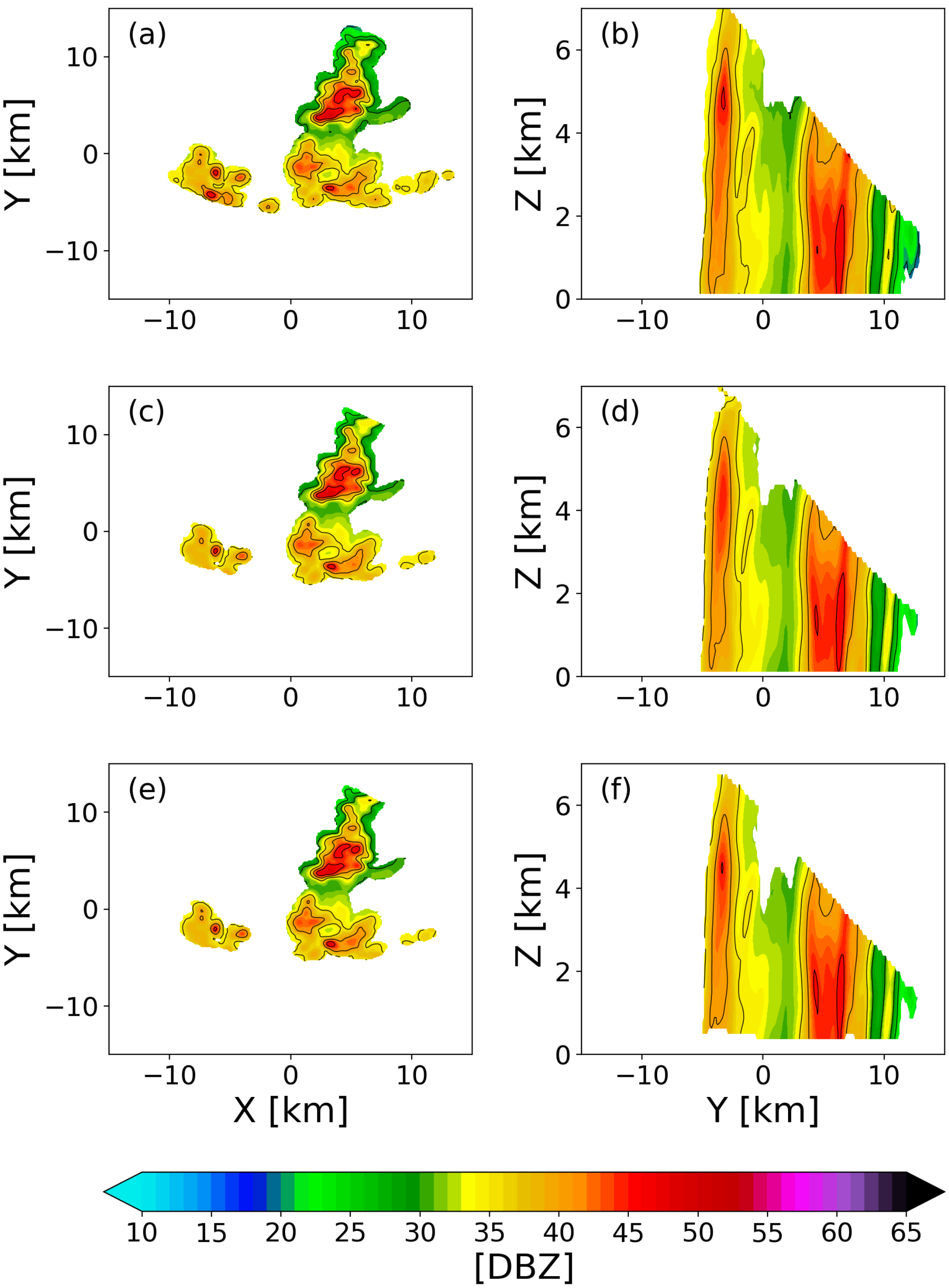

Figure 3.7: Gridded reflectivity at (a),(b) 2139:40 UTC from the AIR and retrieved reflectivity from the (c),(d) two-dimensional and (e),(f) three-dimensional advection correction. Cross-sections are from the same locations as Fig 3.6.

Chapter 4

Verification of Dual-Doppler Analysis Vertical Velocity Retrievals

4.1 Background

As discussed in Chapter 1, using a vertical vorticity equation constraint in DDA has the potential to improve vertical velocity retrievals. This has been shown in OSSE studies by Potvin et al. (2012b) and Dahl et al. (2019). However these studies found that the improvements with the vorticity constraint were limited to situations where data were unavailable or limited at low levels and the time between volume scans was small. With the dataset that was described in Chapter 2 the vorticity equation constrained DDA (hereafter referred to simply as vorticity constraint DDA) can be used with real rapid-scan radar data for the first time to determine if the OSSE results are representative of the DDA's skill with real radar data.

4.2 Variational Dual-Doppler Methodology

4.2.1 Description of Vertical Vorticity Equation Constraint Dual-Doppler Technique

The primary DDA technique used for this study is the variational dual-Doppler analysis procedure that includes a vertical vorticity equation constraint that was first developed by Shapiro et al. (2009) and modified by Potvin et al. (2012b) and Dahl et al. (2019). This variational procedure imposes observations, a mass conservation equation, a vertical vorticity equation, and smoothness as weak constraints for the three-dimensional wind field. Together these constraints form the following cost function:

$$J = J_O + J_M + J_V + J_S, \tag{4.1}$$

where J_O is the observational constraint, J_M is the mass conservation constraint, J_V is the vorticity constraint, and J_S is the smoothness constraint.

Specifically the observational constraint is

$$J_O = \lambda_O \left[\sum_{Cart_1} \left(V_{r_1}^{obs} - V_{r_1}^{a} \right)^2 + \sum_{Cart_2} \left(V_{r_2}^{obs} - V_{r_2}^{a} \right)^2 \right], \tag{4.2}$$

where $V_{r_1}^{obs}$ and $V_{r_2}^{obs}$ are the radial velocities from radar 1 and radar 2 and $V_{r_1}^{a}$ and $V_{r_2}^{a}$ are radial velocities calculated from the analysis wind field for radar 1 and radar 2. Since this study uses rapid-scan radar data and the longest scan-time between the two radars is 30 seconds, no correction for the scan rate of the radar data is made when calculating this penalty term. λ_O is the product of a non-dimensional constraint weight and normalization factor defined as

$$\lambda_O = C_O \left\{ \left(\frac{1}{M_1 + M_2} \right) \left[\sum_{Cart1} \left(V_{r_1}^{obs} \right)^2 + \sum_{Cart2} \left(V_{r_2}^{obs} \right)^2 \right] \right\}^{-1}, \tag{4.3}$$

where C_O is the non-dimensional constraint weight that is set by the user and M_1 and M_2 are the number of radial wind observations from radar 1 and radar 2.

The anelastic mass conservation equation is used for the mass conservation constraint, which leads to the following for J_M:

$$J_M = \lambda_M \sum_{Cart} \left(\frac{\partial u^a}{\partial x} + \frac{\partial v^a}{\partial y} + \frac{\partial w^a}{\partial z} + \frac{w^a}{\rho} \frac{d\rho}{dz} \right)^2, \tag{4.4}$$

where ρ is density, determined by

$$\rho(z) = \rho_o \exp\left(-\frac{z}{H} \right). \tag{4.5}$$

For this application, the scale height of the atmosphere H is set to 10 km, and ρ_o ,which is the density at $z = 0$, is 1 kg m^{-3}. The weighting parameter λ_M can be defined two different ways depending on the data available for the analysis. When no provisional wind analysis is available the mass conservation term is normalized by the azimuthal gradients in radial velocity so

$$\lambda_M = C_M \left\{ \left(\frac{1}{M_1 + M_2} \right) \left[\sum_{Cart} \left(\frac{1}{r_1} \frac{\partial V_{r_1}^{obs}}{\partial \theta} \right)^2 + \sum_{Cart} \left(\frac{1}{r_2} \frac{\partial V_{r_2}^{obs}}{\partial \theta} \right)^2 \right] \right\}^{-1}, \tag{4.6}$$

where r_1 and r_2 are the radial distance to the observation from radar 1 and radar 2, and C_M is the non-dimensional weighting parameter selected by the user. When there is a provisional analysis available the constraint is normalized with the horizontal divergence in the provisional analysis so

$$\lambda_M = C_M \left\{ \left(\frac{1}{N}\right) \left[\sum_{Cart} \left(\frac{\partial u^p}{\partial x} + \frac{\partial v^p}{\partial y} \right) \right]^2 \right\}^{-1}, \tag{4.7}$$

where N is the number of analysis points in the grid domain.

For the vorticity equation constraint, the vertical vorticity equation with no solenoidal term or mixing terms (Eq. 1.4) is used to form the following:

$$J_V = \lambda_V \sum_{Cart} \left[\frac{\partial \zeta}{\partial t} + u^a \frac{\partial \zeta^a}{\partial x} + v^a \frac{\partial \zeta^a}{\partial y} + w^a \frac{\partial \zeta^a}{\partial z} + \left(\frac{\partial v^a}{\partial z}\frac{\partial w^a}{\partial x} - \frac{\partial u^a}{\partial z}\frac{\partial w^a}{\partial y} \right) + \zeta^a \delta^a \right]^2 \tag{4.8}$$

where ζ is vertical vorticity, $\zeta = \partial v/\partial x - \partial u/\partial y$, and δ is horizontal divergence, $\delta = \partial u/\partial x + \partial v/\partial y$. The solenoidal term can be excluded from the constraint as it negligibly contributes toward the generation of vertical vorticity (Shapiro et al. 2009). Accurately estimating the local vorticity tendency, $\partial \zeta/\partial t$, has been the limiting factor on the accuracy of vorticity constraint dual-Doppler retrievals. The calculation of this term is discussed in a following section. The vorticity tendency calculation requires a provisional wind analysis, so two definitions of λ_V are not necessary. Therefore,

$$\lambda_V = C_V \left\{ \left(\frac{1}{N}\right) \left[\sum_{Cart} \left(\frac{\partial \zeta}{\partial t} + u^p \frac{\partial \zeta^p}{\partial x} + v^p \frac{\partial \zeta^p}{\partial y} + \zeta^p \delta^p \right)^2 \right] \right\}^{-1}, \tag{4.9}$$

where C_V is the non-dimensional weighting parameter set by the user.

Finally, the smoothness constraint is

$$\begin{aligned} J_S = \lambda_{S_1} \sum_{Cart} \left[\left(\frac{\partial^2 u^a}{\partial x^2} \right)^2 + \left(\frac{\partial^2 u^a}{\partial y^2} \right)^2 + \left(\frac{\partial^2 v^a}{\partial x^2} \right)^2 + \left(\frac{\partial^2 v^a}{\partial y^2} \right)^2 \right] + \\ \lambda_{S_2} \sum_{Cart} \left[\left(\frac{\partial^2 u^a}{\partial z^2} \right)^2 + \left(\frac{\partial^2 v^a}{\partial z^2} \right)^2 \right] + \lambda_{S_3} \sum_{Cart} \left[\left(\frac{\partial^2 w^a}{\partial x^2} \right)^2 + \left(\frac{\partial^2 w^a}{\partial y^2} \right)^2 \right] + \\ \lambda_{S_4} \sum_{Cart} \left(\frac{\partial^2 w}{\partial z^2} \right)^2 . \end{aligned} \tag{4.10}$$

As in Potvin et al. (2012b) and Dahl et al. (2019), all DDAs were calculated with $\lambda_{S_1} = \lambda_{S_2} = \lambda_{S_3} = \lambda_{S_4} = \lambda_S$. The non-dimensionalization for this constraint also depends on if there is a provisional analysis available, so there are two definitions for λ_S:

$$\lambda_S = C_S \left\{ \left(\frac{1}{M_1 + M_2} \right) \left[\sum_{Cart} \left(\frac{1}{r_1} \frac{\partial^2 V_{r_1}^{obs}}{\partial \theta^2} \right)^2 + \sum_{Cart} \left(\frac{1}{r_2} \frac{\partial^2 V_{r_2}^{obs}}{\partial \theta^2} \right)^2 \right] \right\}^{-1}, \tag{4.11}$$

if there is no provisional analysis available and

$$\begin{aligned} \lambda_S = C_S \Bigg\{ \left(\frac{1}{N} \right) \sum_{Cart} \Bigg[\left(\frac{\partial^2 u^p}{\partial x^2} \right)^2 + \left(\frac{\partial^2 u^p}{\partial y^2} \right)^2 + \left(\frac{\partial^2 u^p}{\partial z^2} \right)^2 + \left(\frac{\partial^2 v^p}{\partial x^2} \right)^2 + \\ \left(\frac{\partial^2 v^p}{\partial y^2} \right)^2 + \left(\frac{\partial^2 v^p}{\partial z^2} \right)^2 \Bigg] \Bigg\}^{-1}, \end{aligned} \tag{4.12}$$

if a provisional analysis is available, where C_S is a non-dimensional weighting parameter set by the user.

One may notice that (4.7), (4.9), and (4.12) do not include w in the normalization factors. The reason for this is that w in the provisional analysis is likely to be less accurate than the provisional u and v, and since this DDA approach is used to improve w retrievals, it would not be appropriate to use w in the normalization. If w was accurate in the provisional retrievals then there would be no reason to run the vertical vorticity constraint DDA. The normalization factors are included in the constraints to reduce the tuning required for the non-dimensional weights of the constraints. However, even with the normalization factors some tuning is necessary to obtain the most accurate DDAs. For this study, $C_O = 1$, $C_M = 0.001$, and $C_S = 0.0001$ were used for all provisional DDAs (there is no vorticity equation constraint in the provisional DDAs so C_V is not applicable), and $C_O = 1$, $C_M = 0.3$, $C_V = 0.1$, and $C_S = 0.0001$ for the analysis DDA runs. For analysis DDAs that do not use the vorticity equation constraint, the values of C_O, C_M, and C_S remain the same as the analysis DDA with the vorticity constraint. The values chosen for the provisional DDA were the same as those used in Dahl et al. (2019). The weights for the analysis DDA were modified from those used in Dahl et al. (2019) as the dataset used for this study required a higher weighting of the vorticity equation constraint in order for the constraint to have an impact on the wind retrievals.

4.2.2 Vorticity Tendency Calculation

The calculation of the vorticity tendency underpins the need for rapid-scan radar for DDAs that use the vorticity equation constraint. Wind fields from consecutive analysis times are needed to calculate this time-tendency term. Potvin et al. (2012b) and Dahl et al. (2019) used consecutive provisional DDAs for the vorticity tendency calculation. Provisional DDAs can be used for this calculation as the u and v components in even simple DDA techniques are typically well constrained by the observational constraints. However, even with accurate provisional horizontal wind retrievals, when the time between two provisional analyses is large, discretization errors in the vorticity tendency calculation increase, which degrades the performance of the DDA.

The calculation of the vorticity tendency occurs outside of the DDA retrieval and the field is included as input for the DDA program. Therefore, vorticity tendency remains constant throughout the minimization of (4.1). There are three ways that the vorticity tendency is computed. The first method is a simple centered difference of vorticity fields from provisional retrievals from the volume scans directly before and after the analysis time so that

$$\frac{\partial \zeta}{\partial t}(x,t^a) = \frac{\zeta^p(x,t^a+\tau) - \zeta^p(x,t^a-\tau)}{2\tau}, \tag{4.13}$$

where τ is the time between volume scans. This technique is most susceptible to discretization error when τ becomes large, but the Dahl et al. (2019) OSSE study found that when τ is sufficiently small (10–30 seconds) this technique provides estimates of the vorticity tendency that are accurate enough to improve vertical velocity retrievals over DDAs that do not include a vorticity constraint. However, the vertical velocity retrievals became significantly degraded when τ was longer than 30 seconds.

The second method that is used to calculate the vorticity tendency is the u and v advection correction method first used by Dahl et al. (2019). In this method, the Shapiro et al. (2010) two-dimensional advection correction procedure is applied to the u and v fields from the provisional retrievals to shorten the discrization interval of the centered difference of the provisional vorticity fields so that

$$\frac{\partial \zeta}{\partial t}(x,t^a) = \frac{\zeta(x,t^a+\Delta t) - \zeta(x,t^a-\Delta t)}{2\Delta t}, \tag{4.14}$$

where Δt is the computational timestep used in the advection correction procedure. Dahl et al. (2019) found that this method produced the most consistent DDA vertical velocity results as this method had less degradation of the w field with increasing volume scan time, however when τ was increased to 150 seconds this method still produced less accurate w fields than a DDA that did not use the vorticity equation constraint. Since this method uses the two-dimensional advection correction, the advection correction is conducted separately on each level in the analysis domain. This has the potential to create vertical discontinuities in the u and v fields due to the discontinuities in U and V that were shown and discussed in Chapter 3. These errors would be exacerbated with larger τ as smaller changes in the pattern translation components can lead to larger horizontal displacement error than when τ is small.

The third and final method for calculating the vorticity tendency also uses advection correction on the horizontal wind components of the provisional retrievals, but instead of using the two-dimensional advection correction procedure, the three-dimensional procedure described in Chapter 3 is used. This procedure has not been previously used to calculate the vorticity tendency, but since the whole analysis volume is corrected at once it should not be subject to the discontinuity errors that can occur with the two-dimensional technique. One downside of using the three-dimensional advection correction technique is that the additional data loss at the top and bottom of the data coverage area leads to the vorticity constraint being applied at fewer locations, as the constraint can only be applied at locations with an estimate of the vorticity tendency.

4.2.3 Retrieval Procedure

The variational dual-Doppler procedure begins with the gridding of the RaXpol and AIR data (described in Chapter 2) with a Cressman filter. For this study, the dual-Doppler analysis was conducted separately at 125-m and 250-m resolution. The Cressman radius used for both resolutions was 400 m. After the RaXPol and AIR are gridded, a two-pass Leise filter (Leise 1982) is applied to the gridded data. This technique of using a smaller Cressman radius and applying a Leise filter afterwards was found to produce more accurate gridded datasets than using a larger Cressman radius (Dahl et al. 2019). Provisional DDAs were conducted in a 30 × 30 × 7 km domain, but the final analyses were conducted in a 25 × 25 × 7 km domain (Fig. 4.1). The reduced horizontal extent in the analysis domain is due to data loss at the edges of the DDA domain when advection correction is used to calculate the vorticity tendency. The dual-Doppler coverage area is smaller than the domain area, but the variational procedure can still perform single Doppler retrievals in the regions with only RaXPol data. After application of the Leise filter, provisional DDAs with no vorticity equation constraint are conducted. If the final dual-Doppler retrieval does not contain a vorticity equation constraint (i.e., running the variational procedure described above with $C_v = 0$) then the provisional retrieval is only performed for the analysis time. This provisional retrieval is used to calculate the normalization factor for the mass conservation constraint. If a vorticity equation constraint is applied, provisional retrievals are conducted for the analysis time t^a and also for the $t - \tau$ and $t + \tau$ scans. These provisional retrievals are used for the vorticity tendency calculation, and the analysis time provisional retrieval is also used to calculate the normalization factors for the mass conservation and vertical vorticity constraints. Once the provisional retrievals are obtained and the vorticity tendency is calculated using one of the three methods described in the previous subsection, the final analysis time DDA is performed.

4.3 Experiment Design

4.3.1 Reference Dual-Doppler Analyses

Since this study aims to determine if the vorticity constraint DDA improves estimates of the vertical velocity field, reference retrievals that do not use the vorticity equation constraint are needed for comparison. Two different techniques are used as a reference. The first technique is the variational DDA described above with no vorticity equation constraint. The second reference DDA is the Brandes (1977) DDA technique that directly integrates the anelastic mass conservation equation to obtain vertical velocity. This is considered to be a "traditional" DDA technique. A traditional DDA and variational DDA with no vorticity equation constraint are both used as a reference to ensure the improvements are not solely due the variational nature of the vertical vorticity constraint DDA.

The traditional DDA used is the same as the iterative one used by Dahl et al. (2019). Specifically, this DDA is conducted on a Cartesian grid and first obtains an estimate of u and v using Eq. (5) from Ray et al. (1980):

$$\begin{aligned} u(x,y,z) = {} & \frac{r_1 v_1 (y-y_2) - r_2 v_2 (y-y_1) - w_t[(z-z_1)(y-y_2) - (z-z_2)(y-y_1)]}{(x-x_1)(y-y_2) - (x-x_2)(y-y_1)} \\ & - w\frac{(z-z_1)(y-y_2) - (z-z_2)(y-y_1)}{(x-x_1)(y-y_2) - (x-x_2)(y-y_1)}, \end{aligned} \tag{4.15}$$

$$\begin{aligned} v(x,y,z) = {} & \frac{r_2 v_2 (x-x_1) - r_1 v_1 (x-x_2) - w_t[(z-z_2)(x-x_1) - (z-z_1)(x-x_2)]}{(x-x_2)(y-y_1) - (x-x_1)(y-y_2)} \\ & - w\frac{(z-z_2)(x-x_1) - (z-z_1)(x-x_2)}{(x-x_2)(y-y_1) - (x-x_1)(y-y_2)}, \end{aligned} \tag{4.16}$$

where x_1, y_1, z_1 and x_2, y_2, z_2 are the Cartesian coordinates of the radar 1 and radar 2 respectively and w_t (< 0) is the particle terminal fall velocity, which is obtained using the Atlas et al. (1973) empirical relationship between reflectivity and terminal fall velocity with a density correction

$$w_t = aR^b \left(\frac{\rho_o}{\rho}\right)^{0.4} \tag{4.17}$$

with a = -2.65 and b = 0.114, where w_t is in m s^{-1} and R is in mm^6 m^{-3}. This terminal fall speed relationship is designed for liquid drops, so the relationship breaks down above the freezing level. The sensitivity of the DDA to the terminal fall speed calculation was tested and it was found that DDA was not sensitive to the terminal fall speed calculation. In fact, even excluding the terminal fall speed from the calculations did not significantly affect the retrieval. For the first calculation of (4.15) and (4.16), w is zero. After obtaining u and v, w is calculated by integration of the anelastic mass conservation equation, which yields the following equation for w,

$$w(x,y,z) = \frac{\rho(z-\Delta z)w^a(x,y,z-\Delta z)}{\rho(z)} - \frac{0.5\Delta z\left[\rho(z-\Delta z)\delta(x,y,z-\Delta z)+\rho(z)\delta(x,y,z)\right]}{\rho(z)}. \quad (4.18)$$

In this DDA, only upward integration is performed so the impermeability condition, $w(x,y,0)$ = 0, is applied as the boundary condition for the integration. In areas of the domain with a data void between the ground and the lowest available data level, the divergence in these data voids is set to 0.8 times the divergence at the lowest available level, as in Brandes (1977). In regions with data voids in between two data levels the divergence in the data void is a linear interpolation of the divergence above and below the data void.

Once w is obtained, the procedure repeats with a new u and v found using (4.15) and (4.16). This new u and v is then used to find a new w field. This continues until the change in the w falls below a specified tolerance, which was set to 0.5 m s^{-1}. Dahl et al. (2019) found that applying a Leise filter to the u and v fields before calculating w and then to w after it is calculated from (4.18) improved the traditional DDA results, therefore, a Leise filter is applied in a similar manner in this study.

4.3.2 Dual-Doppler Retrievals Performed

In the 4 Sept 2018 dataset, the AIR and RaXPol operated with constant volume scan times of 9 and 30 seconds, respectively. According to past OSSE studies (Potvin et al. 2012b;

Dahl et al. 2019), these volume scan times should be small enough to retrieve more accurate vertical velocities using the vorticity constraint DDA than with the DDAs that do not use a vorticity equation constraint. This is useful for testing the vorticity constraint DDA with optimal rapid-scan data, however, one goal of this study is to evaluate the impact of the time between volume scans on the w retrievals from the vorticity constraint DDA. One can test the impact of the time between volume scans on the DDA by varying Δt for the calculation of the vorticity tendency from the provisional DDA retrievals. For example, vorticity constraint DDAs with 90 s between volume scans can be tested by calculating the vorticity tendency from the provisional retrievals 90 s before and after the analysis time. It is important to note that the results from such tests will not include advection errors that would occur when volume scan times are longer, since the true volume scan time for the data that was used for the provisional DDA is still 30 s for RaXPol and 9 s for the AIR.

The vorticity constraint DDAs were performed for Δt of 30 s, 90 s, and 150 s. For each of the times between volume scans, a set of DDAs were conducted for each of the three methods for calculating the vorticity tendency. The DDAs were conducted using the 4 Sept 2018 dataset from 2121:11 to 2148:10 UTC. This time period was chosen as it overlaps with the verification data provided by the SMART-R3 (Fig. 2.5). All of these DDA experiments were performed separately at 125-m and 250-m resolution. Overall, with the two reference DDAs and the vorticity DDA experiments, 22 DDA experiments were performed. A summary of the experiments is shown in Table 4.1. This table also includes the abbreviations that will be used in the rest of the Chapter to refer to each of the DDA experiments.

4.3.3 Verification Method

In past OSSE dual-Doppler verification studies (Potvin et al. 2012b; Dahl et al. 2019) a single DDA was compared to the actual wind fields from the model run that was used to produce simulated radar observations. This allowed for a simple verification of the DDA retrievals. Unfortunately, when using real radar data, verification of the dual-Doppler retrievals is more complicated, as the verification of the wind field has to come from observations. Therefore, it is particularly challenging to verify w, as observations of vertical motion are uncommon, and often only provide a profile at a single location. For this study, the SMART-R3 was used as the verification source for the dual-Doppler w retrievals. Since there is only one verification profile for w, the verification of the DDAs is conducted over multiple scans to assess the performance of the retrieval for different portions of the storm as it passes over the SMART-R3. Obviously, only having one verification point limits the assessment of the DDA retrievals. Even though vertical motion for different regions of the storm is captured by verifying over multiple DDA times, the scan geometry for the verification point is unchanged, which makes it impossible to assess how the retrieval performs with varying cross-beam angles and vertical data availability.

Additionally, using a vertical-pointing radar as the verification source has its own difficulties. The radial velocities measured by SMART-R3 are a combination of the vertical motion of the air, and the terminal fall velocity of the precipitation. Therefore, in order to use the SMART-R3 as a verification for w, terminal fall velocity needs to be removed from the raw radial velocities. Equation (4.17) is used to obtain the terminal fall velocity (Fig. 4.2). This relationship is meant for liquid drops and is not applicable at the melting layer due to bright banding or above the freezing level for frozen precipitation, so the SMART-R3 data will only be used for verification below 4.5 km ASL, the freezing level on this day. Using (4.17) to estimate terminal fall velocity introduces uncertainty into the vertical velocity observations used for the verification as the reflectivity-terminal fall velocity relation is only accurate to within 1 m s^{-1} for reflectivity less than 40 dBZ (Atlas et al. 1973). As noted in (Atlas et al. 1973) the relationship is less certain at lower reflectivities as the raindrop distributions creating low reflectivities can vary from a large number of small drops in a drizzle situation to a small number of large drops at the edge of a convective storm. Additionally, there is already uncertainty in the SMART-R3 reflectivities due to the bias that needed to be removed from them. For these reasons, the verification of the vertical velocity retrievals at the SMART-R3 verification point will be focused on the verification statistics that are used to construct Taylor diagrams (Taylor 2001). A Taylor diagram uses the relationship between the following three statistics to show them all on one diagram: centered root-mean-square error,

$$CRMSE = \sqrt{\frac{1}{N}\sum_{n=1}^{N}\left[\left(w_n - \overline{w}\right) - \left(w_{SR_n} - \overline{w_{SR}}\right)\right]^2}, \tag{4.19}$$

correlation coefficient,

$$CC = \frac{\sum_{n=1}^{N}\left(w_n - \overline{w}\right)\left(w_{SR_n} - \overline{w_{SR}}\right)}{\sqrt{\sum_{n=1}^{N}\left(w_n - \overline{w}\right)^2\left(w_{SR_n} - \overline{w_{SR}}\right)^2}}, \tag{4.20}$$

and standard deviation,

$$SD = \sqrt{\frac{1}{N}\sum_{n=1}^{N}\left(w_n - \overline{w}\right)^2}; \tag{4.21}$$

where an overbar denotes a mean, n is an index for the points included in the verification, N is the number of points included in the calculation, and w_{SR} is the SMART-R3 vertical velocities. In all of these metrics, the mean of the data is irrelevant, and therefore, they are unaffected by a systematic bias in the observed vertical velocity data that may be present due to the terminal fall velocity calculation. The choice of terminal fall speed calculation could still affect the Taylor diagram statistics due to the non-linear relationship between reflectivity and terminal fall speed, but the Taylor diagram statistics were found to be insensitive to other terminal fall speed relationships.

4.4 Results

4.4.1 Qualitative Verification at SMART-R3 Location

The TRAD and NOVORT vertical velocities are very similar to each other at the SMART-R3 verification point for both the 125-m (Fig. 4.3) and 250-m (Fig. 4.4) resolution DDA. This similarity is not surprising since there is no data gap between the lowest analysis level and the ground in this dataset, so the NOVORT DDA does not gain much of an advantage over the TRAD DDA. Both DDAs resolve updrafts at 2130 UTC and 2147 UTC. The SMART-R3 (Fig. 4.2c) also observed updrafts at these time, however, they are much weaker than the updrafts retrieved by the TRAD and NOVORT DDAs. The TRAD and NOVORT DDAs also do not resolve the updraft at 2136 UTC, but at this time the verification point is near the edge of a data void, which may have affected the retrievals at this point. The excessive amplitudes of the vertical velocities is greater at 125-m resolution than 250-m resolution. This is likely due to the larger magnitude of divergence at the finer resolution. These TRAD and NOVORT DDAs are not adept at resolving the structure of the updrafts and downdrafts. An example of this would be the updraft at 2130 UTC. The SMART-R3 observed this updraft either having a tilted structure or descending with time, while the DDAs retrieved a more vertically oriented updraft that had a consistent depth.

The amplitudes of the updrafts retrieved with the 30s_VORT_BF DDA (Figs. 4.5a and 4.6a) are closer to the SMART-R3 observations. These retrieved vertical velocities also seem to have more detail than the those retrieved with the TRAD and NOVORT DDAs. One troubling detail in the 30s_VORT_BF results is the large amplitude downdraft that occurs at 2136 UTC above 3 km. The SMART-R3 observes an updraft at this time and location so this downdraft is a large error. It is important to note, however, that the TRAD and NOVORT both struggled retrieving this updraft observed by the SMART-R3. The verification point is close to the edge of a data void at this time, so the data used for the retrievals in this location could actually be an extrapolation due to the Cressman filter. The proximity of the data void is particularly important with the vorticity constraint DDAs as regions close to the data void may not actually have estimates of the vorticity tendency due to missing data, and therefore the vorticity constraint would not be applied. The differences between the 125-m and 250-m 30s_VORT_BF DDA are mostly resolution differences. The 250-m version's vertical velocities have less structure, and the amplitudes of the vertical velocities are lower than in the 125-m version.

For the 90s_VORT_BF (Figs. 4.5b and 4.6c) and 150s_VORT_BF DDAs (Figs. 4.5c and 4.6c) one sees how the longer volume scan time can degrade vertical velocity retrievals when using a vorticity equation constraint. Large-amplitude updrafts are retrieved just after 2130 UTC for both the 125-m and 250-m versions of the DDAs. Following passage of this updraft a large amplitude downdraft is particularly pronounced in the 125-m version of the DDAs. The vertical velocities after 2142 UTC also deviate from those observed by the SMART-R3. Interestingly, the 90s_VORT_BF and 150s_VORT_BF DDAs seem to perform as well or better than the 30s_VORT_BF at some times. These DDAs are particularly skillful at retrieving the small downdraft feature surrounded by updraft after 2127 UTC, and they do not have the large amplitude downdraft around 2136 UTC. This highlights the uncertainty with using the brute force technique for calculating the vorticity tendency with longer volume scans; it will occasionally work, but in other cases it can produce catastrophic errors.

When the two-dimensional advection correction method is used for calculating vorticity tendency, the high amplitude updrafts and downdrafts that were present in the 90s_VORT_BF are no longer present and the structure of the vertical velocities is much improved (Figs. 4.7 and 4.8). The region above 3 km at 2136 UTC does acquire the incorrect downdraft in the 90s_VORT_2DADV DDA. Again, this is likely due to the proximity to the data void. The data void issue is a larger issue when using advection correction due to the loss of data at the edges of the data coverage regions. The updraft at 2147 UTC is too weak in all the two-dimensional advection correction DDAs, but this is particularly apparent at the 250-m resolution. These DDAs also incorrectly retrieve a strong downdraft following this updraft. At that time the verification point is again close to the data void, and no vorticity constraint is applied at that time and location. On the other hand, the structure of the retrieved updraft at 2130 UTC is impressive when two-dimensional advection correction is used, especially in the 90s_VORT_2DADV DDA. Even with using the two-dimensional advection correction the 125-m 150s_VORT_2DADV still produces a strong updraft–downdraft pair between 2130 and 2133 UTC, which suggests that the two-dimensional advection correction method is still not providing an accurate enough estimate of the vorticity tendency to improve the vertical velocity retrievals.

Using the three-dimensional advection correction technique for calculating the vorticity tendency does not result in large changes in the vertical velocities at the verification point in the 30s_VORT_3DADV and the 90s_VORT_3DADV DDAs (Figs. 4.9 and Figs. 4.10). It does, however, improve the 125-m resolution 150-s volume scan DDA retrieved vertical velocities as the large amplitude updraft–downdraft pair is no longer present and the retrieved vertical velocities look similar to those in the 90s_VORT_3DADV DDA. There was not much improvement in the 250-m 150s_VORT_3DADV DDA, but the 250-m 150s_VORT_2DADV did not have apparent errors that could be improved upon. The improvement in the 150s_VORT_3DADV DDA vertical velocities suggest that the three-dimensional advection correction technique for calculating the vorticity tendency may improve the vorticity constraint DDAs, especially for longer volume scan times.

4.4.2 Objective Verification at SMART-R3 Location

The Taylor diagram statistics of CRMSE, correlation coefficient, and standard deviation were calculated at the SMART-R3 verification point for the entire time period for each DDA experiment. The SMART-R3 data were linearly interpolated to the same time–height grid used in the DDAs experiments. For this verification, times and heights that had no vertical velocity estimate in one of the DDA experiments for that resolution were not included in the statistics. This was done so no experiment was rewarded or penalized for performing a vertical velocity retrieval where another experiment could not. For the 125-m DDA, the TRAD and NOVORT experiments had the largest CRMSE (Fig. 4.11). Interestingly, these experiments had the highest correlation coefficient, but the CRMSE fell because the standard deviation of the retrieved vertical velocity was much larger than the

SMART-R3-observed vertical velocity standard deviation. This indicates that the main errors in the TRAD and NOVORT are due to the amplitudes of the retrieved vertical velocities being too large. The 30s_VORT_BF has a lower CRMSE than the TRAD and NOVORT. This reduction in RMSE is mostly due to the improvement in the amplitudes of the vertical velocity field as the standard deviation is closer to the observation standard deviation, but the correlation coefficient is lower. The lower correlation coefficient is mostly due to the downdraft above 3 km at 2136 UTC. The 90s_VORT_BF and 150s_VORT_BF do not have this downdraft, so the correlation coefficient is higher for these DDAs, but the standard deviation of the retrieved vertical velocities is also higher, resulting in greater CRMSE. It is important to note that the 90s_VORT_BF and 150s_VORT_BF have large amplitude updrafts shortly after 2130 UTC, which is when there is no SMART-R3 data for the verification. Therefore, the objective verification metrics overestimate the skill of these two DDAs. When advection correction is used for calculating the vorticity tendency the 90-s and 150-s DDAs have verification statistics that are similar to the 30s_VORT_BF DDA. The 90s_VORT_3DADV and 150s_VORT_3DADV DDAs have slight improvements in CRMSE over the 90s_VORT_2DADV and 150s_VORT_2DADV DDAs, respectively, but these improvements are much smaller than the improvements over the 90s_VORT_BF and 150s_VORT_BF. Using advection correction on the 30-s volume scans resulted in the CRMSE slightly increasing, which suggests that advection correction for 30-s scans for this case is not necessary and can even slightly hurt the DDA performance. In terms of lowest CRMSE, the 90s_VORT_3DADV is the best DDA.

For the 250-m DDAs, the CRMSE of the TRAD and NOVORT DDAs is lower than that of the 125-m versions due to a lower standard deviation of the retrieved vertical velocity (Fig. 4.12). None of the brute force DDAs at this resolution performed better than the TRAD DDA, with the 90s_VORT_BF and 150s_VORT_BF having a higher CRMSE than the TRAD and NOVORT DDAs and the 30s_VORT_BF having a CRMSE that is slightly lower than the NOVORT DDA but similar to the TRAD. Even though the TRAD DDA and the 30s_VORT_BF have similar CRMSE, they are achieved in different manners, as the 30s_VORT_BF has a lower correlation coefficient, but has a standard deviation that is closer to the observation standard deviation. As in the 125-m resolution DDAs, using advection correction results in a substantial improvement in the skill of the 90-s and 150-s DDAs. The correlation coefficient is lower when advection correction is used for the vorticity tendency calculation, but the standard deviation of the vertical velocity is closer to the observed standard deviation. Again, this reduction in correlation coefficient is likely due to the downdraft present in these DDAs at 2136 UTC. The difference between two-dimensional advection correction and three-dimensional advection correction is more mixed at this resolution. The three-dimensional advection correction technique made the 90-s DDA slightly better, but made the 150-s DDA slightly worse. At 30 s, two-dimensional advection correction produced verification statistics similar to the 30s_VORT_BF, but three-dimensional correction resulted in a higher CRMSE. As at 125-m resolution, the 90s_VORT_3DADV had the lowest CRMSE for the 250-m resolution DDAs.

The qualitative verification showed that the vorticity constraint DDAs performed poorly when the verification point was close to a data void. At those times and locations, the vorticity equation constraint is not applied since the vorticity tendency cannot be calculated. Therefore, including these times and locations when calculating the objective verification statistics may not represent the true skill of the vorticity constraint. If only the times and locations where the vorticity constraint is applied are used for the objective verification, the CRMSE is lower than the times and locations that do not use the vorticity constraint are included (Figs. 4.13 and 4.14). At the 125-m resolution, the CRMSE at only the vorticity constraint locations for the TRAD and NOVORT actually increases. This suggests that the improvement in CRMSE seen in the vorticity constraint DDAs is due to the vorticity constraint and not due to the sample of verification points used for the calculations. The improvement in CRMSE is mostly due to an increase in the correlation coefficient. At the

250-m resolution, the increase in correlation coefficient is even more drastic than at 125-m. This jump in correlation coefficient was expected since the strong downdraft present at 2136 UTC is not included in the verification statistics when only locations with a vorticity constraint are included.

Overall, these results suggest the vorticity constraint DDAs provide more accurate vertical velocity retrievals when the proper method for calculating the vorticity tendency is used. However, vertical velocity retrievals near data voids will likely be less skillful as the vorticity constraint cannot not be applied at these points since an estimate of the vorticity tendency cannot be made.

The average RMSE with height over the entire DDA time period shows the typical error accumulation with height that is expected for DDAs (Fig 4.15). For the 125-m resolution DDA, the TRAD and NOVORT have a greater decrease in skill with increasing height than the vorticity constraint DDAs. However, this is not the case for the 250-m resolution DDAs. The 90s_VORT_BF and 150s_VORT_BF have higher RMSEs than the TRAD and NOVORT below 2.5 km, but equal or lower RMSE above 2.5 km for the 125-m resolution versions. At 250-m resolution, these DDAs have higher or approximately equal average RMSE for all heights. At 125-m resolution, the 30s_VORT_BF and all of the advection correction DDAs have lower or similar RMSE than TRAD and NOVORT throughout the entire vertical profile. The 30-s DDAs have a reduction in skill at 2–2.5 km that prevents them from having a lower total RMSE than the 90-s DDAs that use advection correction to calculate the vorticity tendency. The lower resolution vorticity constraint DDAs are not significantly better than the NOVORT and TRAD DDAs. This is mostly due to the improvement in the NOVORT and TRAD DDAs and not the vertical vorticity DDAs performing more poorly at a lower resolution. The improvements that do occur in the vorticity constraint DDAs are most noticeable below 3 km. Specifically, the 90s_VORT_2DADV, 90s_VORT_3DADV, 150s_VORT_2DADV, and 150s_VORT_3DADV have the most improvement at these levels. The 30-s DDAs do not have the same improvements and instead have similar RMSEs to the TRAD and NOVORT.

4.4.3 Domain-Wide KTLX Verification

The SMART-R3 observations were the only observations of vertical velocity that could be used to verify the DDA vertical velocities, but the KTLX radial velocities can be used to assess the DDA skill across the entire DDA domain. Since KTLX scans with low elevation angles, this verification will mostly represent the DDA's skill in retrieving the horizontal wind components. This verification is still useful for quantifying differences in the horizontal wind retrievals between DDAs. For this verification, the KTLX radial velocities were gridded at the same horizontal resolution as the DDAs, but on conical surfaces for each sweep using a Cressman filter with a 1-km Cressman radius. Each sweep was gridded separately instead of as an entire volume due to the longer scan times of KTLX as 10 DDAs were conducted in the time it took to complete one volume scan. For each KTLX sweep, the radial velocities that would be observed by KTLX from the DDA time closest to the KTLX sweep time were calculated. The RMSE between the KTLX-observed radial velocities and the calculated radial velocities from the DDA retrievals was determined for the entire DDA time period and for each DDA experiment.

For both the 125-m and 250-m resolutions, there were minimal differences in the radial velocity RMSE between DDA experiments (Table 4.2). This is an expected result and is consistent with the OSSE results in Potvin et al. (2012b), as the horizontal wind field is not strongly affected by including a vorticity constraint since the horizontal winds are already well constrained by the observations.

4.4.4 Domain-Wide Analysis of Retrieved Vertical Velocity

Even though there is no verification source for vertical velocity across the domain, it is still useful to compare the vertical velocity field between the different DDA experiments. One feature that was very apparent when comparing the vertical velocity fields between experiments was that the vorticity constraint DDAs had more spatial variability in the vertical velocity than the TRAD and NOVORT experiments (Figs. 4.16 and 4.17). This can be explained by the tilting term in the vorticity equation. In this term, the horizontal gradients of vertical velocity are present, and therefore, creating gradients in the vertical velocity is one way to balance the vorticity tendency. Another feature that stood out was an excessively strong downdraft that was retrieved in the TRAD and NOVORT DDAs around 2130 UTC in the southwest region of the storm. This downdraft reaches -48.84 m s^{-1} in the NOVORT and -51.44 m s^{-1} in the TRAD DDA at 125-m resolution. The downdraft is weaker in the 250-m resolution DDAs with the maximum downdraft reaching -31.05 m s^{-1} in the NOVORT and -26.20 m s^{-1} in the TRAD DDA. These values are unrealistic for the environment that these storms developed in and are likely a result of an observational error in the radar data. After revisiting the data, it was found that the RaXPol data likely had sidelobe contamination in this region that artificially enhanced low-level divergence, resulting in the strong downdraft. This data error, however, was serendipitous in that it revealed another advantage of the vorticity constraint. The vorticity constraint DDAs did not produce the excessive downdraft seen in the TRAD and NOVORT DDAs. This suggests that the vorticity constraint may help to reduce vertical velocity retrieval error when observational errors are present. As this study shows, even with extensive quality control of the radar data, radar data errors can still remain in a dataset. Using a vorticity constraint DDA would help to protect against analysis errors that result from observation errors. This is a potential feature of using a vorticity constraint that would be difficult to discover in an OSSE framework. Since there is no verification data for this region of the storm it is impossible to know the accuracy of the vorticity constraint DDAs in this region, but it is clearly an improvement upon the unrealistic downdraft present in the TRAD and NOVORT DDA.

4.4.5 Comparing Vorticity Tendency Calculations

The accuracy of the vorticity tendency calculation is critical for accurate vertical velocity retrievals with the vorticity constraint DDAs, so an analysis of the vorticity tendency calculated using the different techniques can provide insights into why there were significant skill differences in the vertical velocity retrievals depending on the time between volume scans and the method for calculating the vorticity tendency. The average magnitude of the vorticity tendency at the verification point was lower for the 250-m resolution DDAs than the 125-m resolution DDAs (Fig. 4.18). This difference is expected due to the resolution difference. The 90s_VORT_BF and 150s_VORT_BF at both resolutions have lower estimates of the vorticity tendency magnitude and the magnitudes of the vorticity tendency in these DDAs are more constant throughout the entire DDA period. The 30s_VORT_BF DDAs have magnitudes of the vorticity tendency similar to the advection correction DDAs, which suggests that 30-s volume scans are rapid enough to use the brute force technique for this data set. The 90s_VORT_BF and 150s_VORT_BF vorticity tendencies significantly deviate from the magnitude of the vorticity tendency from the other techniques between 2130 and 2133 UTC and after 2145 UTC. These two time periods are also the time periods where these DDAs produced inaccurate vertical velocities (Figs. 4.5 and 4.6). This result directly shows the importance of accurate vorticity tendency calculations when using the vorticity constraint, as the inaccurate vorticity tendency estimates in the 90s_VORT_BF and 150s_VORT_BF DDAs lead to errors in the vertical velocity retrievals that were worse than those in the TRAD and NOVORT DDAs.

Profiles of the vorticity tendency at 2134:40 UTC at the verification point show that the 90s_VORT_BF and 150s_VORT_BF have very little change in the vorticity tendency with height, while the other methods show much more vertical variation in the vorticity tendency (Fig. 4.19). These profiles also show that the largest spread in the vorticity tendency occurs above 3.5 km, and this spread is greater at 125-m resolution. The 125-m 150s_VORT_2DADV appears to underestimate the magnitude of the vorticity tendency above 3.5 km, and at this time this DDA produces an excessively strong updraft. For the 250-m 150s_VORT_2DADV, the vorticity tendency above 3.5 km is more similar to the other DDAs, and this version of the DDA did not have large errors in the vertical velocity at this time. Again, this shows the importance of the vorticity tendency calculation for these DDAs.

It is also encouraging to see that the advection correction methods for calculating the vorticity tendency can produce vorticity tendencies similar to the 30s_VORT_BF when the volume scan times are 90 s and 150 s. This indicates that these techniques may enable the vorticity constraint DDA to be applied to datasets with slower volume scans. Of course, this was not a complex storm, so these results may not hold for a storm with a stronger and more variable wind field.

4.4.6 Impact of DDA Technique on Trajectory Analysis

The objective verification showed that there was less than a 1 m s^{-1} difference in CRMSE between the best vorticity constraint DDA and the NOVORT DDA at the SMART-R3 verification point. That difference may not seem large, but it is important to determine if this difference would significantly impact analyses derived from the DDA-retrieved wind field. One such analysis that is conducted with DDA-retrieved wind fields is the calculation of trajectories, which can be used to analyze budgets of vorticity and other variables (e.g., Conway and Zrnić 1993; Marquis et al. 2008; Miller et al. 2020). Backward trajectories were calculated for a 10.5-minute period from 2128:10 to 2138:40 UTC at every grid point for the 90s_VORT_3DADV, 90s_VORT_2DADV, 150s_VORT_BF, and NOVORT DDAs. These DDAs were chosen because they cover a wide range of DDA skill levels. These backward trajectories were calculated using a fourth-order Runge–Kutta scheme with a 5-s timestep. The locations of the trajectories in the 90s_VORT_2DADV, 150s_VORT_BF, and NOVORT DDAs at every timestep were compared to the 90s_VORT_3DADV trajectory locations and differences were calculated. The average differences in location of these trajectories from the 90s_VORT_3DADV trajectory location at each timestep are shown in Fig. 4.20. The difference in locations between the 90s_VORT_3DADV and the 90s_VORT_2DADV is less than 150 m for all three coordinates at both resolutions. The 150s_VORT_BF and the NOVORT DDA trajectories, however, have larger differences from the 90s_VORT_3DADV trajectories. The average x difference almost reaches 300 m for a 10-minute back trajectory and peaks around 250 m in the y coordinate for 6-minute trajectories. The dropoff in average difference after 7 minutes is due to trajectories leaving the data-coverage area, so differences between the trajectories cannot be calculated. The largest difference in coordinate, unsurprisingly, occurs in the z coordinate where the maximum average differences reach 650 m for the 125-m NOVORT DDA and 675 m for the 250-m NOVORT DDA. These maximum difference occur for back trajectories of approximately 6 minutes. Like for the x and y coordinates, the differences after 6 minutes are artificially lower due to trajectories leaving the data coverage area. The maximum average z difference for the 150s_VORT_BF trajectories is less than the NOVORT trajectories.

Figure 4.20 shows average differences in the coordinates of the trajectories, so there are regions of the storm that have larger and smaller differences than these averages. These regional differences are shown in Figs. 4.21 and 4.22 for the z coordinate of the NOVORT DDA. For 5-minute trajectories, there are some locations that have 3 km differences in trajectory height for the 125-m NOVORT DDA and 2 km differences for the 250-m NOVORT DDA. These are significant differences that could lead to entirely different conclusions from the trajectory analysis depending on the DDA technique that is used. This result shows that the differences between the NOVORT DDA and the best vorticity DDA are significant from a storm-scale analysis perspective.

4.5 Summary

The verification of the vertical velocities at the SMART-R3 verification point suggests that a vertical vorticity equation constraint DDA can improve vertical velocity retrievals. This is generally consistent with the prior OSSE studies (Potvin et al. 2012b; Dahl et al. 2019), however, it should be noted that the improvements in the OSSE studies occurred in situations with substantial depths of missing low-level data. In this real-data test there was not a large data gap between the lowest level of data availability and the ground, which indicates that the vertical vorticity equation constraint can provide value even in the best data availability scenarios, likely due to the vorticity constraint DDA being more forgiving to observational errors. The results also show that the vorticity constraint DDA can be prone to large errors in areas close to data voids where no estimate of the vorticity tendency can be made. Therefore, caution should be applied when interpreting results close to data voids, and potentially these points should be excluded from the final analysis.

The time between volume scans had a significant impact on the vertical velocity retrievals when the brute force technique was used for calculating the vorticity tendency. For 30 s between volume scans, the brute force discretization of the tendency was able to provide more accurate vertical velocity retrievals than the NOVORT and TRAD DDAs, but for 90 s and 150 s between volume scans larger errors occurred when the brute force technique was used. These errors occurred because the vorticity tendency was underestimated. When an advection correction method was used to calculate the vorticity tendency for 90 s and 150 s between volume scans the vorticity tendency estimates were more similar to the 30-s brute force vorticity tendencies and the vertical velocity retrievals had substantial improvements. Generally, vertical velocities retrieved when three-dimensional advection correction was used to calculate the vorticity tendency were slightly better than those retrieved when two-dimensional advection correction was used for the vorticity tendency calculation, but this improvement was much less than the improvement of the two-dimensional advection correction over the brute force technique for 90 s and 150 s between volumes scans. The 30-s volume scan DDAs did not improve when using advection correction, potentially because there was not much possible improvement in the vorticity tendency estimate from the brute force estimates.

The vorticity constraint DDAs appeared to be less sensitive to radar data errors than DDAs that did not impose a vorticity equation constraint. Sidelobe contamination in the radar data set caused the TRAD and NOVORT DDAs to produce nonphysical downdrafts while the vorticity constraint DDAs did not. This new finding highlights why OSSE study results should always by followed be real-data tests, as this is a potential feature of the vorticity constraint DDA that would be difficult to identify in an OSSE.

The differences between the retrieved wind fields from the varying DDA techniques were significant from an analysis perspective. A trajectory analysis using the DDA-retrieved winds had a 600-m average difference in height of the 6-minute trajectories, but these difference were as large as 3 km in some regions of the storm. These large differences demonstrate that analyses that use DDA retrieved winds should be used cautiously.

Finally, even though the results of this study were positive for the vertical vorticity constraint DDA this is only the first study to test the procedure with real rapid-scan radar data. Future tests should be conducted with different storm types and environments to see if the results hold for other scenarios. This is particularly important for determining the volume scan time needed for accurate retrievals when using the vorticity constraint as different storms types may generate vorticity at varying time scales. The skill of the vorticity constraint DDA could also be dependent on the vertical wind shear present in the environment, as vertical wind shear magnitude will affect vertical vorticity generation due to tilting. Overall, the vorticity constraint DDA is a promising technique that is well suited for the proliferation of rapid-scan radars.

Table 4.1: Names and descriptions of the dual-Doppler experiments performed for this study.

Name	**Variational Technique?**	**Vorticity Constraint?**	**Vorticity Tendency Calculation**	**Time Between Volume Scans**
TRAD	No	No	N/A	N/A
NOVORT	Yes	No	N/A	N/A
30s_VORT_BF	Yes	Yes	Brute Force	30 s
90s_VORT_BF	Yes	Yes	Brute Force	90 s
150s_VORT_BF	Yes	Yes	Brute Force	150 s
30s_VORT_2dADV	Yes	Yes	2D ADV Correction	30 s
90s_VORT_2dADV	Yes	Yes	2D ADV Correction	90 s
150s_VORT_2dADV	Yes	Yes	2D ADV Correction	150 s
30s_VORT_3dADV	Yes	Yes	3D ADV Correction	30 s
90s_VORT_3dADV	Yes	Yes	3D ADV Correction	90 s
150s_VORT_3dADV	Yes	Yes	3D ADV Correction	150 s

Table 4.2: Radial velocity RMSE (m s^{-1}) from the KTLX observations for all DDA experiments.

Experiment	**125 m**	**250 m**
TRAD	2.172	1.960
NOVORT	2.163	2.030
30s_VORT_BF	2.107	2.012
90s_VORT_BF	2.085	1.990
150s_VORT_BF	2.091	2.002
30s_VORT_2dADV	2.136	2.027
90s_VORT_2dADV	2.126	2.023
150s_VORT_2dADV	2.119	2.024
30s_VORT_3dADV	2.135	2.026
90s_VORT_3dADV	2.123	2.020
150s_VORT_3dADV	2.124	2.023

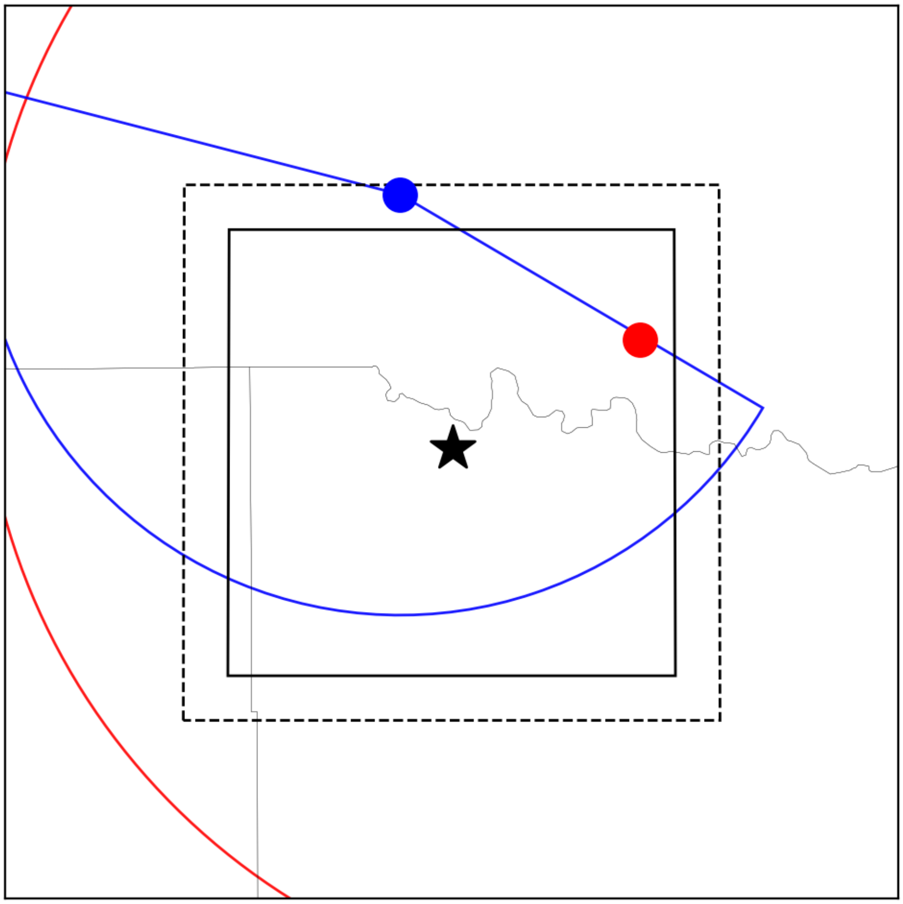

Figure 4.1: Provisional DDA domain (dashed border) and final analysis DDA domain (solid border). The location and scanning area of the AIR is shown in blue and the location and scanning area of RaXPol is in red. The black star is the location of SMART-R3.

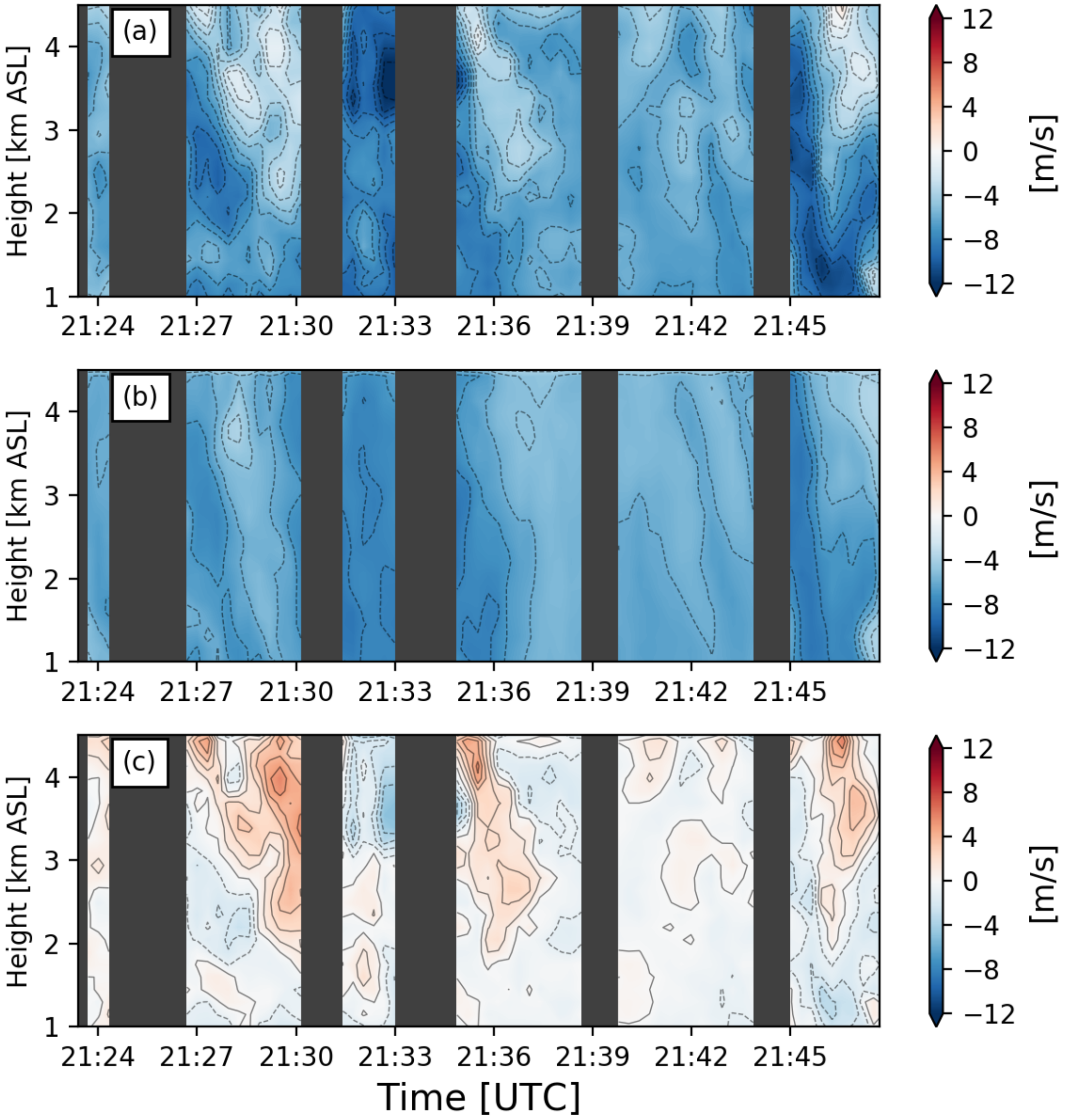

Figure 4.2: SMART-R3 (a) dealiased radial velocities, (b) terminal fall velocity calculated from (4.17) using the bias corrected SMART-R3 reflectivity, and (c) resulting observed vertical velocities after the terminal fall velocity was removed from the radial velocities. The contour interval is 1 m s^{-1} with negative values shown with dashed contours.

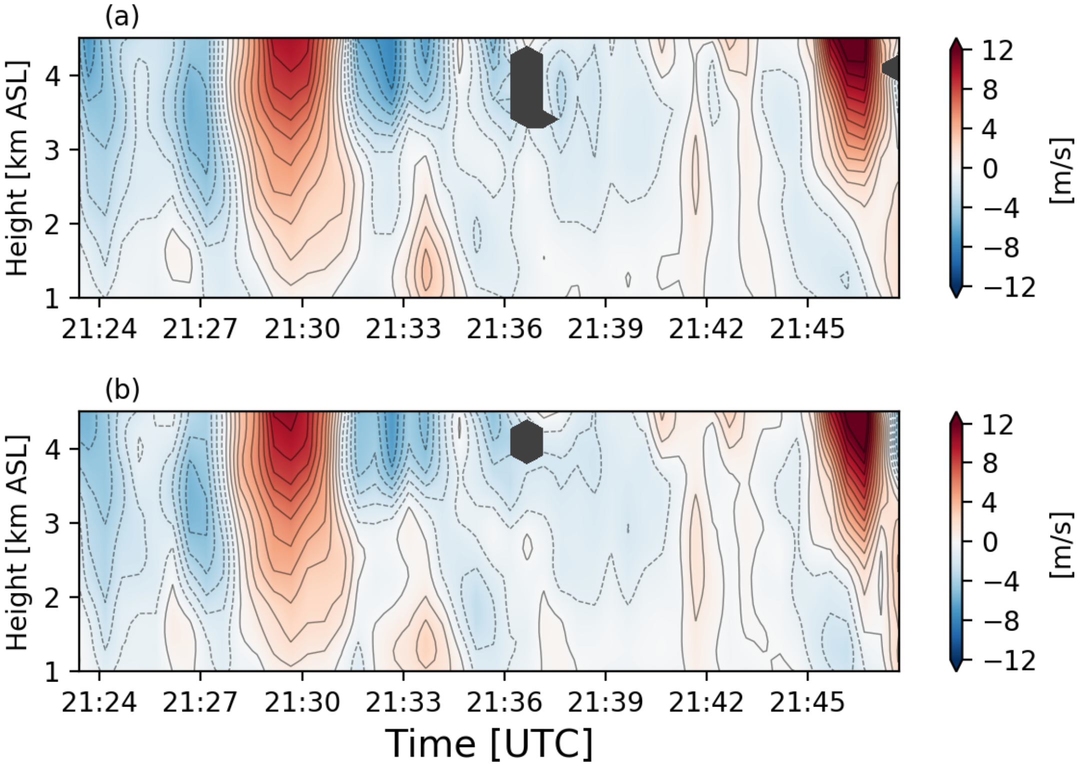

Figure 4.3: Vertical velocities retrieved by the 125-m (a) TRAD and (b) NOVORT DDAs at the SMART-R3 verification point for the entire DDA time period. The black contour interval is 1 m s^{-1} with negative values shown with dashed contours. Areas shaded in gray are locations where no vertical velocity retrieval could be performed due to lack of data from one or both input radars.

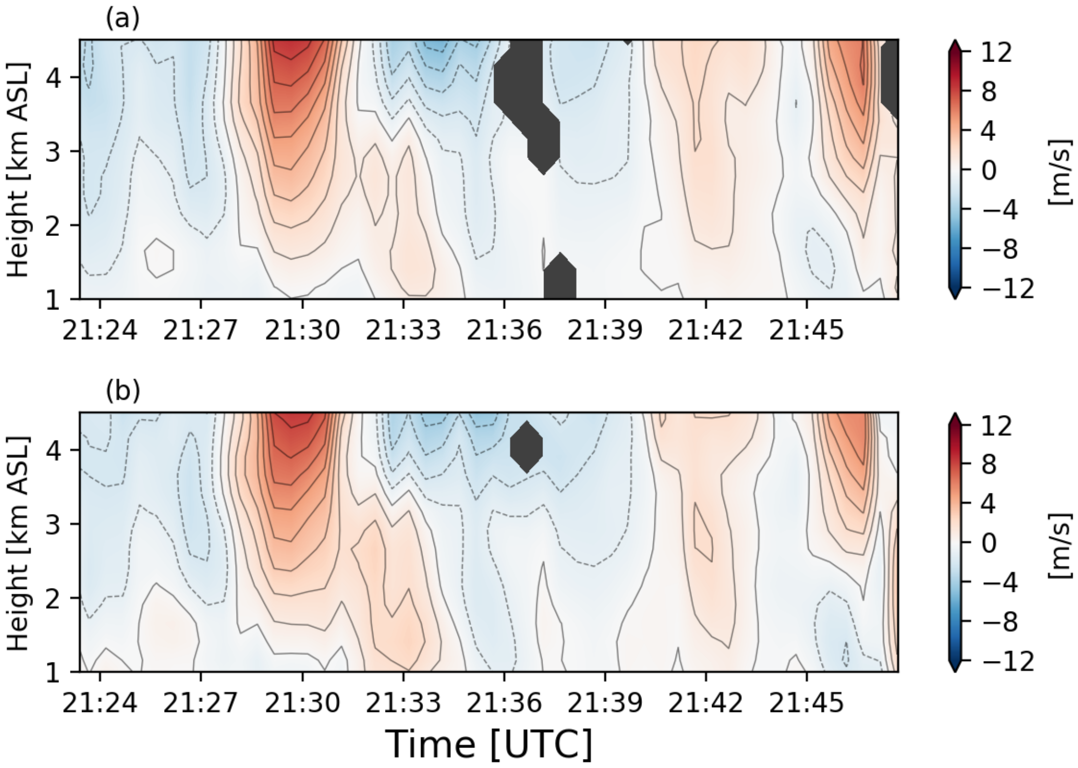

Figure 4.4: Same as Fig. 4.3, but for the 250-m (a) TRAD and (b) NOVORT DDAs.

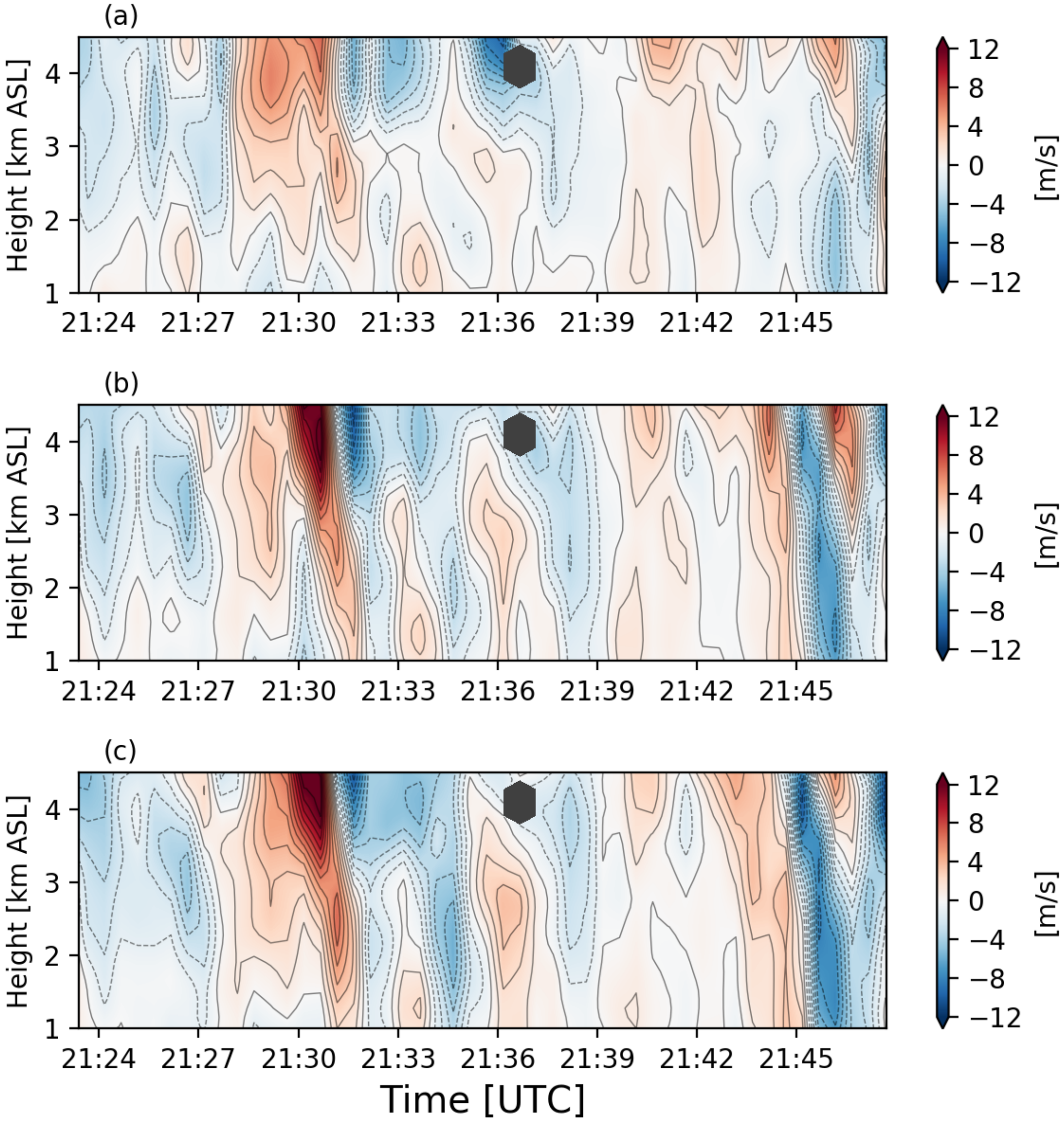

Figure 4.5: Same as Fig. 4.3, but for the 125-m (a) 30s_VORT_BF, (b) 90s_VORT_BF, and 150s_VORT_BF.

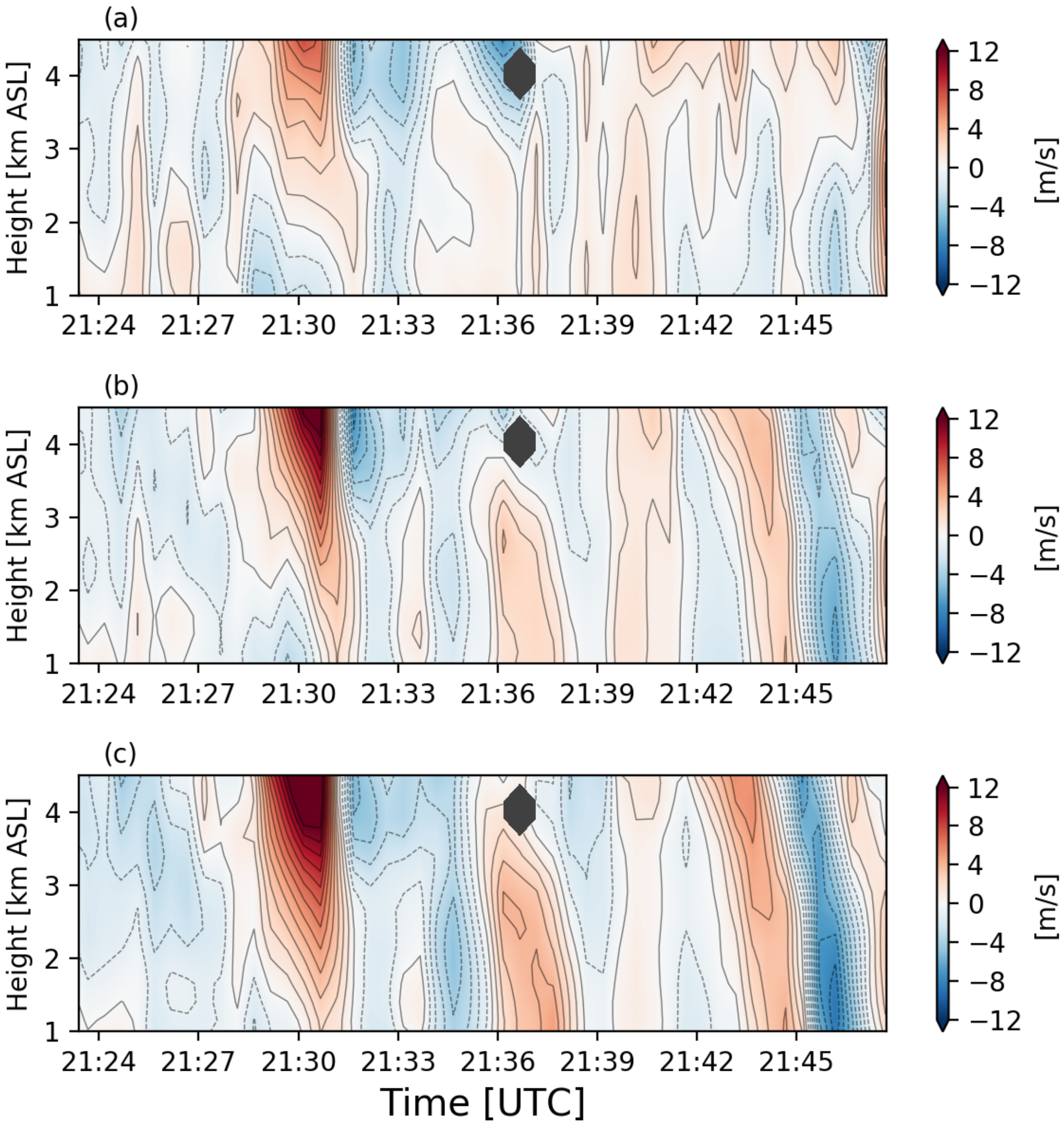

Figure 4.6: Same as Fig. 4.3, but for the 250-m (a) 30s_VORT_BF, (b) 90s_VORT_BF, and 150s_VORT_BF.

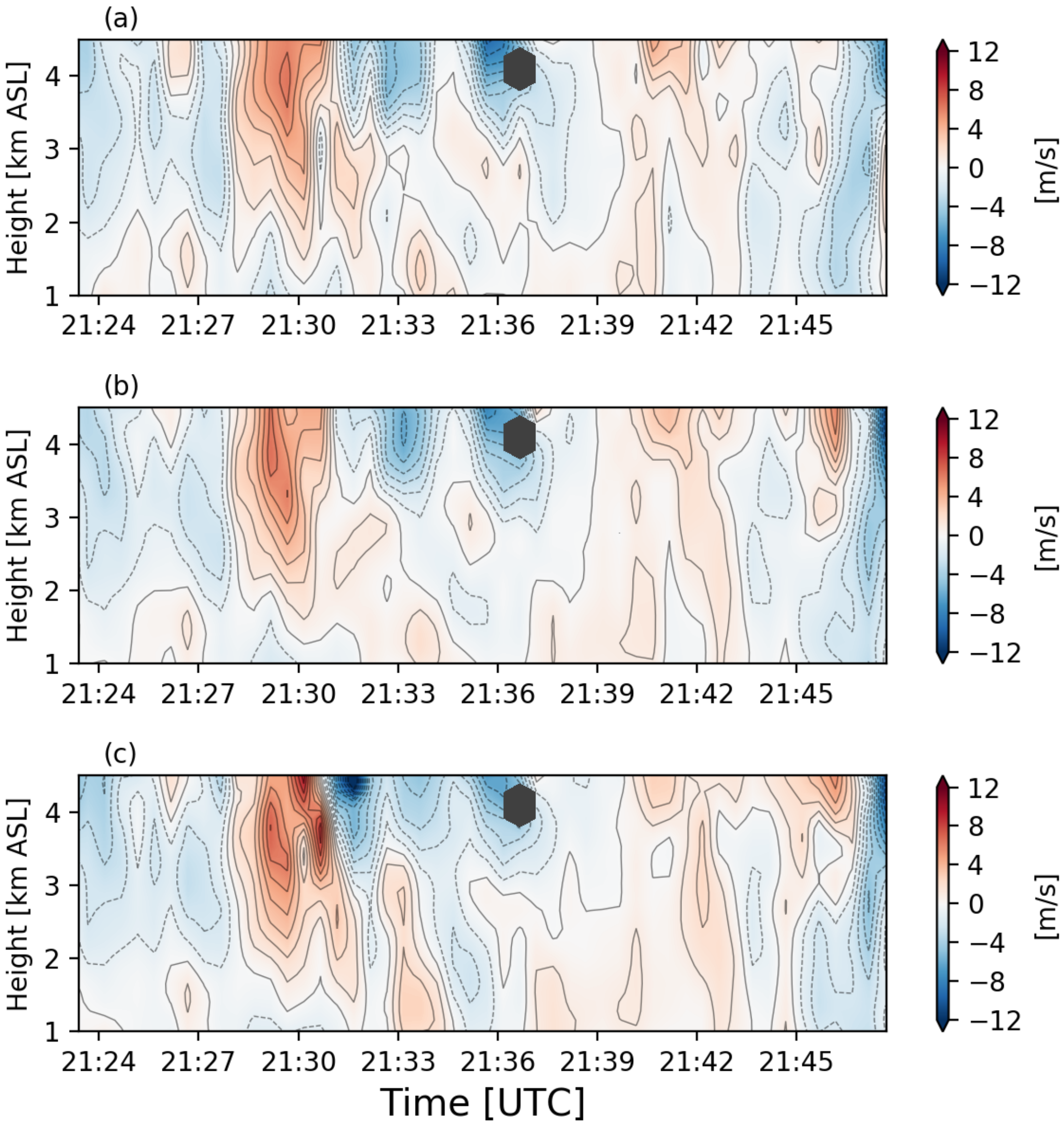

Figure 4.7: Same as Fig. 4.3, but for the 125-m (a) 30s_VORT_2DADV, (b) 90s_VORT_2DADV, and 150s_VORT_2DADV.

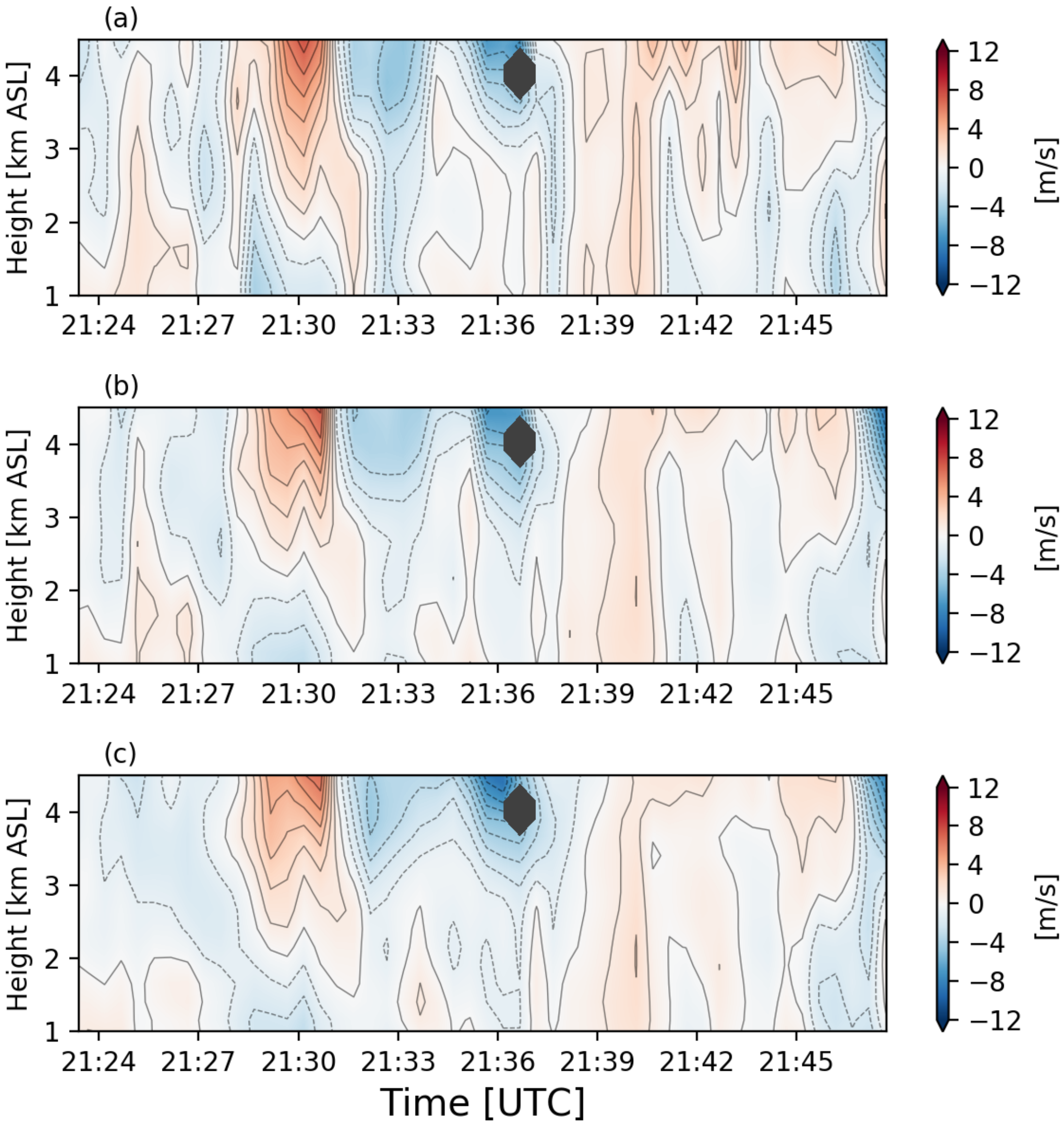

Figure 4.8: Same as Fig. 4.3, but for the 250-m (a) 30s_VORT_2DADV, (b) 90s_VORT_2DADV, and 150s_VORT_2DADV.

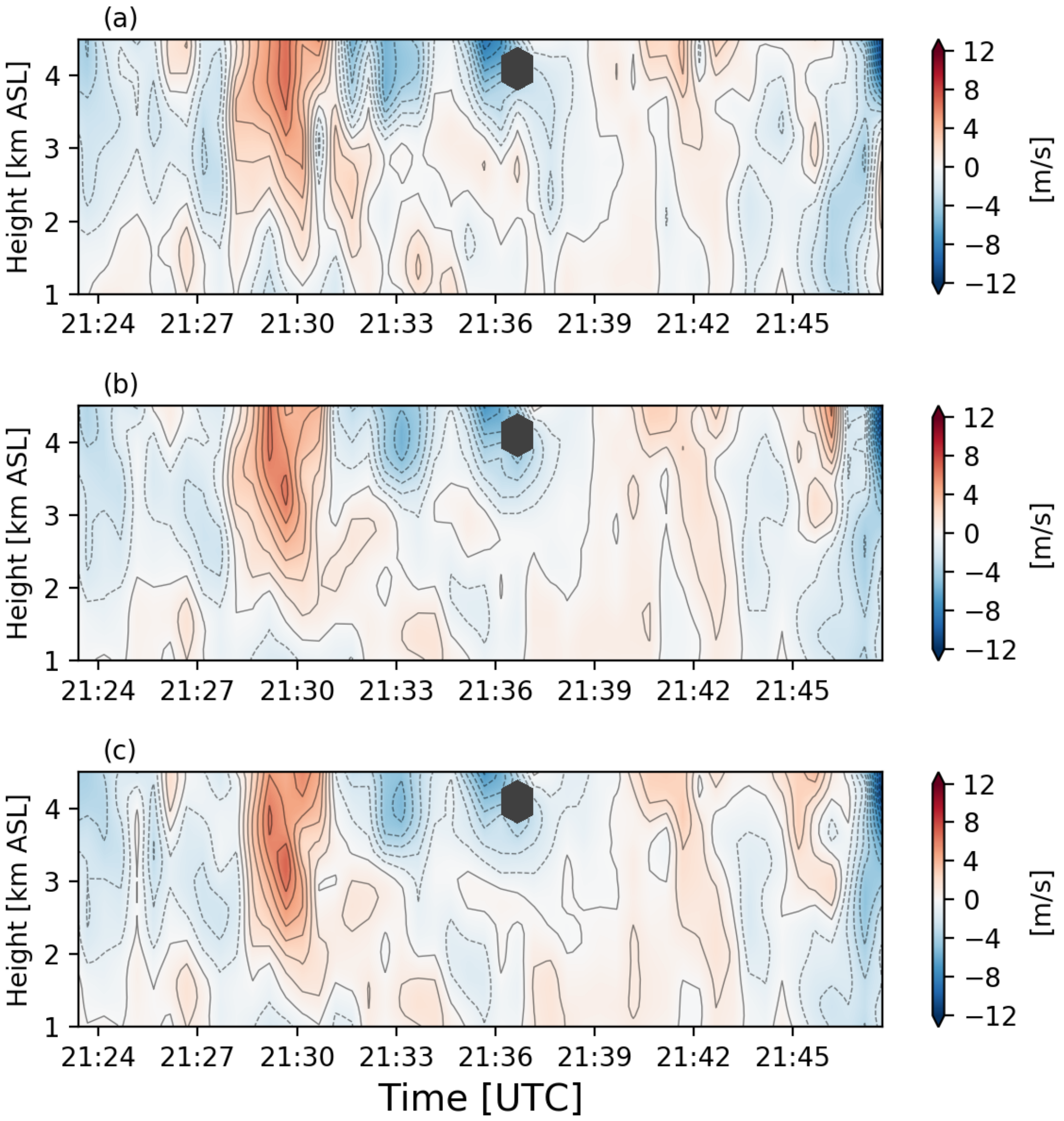

Figure 4.9: Same as Fig. 4.3, but for the 125-m (a) 30s_VORT_3DADV, (b) 90s_VORT_3DADV, and 150s_VORT_3DADV.

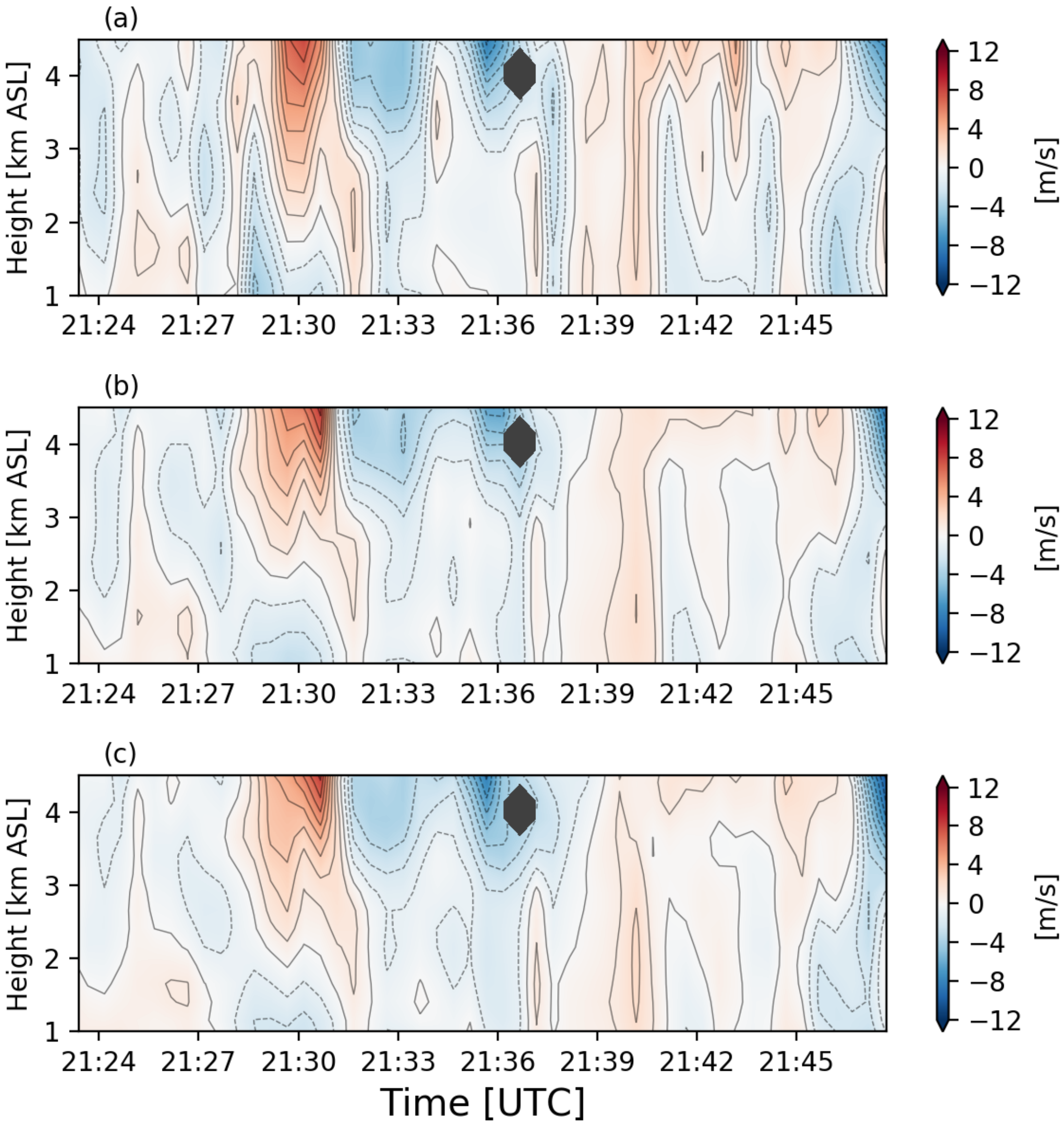

Figure 4.10: Same as Fig. 4.3, but for the 250-m (a) 30s_VORT_3DADV, (b) 90s_VORT_3DADV, and 150s_VORT_3DADV.

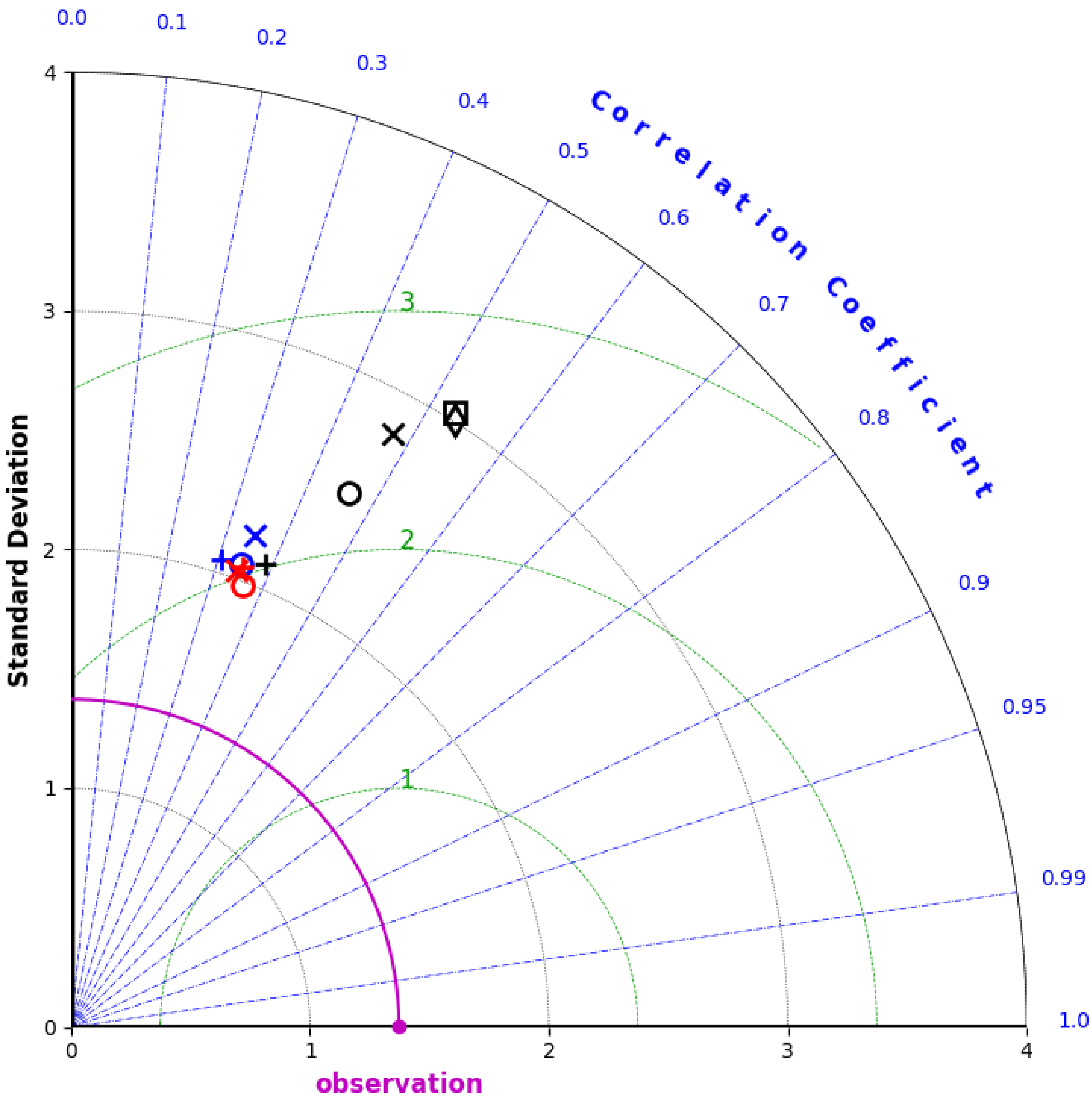

Figure 4.11: Taylor diagram for the 125-m DDA experiments. Correlation coefficient is the angular coordinate, standard deviation (m s^{-1}) is the range coordinate, and CRMSE (m s^{-1}) is represented by the green contours. The observation standard deviation is shown with the magenta arc. The markers for the TRAD and NOVORT DDAs are a black diamond and square, respectively. 30-s DDAs are represented by a cross, 90-s DDA by a circle, and 150-s DDAs by an ×. The technique for calculating the vorticity tendency is represented by color, with black markers for the brute force DDAs, blue markers for the 2-D advection correction DDAs, and red markers for the 3-D advection correction DDAs.

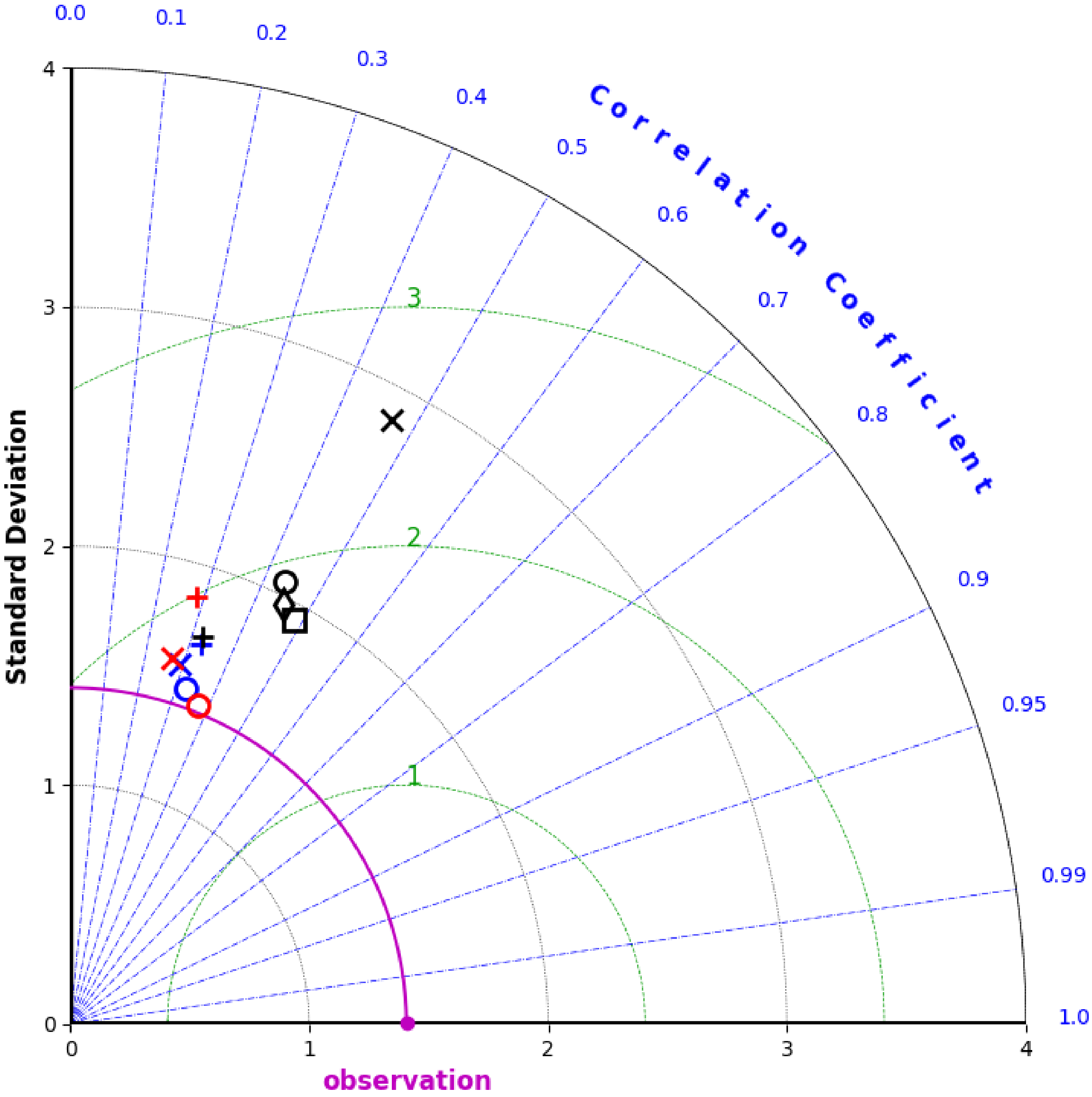

Figure 4.12: Same as Fig. 4.11, but for the 250-m DDAs.

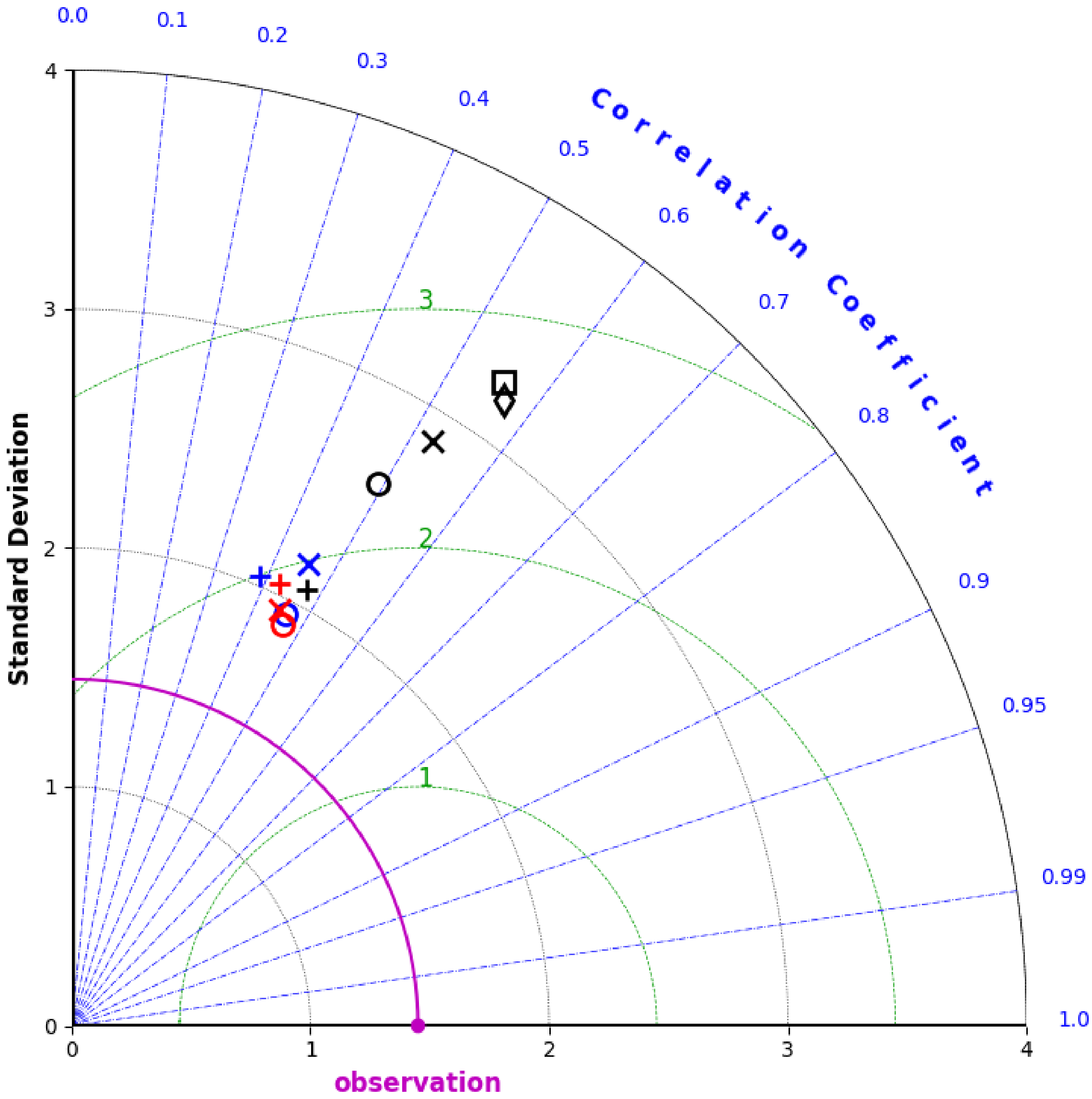

Figure 4.13: Same as Fig. 4.11, but only for the times and locations for the 125-m DDAs that have the vorticity constraint applied.

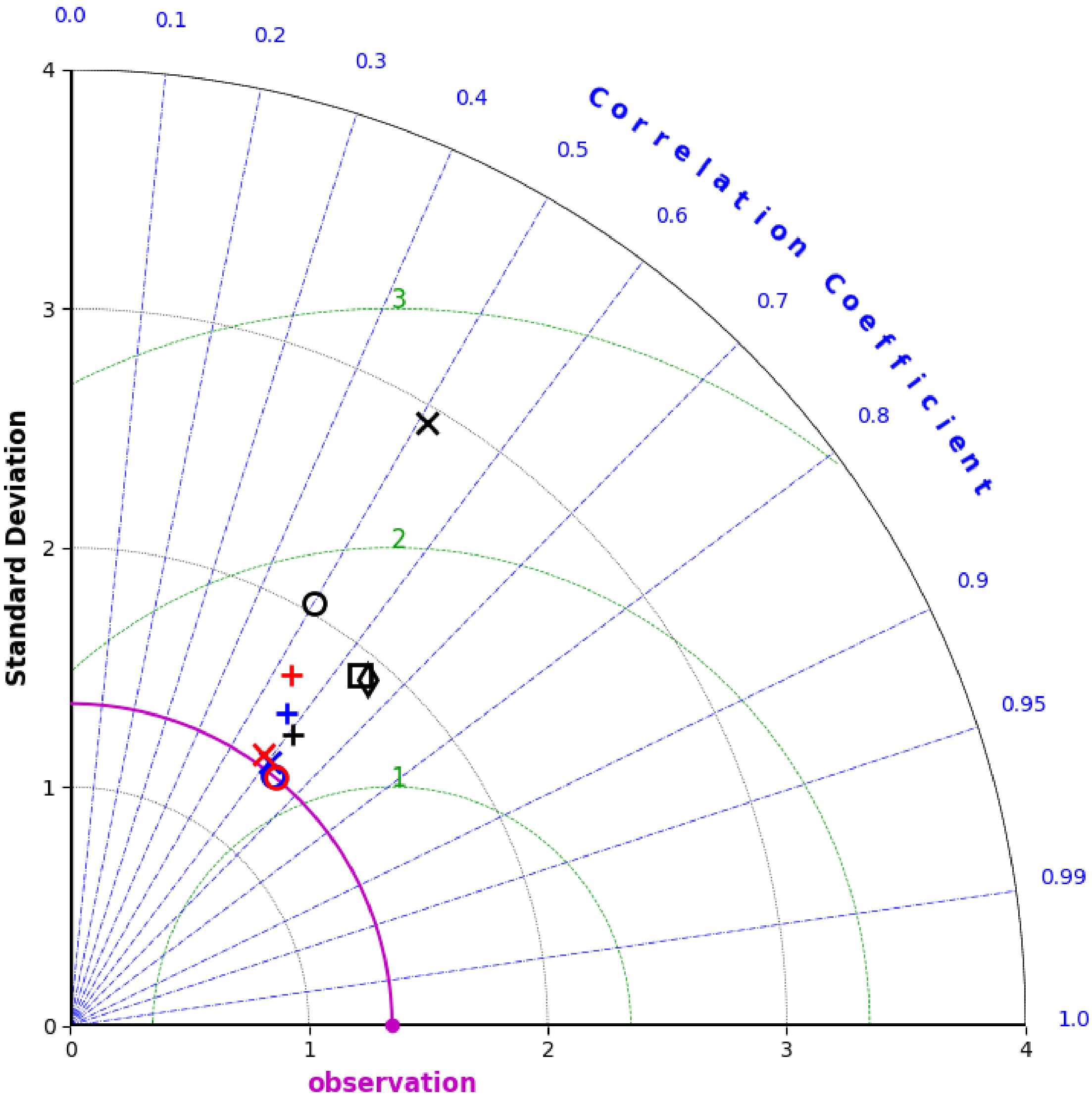

Figure 4.14: Same as Fig. 4.11, but only for the times and locations for the 250-m DDAs that have the vorticity constraint applied. Note that the marker for the 90s_VORT_2DADV DDA is covered by the marker for the 90s_VORT_3DADV DDA.

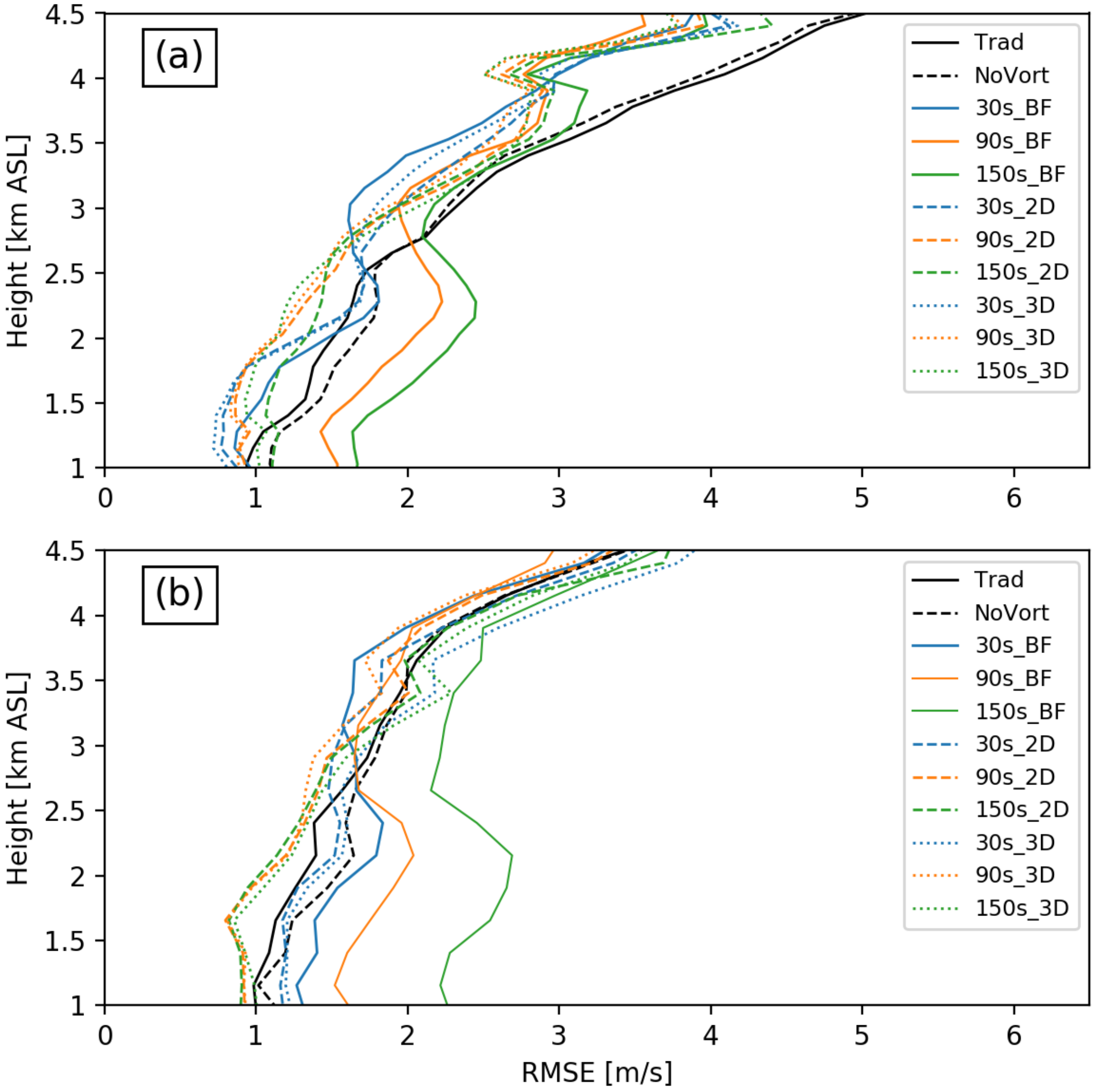

Figure 4.15: Profiles of average RMSE for the entire DDA time period for DDA experiments at (a) 125-m and (b) 250-m resolution.

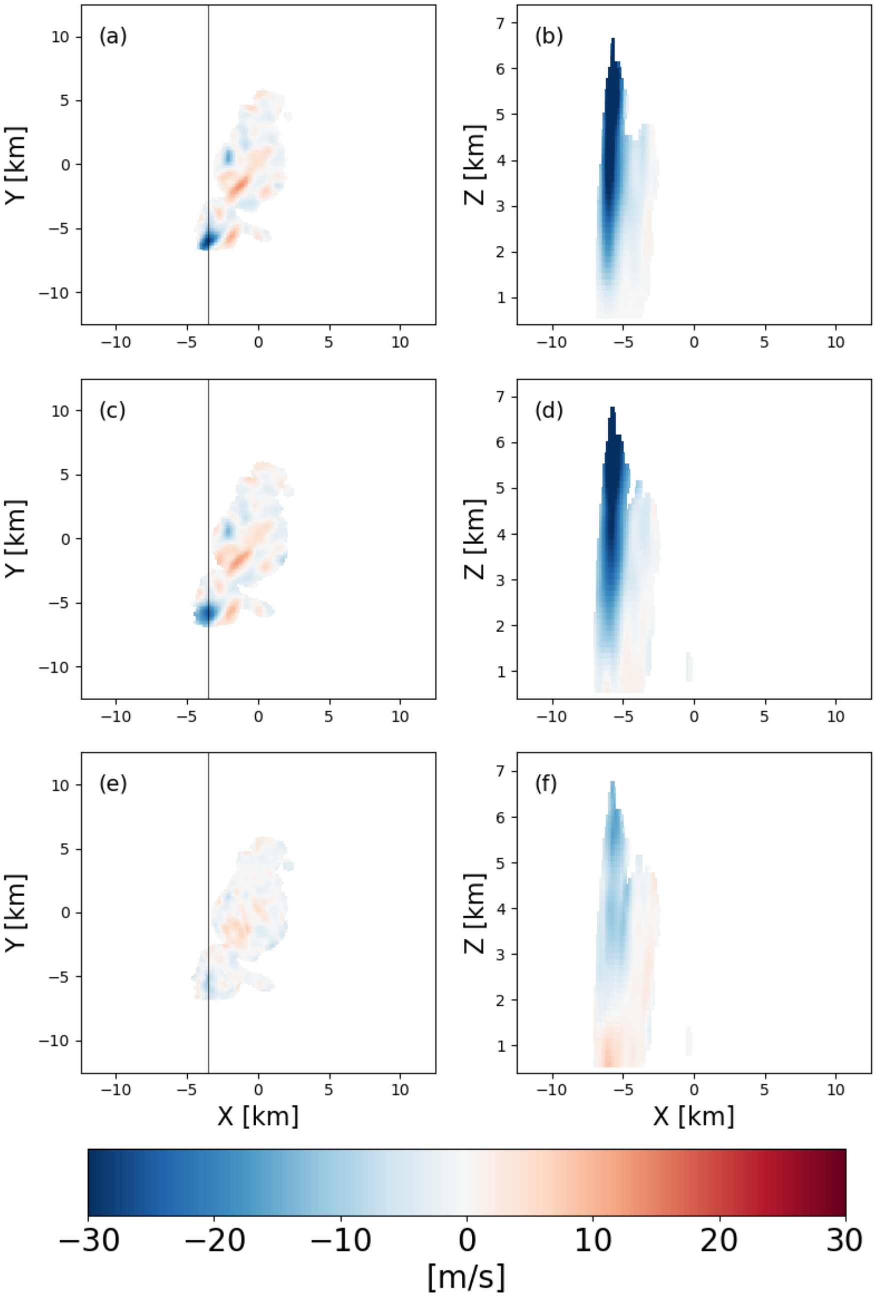

Figure 4.16: Retrieved vertical velocity from the 125-m resolution (a) TRAD, (c) NOVORT, (e) 90s_VORT_3DADV at 3.03 km ASL and horizontal cross-sections of retrieved vertical velocity at $x = -3.5$ km for the 125-m resolution (b) TRAD, (d), NOVORT, and (f) 90s_VORT_3DADV. The black line in (a),(c),(e) shows the location of the cross-section for (b),(d),(f).

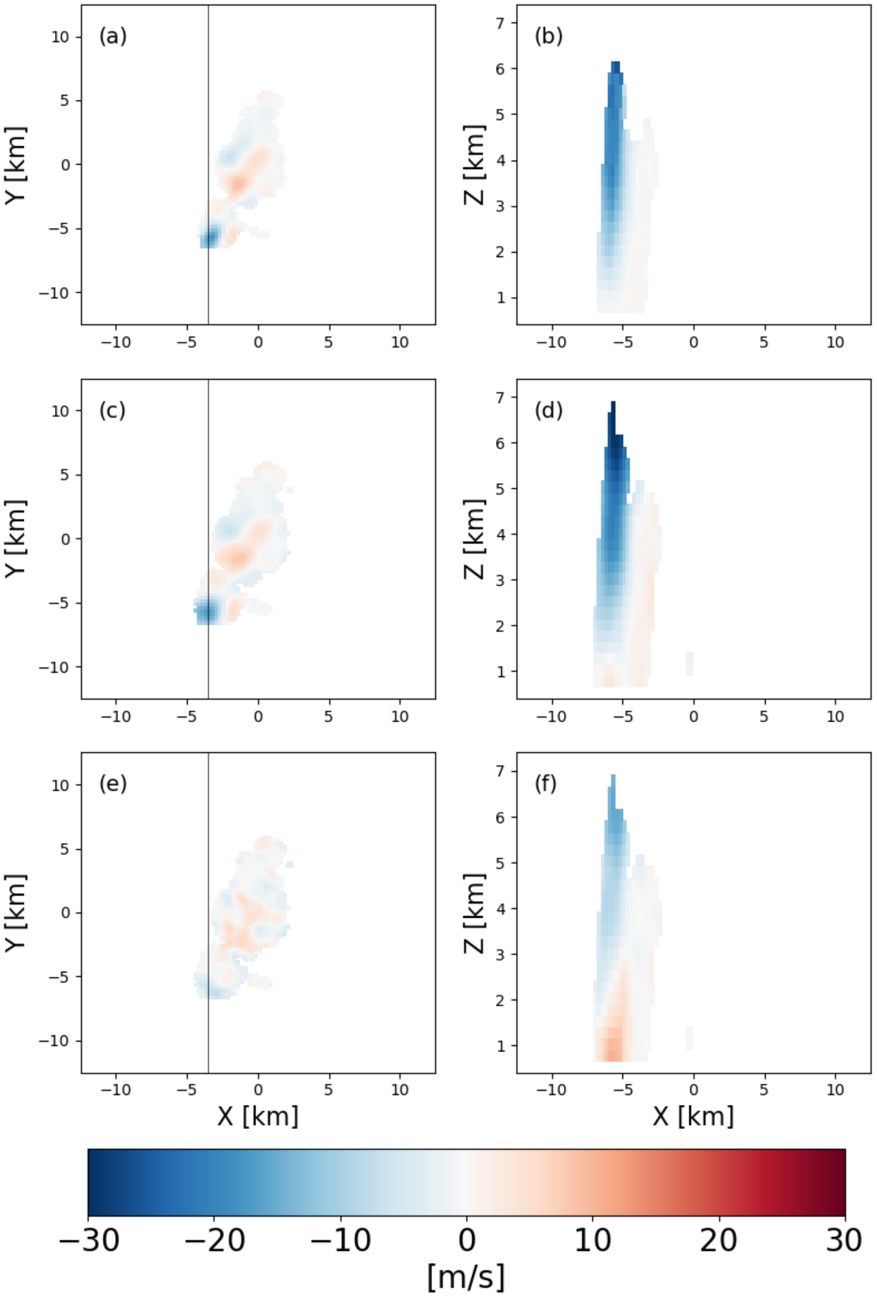

Figure 4.17: Same as Fig. 4.16, but or the 250-m resolution DDAs.

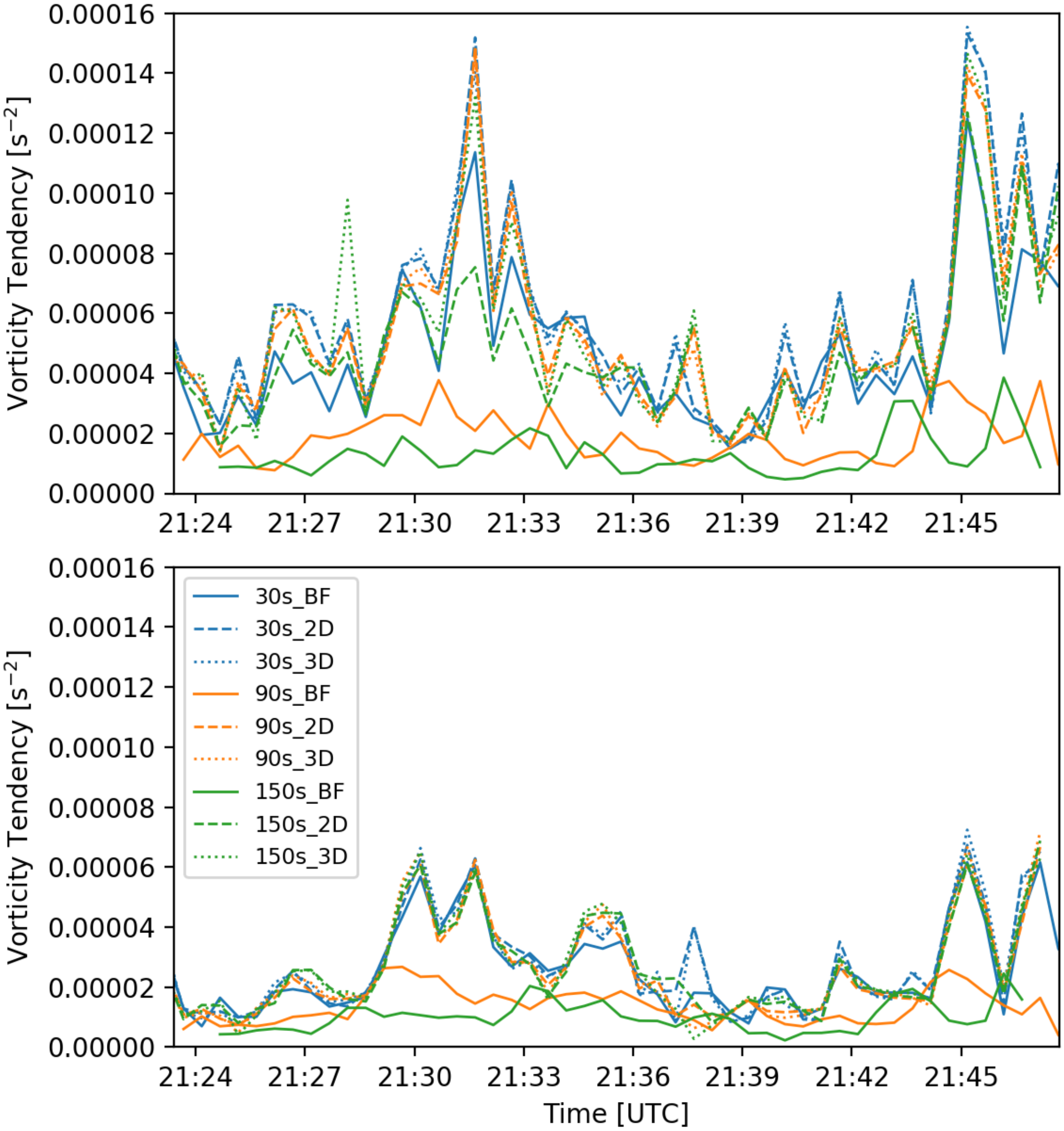

Figure 4.18: Average magnitude of the vorticity tendency at the SMART-R3 verification point for the (top) 125-m and (bottom) 250-m DDAs.

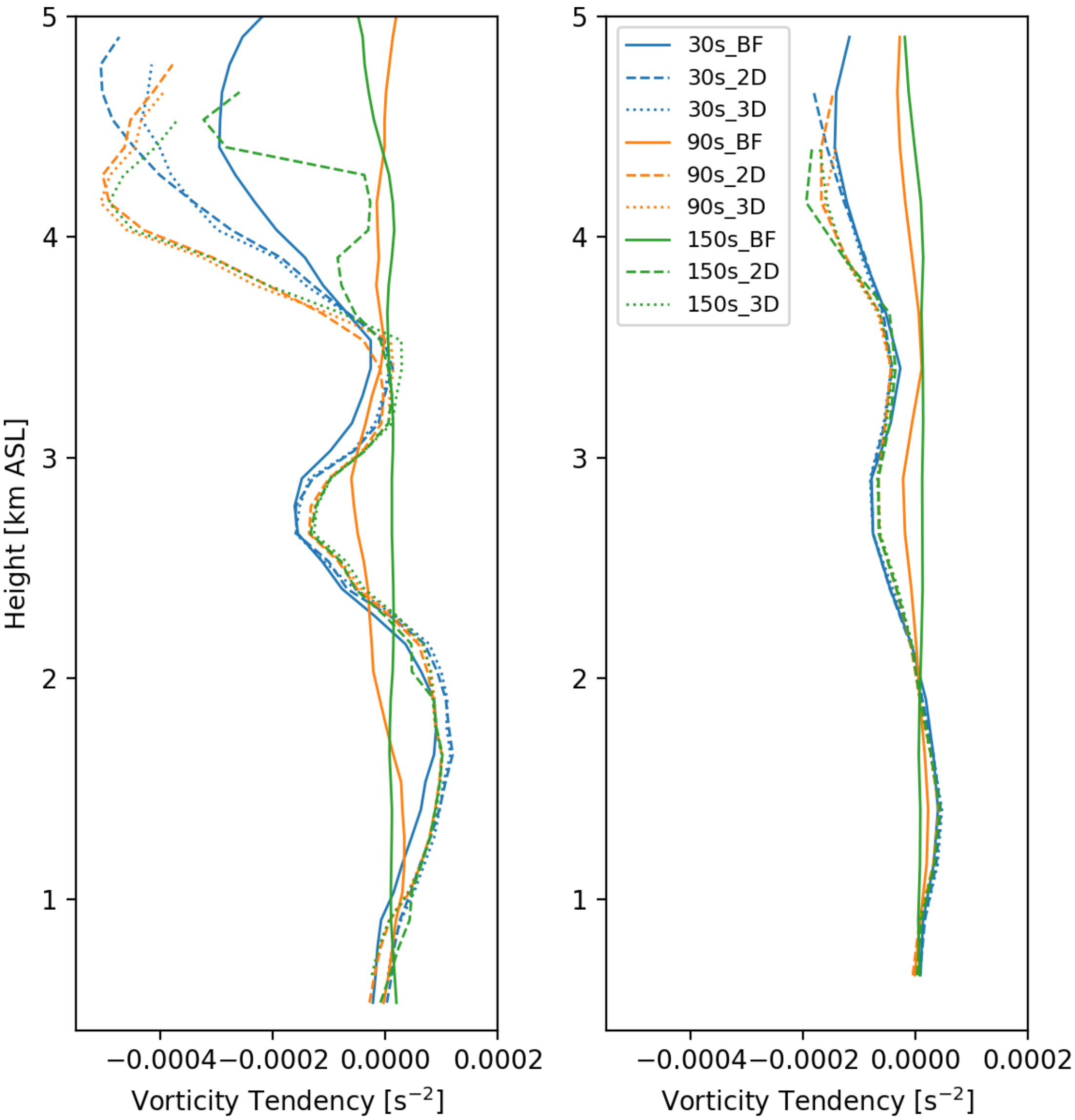

Figure 4.19: Profiles of the calculated vorticity tendency at the SMART-R3 verification point for 2131:40 UTC for the (left) 125-m and (right) 250-m resolution DDAs.

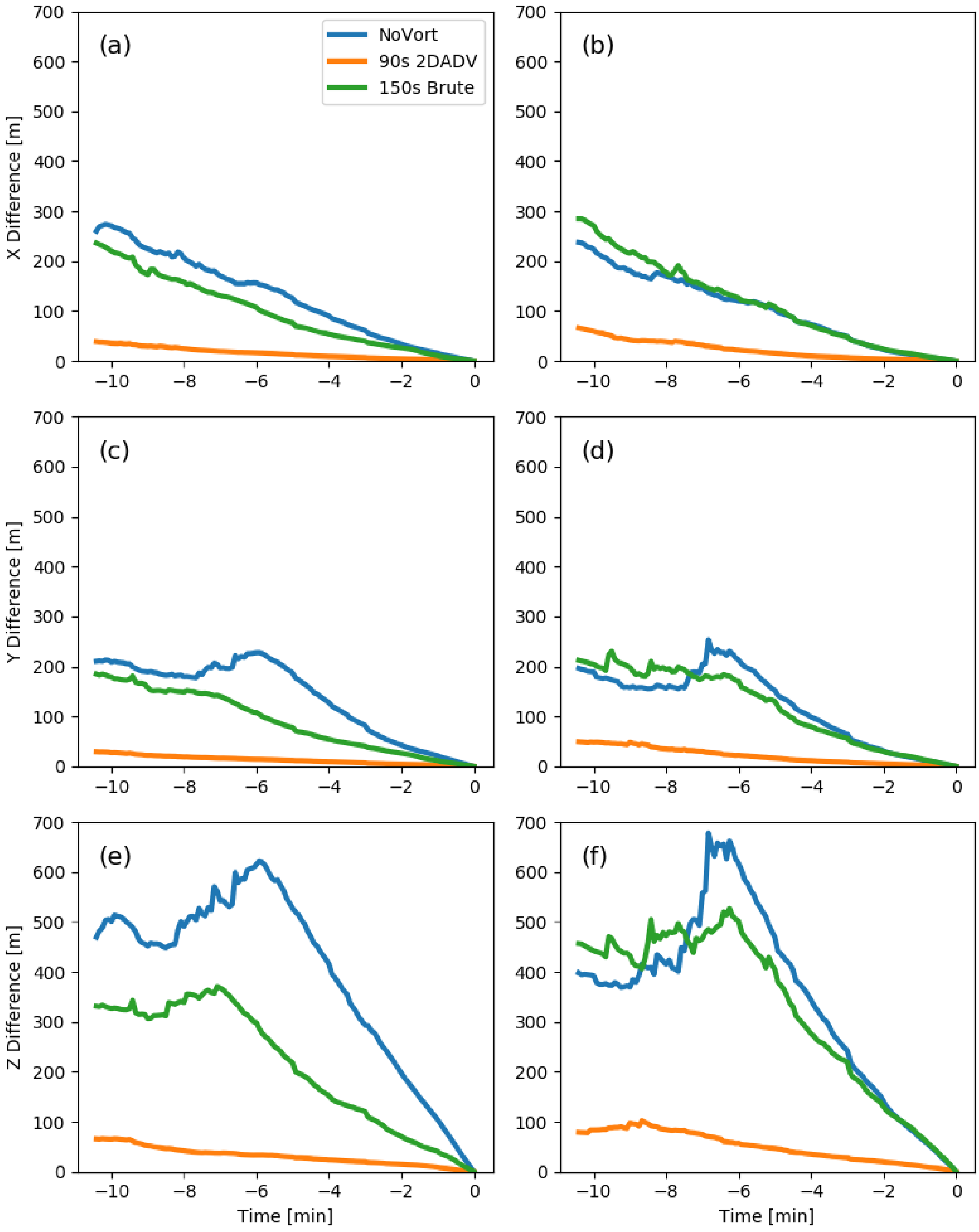

Figure 4.20: Average magnitude of the difference in (a),(b) *x*, (c),(d) *y*, and (e) (f) *z* coordinates of the trajectories from the trajectory coordinates for the 90s_VORT_3DADV DDA for (a),(d),(e) 125-m and (b),(d),(f) 250-m resolution DDAs.

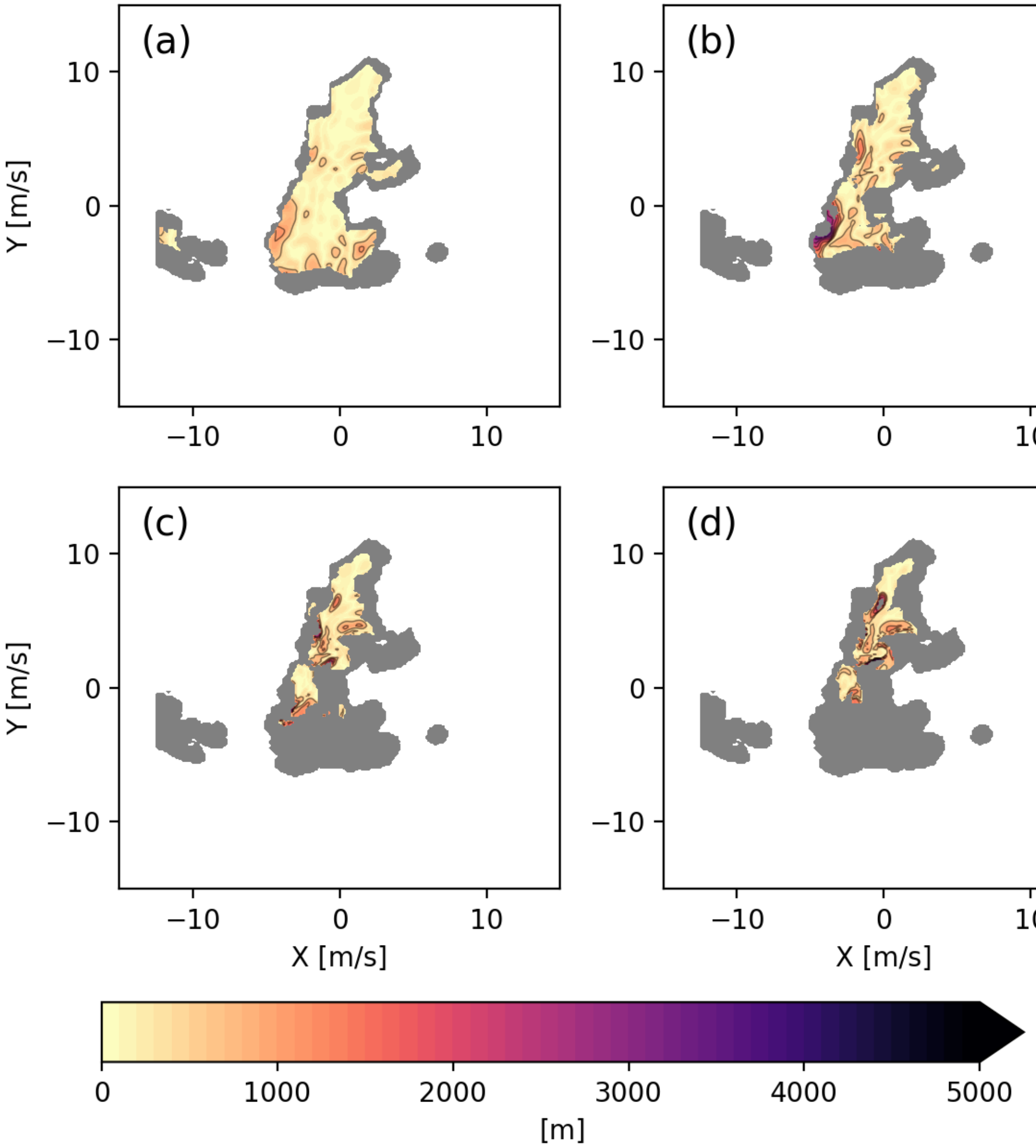

Figure 4.21: Magnitude of the difference in the z coordinate between the 125-m NOVORT and 90s_VORT_3DADV trajectories that began at $z = 2.905$ km ASL for (a) 2.5, (b) 5, (c) 7.5, and (d) 10 min trajectories. The solid contour interval is 0.5 km. The gray shaded region represents the area where differences could not be calculated due to the one of the trajectories leaving the data coverage area.

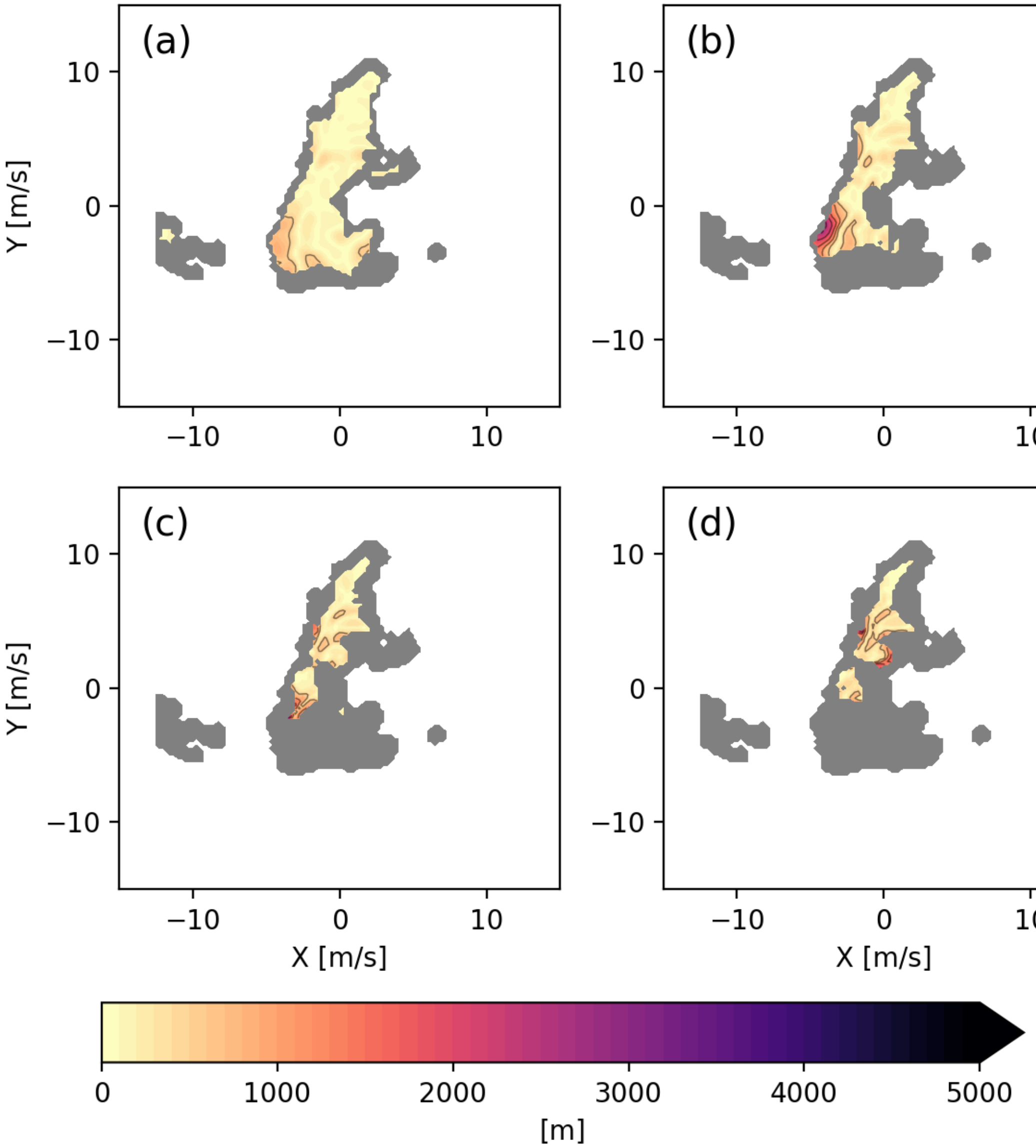

Figure 4.22: Same as Fig. 4.21, but for the 250-m resolution DDAs.

Chapter 5

Ensemble Kalman Filter Retrievals

5.1 Background

EnKF analyses have become more prevalent in recent years with the increase in computing resources. Unlike DDA analyses, EnKF analyses do not use geometric and physical constraints to obtain wind analyses. Instead, the radar data are assimilated into a background state to obtain the most likely atmospheric state using the background and the observation error covariances. The background state comes from an ensemble runs of an atmospheric numerical weather prediction model. EnKF analyses do not have the same issues that traditional DDAs have with boundary-condition specification and integration of the mass conservation equation using retrieved wind fields. However, EnKF analyses are computationally expensive as a large number of ensembles are needed to obtain accurate background error covariances. Often, the ensembles become underdispersed, which can result in the rejection of the observations and filter divergence.

Most research on EnKF data assimilation has not been focused on the accuracy of the wind analyses, but have instead focused on using EnKF data assimilation to improve forecasts from the analyses (Yussouf et al. 2013; Snook et al. 2015). Potvin and Wicker (2012) did compare EnKF analyses to variational DDAs with no vertical vorticity constraint, and found that the EnKF analyses were more accurate at mid- and upper levels, but EnKF analyses have never been compared to DDAs that use a vorticity constraint. Additionally, EnKF analyses are not typically performed at the resolutions of the DDAs conducted in Chapter 4. The author is also unaware of prior EnKF experiments that have assimilated volumes of radar data collected in 30 s or less. Research has been done for the Phased Array Radar (PAR) with 1-minute volume scans and have found that rapid-scan data improves forecasts initiated from the analyses, but the accuracy of the vertical velocity in the analyses themselves was not determined (Stratman et al. 2020). Rapid-scan radar data can be difficult to assimilate due to the short cycling frequency needed to prevent timing errors in the analyses. Short cycling frequencies are computationally expensive, and short integration times for the ensembles can create imbalances and noise that can reduce the accuracy of the analysis (Wang et al. 2013b; Lange and Craig 2014).

In this chapter, radial velocities from the 4 Sept 2018 dual-Doppler dataset is used to obtain EnKF analyses of the vertical velocity field to assess the performance of EnKF assimilation with high-resolution rapid-scan radar data. These results are also compared to DDA retrieved vertical velocities to determine if EnKF analyses with rapid-scan radar data are better than vorticity constraint DDAs at retrieving vertical velocity.

5.2 Data Assimilation and Ensemble Design

The ensemble used for these EnKF analyses is a 40-member ensemble of Version 3.8.1 of the Advanced Research Weather Research and Forecasting model (WRF-ARW; Skamarock et al. 2008). The ensembles use one-way nested domains with a 240 $\times$ 240 1.25-km spaced outer grid and a 141 $\times$ 141 250-m spaced inner grid with 51 stretched vertical levels centered on the original DDA area (Fig. 5.1). The ensembles have the same physics options for all members. The outer grid uses the Yonsei University (YSU) planetary boundary layer (PBL) scheme (Hong et al. 2006). Due to the fine resolution of the inner grid, no PBL scheme is used on the inner domain, but instead a large-eddy simulation (LES) set-up with a 1.5 order TKE closure is used. This is a coarse resolution for an LES set-up, but it is too fine of a resolution to use a PBL scheme and computational constraints prevented a higher resolution. The Monin–Obukhov similarity scheme is used for the surface layer physics, and the Rapid Update Cycle Land Surface model is used for the land surface physics. The longwave radiation physics is controlled by the Rapid Radiative Transfer Model (Mlawer et al. 1997), while the shortwave radiation physics is controlled by the Dudhia scheme

(Dudhia 1989). Lastly, the NSSL 2-moment scheme (Mansell et al. 2010) is used for the microphysics.

The initialization of the ensemble is arguably one of the most critical components of EnKF data assimilation. The spread of the ensemble is typically greatest at initialization and that spread needs to be maintained throughout the assimilation period. Therefore, a proper initialization is needed to help prevent the ensemble from becoming underdispersed. In this study, the initial ensemble perturbations are generated using a similar technique to the one described by Zhang et al. (2018) and Zhang et al. (2019). The 20-member Global Ensemble Forecast System (GEFS) analyses at 0000 UTC and 0600 UTC for 4 Sept 2018 are used to initialize 40 forecasts out to 2200 UTC on 4 Sept 2018. These forecasts are conducted using 1-way nested grids with 100×100 9-km spaced outer domain with 51 stretched vertical levels and a 100×100 3-km spaced inner domain that exactly matches the extent of the outer domain used for the EnKF experiments (Fig. 5.1). Starting for the 1200 UTC forecast and continuing through the 2200 UTC forecast, ensemble perturbations on the inner domain are calculated and then applied to the corresponding hourly High-Resolution Rapid Refresh analysis (HRRR; Benjamin et al. 2016; Blaylock et al. 2017). These perturbed HRRR analyses are then used as the initial and boundary conditions for the ensemble starting at 1200 UTC on 4 Sept 2018. The early start of the simulation is to allow for spin up and also generation of the proper storm environment before the actual analysis times for the vertical velocity verification.

The specific ensemble Kalman filter algorithm used for the data assimilation is the Ensemble Adjustment Kalman Filter (EAKF; Anderson 2001) from the Data Assimilation Research Testbed (DART; Anderson et al. 2009). DART was chosen for this study as it makes EnKF data assimilation accessible to the general research community, so the techniques used in this study can be easily replicated. Spatially and temporally varying adaptive state space inflation (Anderson 2009) is applied to the background ensemble before each assimilation cycle to help maintain spread in the ensemble due to the high density of the radar observations that are assimilated. Additive noise was applied to the *u*, *v*, temperature and dewpoint fields in regions with reflectivities greater than 35 dBZ in the simulations in the manner described by Dowell and Wicker (2009). A Gaspari–Cohn covariance localization (Gaspari and Cohn 1999) is applied for all observations. The horizontal localization radius is 0.0014137 radians ($\sim$9 km) for radar data, 0.0047123 radians ($\sim$30 km) for surface observations, and 0.036 radians ($\sim$230 km) for all other observations. The vertical localization is 3 km for radar observations and 4 km for all other observations. The settings used here are similar to those used in the Warn-on-Forecast System (Wheatley et al. 2015).

For the simulations starting at 1200 UTC, surface observations of temperature, dewpoint, and horizontal wind speed from the Oklahoma Mesonet (Brock et al. 1995; McPherson et al. 2007); conventional observations from the Global Data Assimilation System (GDAS); and radial velocities, reflectivity, and clear air reflectivity from the KTLX, KVNX, and KINX WSR-88D radars are assimilated every 15 minutes. The radial velocity and reflectivity data are superobbed to a 1×1 km grid on conical surfaces using a Cressman filter with a 3-km Cressman radius. Starting at 2100 UTC in the simulation, only the clear-air reflectivity and reflectivity observations from KTLX are assimilated along with the Oklahoma Mesonet data, and the RaXPol radial velocities every 2 minutes. The RaXPol radial velocities are superobbed to a 250×250 m grid on conical surfaces using a Cressman filter with a 400-m Cressman radius. The KTLX radial velocities are not used after 2100 UTC to avoid assimilating radial velocity data of differing temporal and spatial scales. The reflectivities from KTLX are still assimilated because the RaXPol reflectivity can not be used due to attenuation. The reflectivity data, and particularly the clear air reflectivity observations, helps to prevent convection in regions of the domain where it should not exist. The AIR data are added to the 2-minute cycling starting at 2122 UTC. These 2-minute assimilation cycles continue until 2148 UTC, which is the last analysis time for the experiments.

5.3 Experiments Performed and Verification Methods

The EnKF analyses from 2100 UTC to 2148 UTC were conducted three times with varying amounts of the RaXPol and AIR radial velocities being assimilated. In the first set of analyses, AIR and RaXPol radial velocities from volume scans every 30 s were assimilated every two minutes. In the other two experiments, RaXPol and AIR radial velocities from volume scans every 90 and 150 s are assimilated every two minutes. These experiments assess the impact of rapid-scan radar data on the EnKF wind analyses. The cycling frequency is held constant at 2 minutes to limit the "model shock" problem where too short of a cycling frequency introduces instabilities and noise into the analyses. Since the cycling frequency was held constant at 2 minutes, observations from RaXPol and AIR will have timing errors for the analyses, which is a common problem with synchronous EnKF analyses (Supinie et al. 2017). These timing errors can be avoided by using asynchronous EnKF, where observations are assimilated into the ensemble at the time they are collected (Sakov et al. 2010). Asynchronous EnKF is more computationally expensive, as the ensemble observations at all observation times need to be retained until the cycle is finished. DART currently does not have asynchronous EnKF abilities, and therefore, it is not used in this study, but this technique should be tested in future studies.

Before verifying the EnKF analysis vertical velocity, it is important to evaluate the performance of the data assimilation using observation-space diagnostic statistics. The first commonly used metric for this purpose is root-mean-square innovation (RMSI), which is defined as

$$\mathrm{RMSI} = \sqrt{\left\langle \left[y^o - \overline{H(\mathbf{x})} \right]^2 \right\rangle}, \tag{5.1}$$

where y^o is the observation, H is the forward operator, and $\mathbf{x}$ is the model state vector. Overbars represent the ensemble mean and $\langle\rangle$ represents the mean over all observations. RMSI represents the differences between the model and observations. RMSI should not reasonably be expected to equal zero because observations themselves have errors, but RMSI should be small and slightly decreasing throughout the assimilation. If RMSI begins to increase, it is often a sign of filter divergence. The second metric often used is total spread,

$$\text{total spread} = \sqrt{\sigma_o^2 + \left\langle \frac{1}{N-1} \sum_{n=1}^{N} \left[H(\mathbf{x}_n) - \overline{H(\mathbf{x})} \right]^2 \right\rangle}, \tag{5.2}$$

where σ_o is the observation error standard deviation, N is the number of ensemble members, and n is an index representing a particular ensemble member. The second term under the radical in (5.2) represents the average standard deviation of the ensemble for all observations. The observation error standard deviation is set to 5 dBZ for reflectivity observations, and 2 m s^{-1} for radial velocity observations. Ideally, the total spread starts at an appropriate value and does not greatly increase or decrease with time as those situations indicate that filter divergence may be occurring. The final metric used is consistency ratio,

$$\text{consistency ratio} = \frac{\sigma_o^2 + \left\langle \frac{1}{N-1} \sum_{n=1}^{N} \left[H(\mathbf{x}_n) - \overline{H(\mathbf{x})} \right]^2 \right\rangle}{\left\langle \left[y^o - \overline{H(\mathbf{x})} \right]^2 \right\rangle}. \tag{5.3}$$

When this ratio is $\sim$1, it suggests that the observation error standard deviation is appropriate for the ensemble spread and the total spread is representative of the forecast error. If the ratio is greater than 1, it suggests that the total spread is larger than optimal due to either the ensemble spread or the chosen observation error standard deviation. A ratio less than one indicates that the total spread is too small.

The verification of the EnKF analysis vertical velocities is conducted in a similar manner to the verification of the DDAs in Chapter 4. The SMART-R3 radial velocities with terminal fall speed removed are used as the verification data source for the analyses. The Taylor diagram statistics are again used as an objective verification tool. Specifically, the EnKF analyses are the probability-matched mean of the ensemble. The probability-matched mean uses the spatial patterns of the ensemble mean, but restores the amplitudes to those of the individual members. A probability-matched mean tends to be more skillful at convective scales than the basic ensemble mean (Clark 2017). There is not a reference EnKF experiment with which the analyses are compared, but instead the EnKF analyses are compared to 250-m 90s_VORT_3DADV DDA, which was the best 250-m DDA according to the Taylor diagram statistics in Chapter 4. Before calculating the Taylor diagram statistics, the EnKF analyses will be interpolated to the vertical levels used in the DDAs. Obviously, the temporal frequency of the analyses is different for the EnKF analyses and the DDA so any comparison of the objective verification metrics are done with analyses from common analysis times. This means that some verification statistics may be different than those presented in Chapter 4 for the DDAs, but this allows for a true comparison between the different analysis techniques.

5.4 Results

5.4.1 Catastrophic Filter Divergence

The observation space diagnostics highlight the difficulties with assimilating high-resolution rapid-scan radar data. For all experiments, the radial velocity RMSI increases throughout the cycling period, while the reflectivity RMSI is relatively constant (Figs. 5.2, 5.3, and 5.4). The increase in radial velocity RMSI is greatest in the 30-s volume scan experiment, and is lower in the 90- and 150-s experiments. The increase in RMSI coincides with an increase in the total spread, which together suggests that filter divergence is occurring in these experiments. The consistency ratios in all experiments are greater than 1 for both reflectivity and radial velocities for all experiments and cycling times. This indicates that either the ensemble spread or observation error standard deviation is too large. Considering that the total spread is very close to 2 m s^{-1} for the entire period it is more likely that the observation error standard deviation is too large and the observations are underfitted.

Looking further into the filter divergence issue, extremely large increments are found in regions outside of the high-observation-density areas (Fig. 5.5). The increments in the 30-s volume scan experiment are the greatest with increments in the vertical velocity exceeding 300 m s^{-1} late in the cycling period. The increments in the 90-s and 150-s volume scan experiments are lower than the 30-s volume scan experiment, but are still unreasonably large. The large increments indicate that the filter divergence in this case is different than classical filter divergence. In classical filter divergence, the ensemble spread becomes too small and observations are given little weight in the data assimilation. In the experiments in the present study, catastrophic filter divergence is occurring (Gottwald and Majda 2013; Kelly et al. 2015; Houtekamer and Zhang 2016). In this type of filter divergence, the ensemble spread becomes too large in unobserved regions, and therefore, huge increments occur. These huge increments result in nonphysical analyses and these analyses create instabilities in the model, which can cause the model to fail to complete the forecast step (hence the name catastrophic filter divergence). The model failed in the 30-s experiment after the 2146 UTC cycle, but the filter divergence did not cause the model to fail in the 90- and 150-s volume scan experiments. However, it is likely that with continued cycling these two experiments would eventually result in model failure.

Using the 30-s volume scan experiment as an example, one sees that the spread in the 30-s volume scan experiment becomes large in a data-sparse region of the domain, and since there are no radial velocity observations at these regions the ensemble spread is unchecked (Fig. 5.6). The large number of radial velocity observations causes large inflation values due to the technique's adaptive nature. However, these inflation values extend away from the observation region. This large inflation results in a region of large ensemble spread to the west of the main core of the radial velocity observations. There are no radial velocity observations in this area, so the background in this region is updated due to correlations within the data coverage area. With the increase in spread, the covariances with the data coverage area are amplified so even small innovations at the location of the observation can result in large increments in the high-spread, data-sparse region. Once the non-physical analyses begin, model instability and the continued adaptive inflation prevents the EnKF system from recovering. Observations that do appear in these regions in later analysis cycles are rejected as their values are too far from the ensemble mean and are deemed outliers. This further prevents correcting the downward spiral of the analyses.

The catastrophic filter divergence manifests itself earliest in the 30-s experiment because the covariance inflation is larger due to the higher number of observations being assimilated. With the larger inflation, the spread is amplified more quickly in the data-sparse regions, leading to a faster degradation of the analyses. Additionally, since the large-amplitude increments occur outside the data-coverage area, the region with dual-Doppler radar coverage is not initially impacted by the filter divergence. The observations are able to constrain the analyses in these regions even though nonphysical features develop around the data-coverage area. However, eventually the errors outside the data-coverage area propagate into the data-coverage area and degrade the analyses. This is represented by the slow growth in radial velocity RMSI in the experiments. The 90- and 150-s volume scan experiments only have an RMSI increase of about 0.5 m s^{-1} by the end of the cycling period despite the large increments occurring outside the data coverage area.

The type of filter divergence seen here would be difficult to prevent when high-resolution rapid-scan radar data are assimilated. The covariance inflation is necessary to prevent classical filter divergence due to the large number of observations, but it also facilitates the catastrophic filer divergence. One possible solution would be to increase the observation error standard deviation. With less certain observations, lower values of inflation would be needed, however, consistancy ratios in the experiments suggest that the observation error standard deviation should actually be lower, so artificially inflating the observation error standard deviation would result in significant underfitting of the observations. Another way to prevent the catastrophic filter divergence would be thinning the radial velocity observations. Thinning the observations would also reduce the inflation needed, but also would remove most of the additional data gained by using a high-resolution rapid scan radar. Therefore, rapid-scanning radar data may not be best suited to EnKF analyses. Despite the catastrophic filter divergence, the verification results are still presented, though it should be noted when interpreting the results that the data assimilation is sub-optimal for all experiments.

Motivated by the catastrophic filter divergence in the original experiments, one additional experiment was conducted with observations superobbed to 1-km spacing and the observation error standard deviation set to 3 m s^{-1}. All volume scans in the dataset are used in this experiment. The radial velocity RMSI drops (Fig. 5.7) and analysis increments remain reasonable throughout the cycling period (Fig. 5.5), so the experiment is able to avoid catastrophic filter divergence. However, the consistency ratios are much greater than 1, so the observations are significantly underfitted due to the high observation standard deviation. This trade-off was necessary to completely prevent the catastrophic filter divergence.

5.4.2 Verification

Since the EnKF analyses are only conducted every two minutes, there are fewer vertical profiles from the SMART-R3 that can be used for verification. The SMART-R3 vertical velocities at the EnKF analysis times are shown in Fig. 5.8a. There are fewer times of significant vertical motions in this dataset than the one used to verify the DDA retrieved vertical velocities, so the EnKF analyses should appear to have weaker overall vertical motions than the full DDA analysis. These weak vertical velocities are difficult for the 90s_VORT_3DADV DDA to retrieve accurately (Fig. 5.8b). The errors at 2136 UTC stand out, but at this time the vorticity constraint cannot be applied due to the edge of the data coverage area. It was decided to include this area in the verification since this type of error could be a reason one would choose an EnKF analysis over a DDA.

As one might expect due to the filter divergence, the 30-s volume scan EnKF vertical velocities are much too strong for almost the entire verification period, and there is little correlation between the EnKF retrieved vertical velocities and the SMART-R3 observations (Fig. 5.9a). The amplitudes of the 90-s volume scan EnKF vertical velocities earlier in the cycling period are closer to those observed by the SMART-R3, but later in the cycling period, the amplitudes begin to increase as the filter divergence begins to impact the data coverage area (Fig. 5.9b). The 150-s volume scan EnKF experiment vertical velocities are the closest to the SMART-R3 observations out of the three experiments (Fig. 5.9c). The analysis vertical velocities are moderately correlated to the observations before 2142 UTC. One particularly skillful analysis time for this experiment is at 2136 UTC. This is noteworthy since all DDA experiments struggle at retrieving the weak updraft observed at that time. The analyses have a likely incorrect updraft after 2142 UTC, but unfortunately, this cannot be verified because there are no SMART-R3 data at this time. The 150-s vertical velocities are most likely better before 2142 UTC because the filter divergence developed gradually in this experiment, but the updraft after 2142 UTC might be the result of the filter divergence beginning to affect the data-coverage area. Finally, the EnKF experiment with spatially thinned observations and higher observation standard deviation has vertical velocity magnitudes that are similar to the 150-s volume-scan EnKF experiment, but there is much less vertical detail (Fig. 5.8). This reduced detail is not surprising since the observations are significantly underfitted in this experiment and therefore the analyses are more reliant on the model output.

The 90s_VORT_3DADV experiment has slightly different verification statistics for the EnKF analysis times than for the entire DDA analysis times (Fig. 5.10). The correlation coefficient falls to 0.22 and the difference from the observed vertical velocity standard deviation is slightly higher resulting in a CRMSE of 1.612 m s^{-1}. Unsurprisingly, the verification statistics for the 30-s volume scan experiment are exceptionally poor. The standard deviation of the retrieved vertical velocities is over three times the observed standard deviation and the correlation coefficient is slightly negative, which suggests that there is little skill in these analyses. The 90-s volume scan experiment has a lower standard deviation, but the correlation coefficient is still small. The verification statistics are quite different for the 150-s volume scan experiment. The standard deviation of the analyses' vertical velocities are only slightly less than observed, and the correlation coefficient is 0.61. This results in a CRMSE that is less than 1 m s^{-1}, which is less than the best DDA experiment.

It is important to note that the updraft after 2142 UTC is not factored into the verification statistics due to the missing SMART-R3 data. Even considering this, these results suggest that EnKF analyses can produce quality vertical velocity analyses. Also, considering that filter divergence was slowly developing during the cycling in this experiment these good verification statistics are somewhat surprising. Finally, the experiment with the higher observation variance and thinned observations has a low standard deviation of the analysis vertical velocities and a slightly negative correlation coefficient. The CRMSE of this experiment is actually lower than the 90s_VORT_3DADV CRMSE because of the low standard deviation. Essentially, the weak and smoothed vertical velocities in these EnKF analyses result in little error because the observed vertical velocities are weak. Even though the CRMSE is low, the negative correlation coefficient suggests that these analyses would not be useful.

The 150-s volume scan EnKF vertical velocities at the SMART-R3 verification point had lower RMSE at higher elevations than the 90s_VORT_3DADV vertical velocities (Fig. 5.11). This result is in agreement with the OSSE study results in Potvin and Wicker (2012). The higher observation error variance and thinned observation EnKF analyses also had low RMSE above 2 km, but had higher RMSE below 2 km. This is due to the vertical smoothness of the vertical velocities in this experiment. The other EnKF experiments have RMSE that become greater than the 90s_VORT_3DADV RMSE with height, but, again, this is to be expected with the aggressive filter divergence in these experiments.

These verification statistics further highlight the difficulties with using EnKF analyses with high-resolution rapid-scan radar data. The experiment that produced the best results assimilated 250 m gridded radar observations, but had temporally thinned data and slow-building catastrophic filter divergence that would have likely affected the results if the cycles continued past the verification period. When observations were spatially thinned and the observation error standard deviation was increased, the filter divergence problem was avoided, but there was very little detail in the vertical velocities. This shows that there is a delicate balance between assimilating observations with enough detail to produce accurate vertical velocities and thinning observations to prevent filter divergence.

5.5 Summary

EnKF analyses have recently become more popular for analyses of convective storms, but are still a relatively new type of analysis. EnKF analyses show promise, but they have not been used very often to produce high-resolution analyses with rapid-scan radar data. This chapter shows some of the difficulties that can arise when using EnKF analyses in this manner. The large number of observations that are assimilated from the rapid-scan radars requires intervention to maintain sufficient ensemble spread. In this study, adaptive covariance inflation was the technique used to maintain ensemble spread, but the large values of inflation that were needed caused catastrophic filter divergence to develop in the system. The catastrophic filter divergence ruined the analyses outside of the data coverage area, rendering those regions useless for interpretation. In the worst case, the catastrophic filter divergence caused model failure that prevented the full assimilation period to be completed. The analyses that performed well at the verification point only assimilated observations from volume scans every 150 s, but even in this experiment catastrophic filter divergence was slowly developing by the end of the cycling period. However, this analysis had better verification statistics than the best DDA analysis from Chapter 4, which suggests that if the filter divergence problem can be avoided, EnKF analyses could be more accurate than DDAs. Due to this filter divergence problem, EnKF analyses will likely not benefit from assimilating high-resolution rapid-scan radar data at fine scales until a solution for this problem can be found. In fact, the large computational cost of EnKF analyses, the reduced number of possible analyses per volume scan, and the filter divergence issues indicate that, currently, DDAs may be more applicable than EnKF analyses with rapid-scan radar data, especially when a vorticity constraint is used. Even so, the 150 s volume scan experiment is somewhat promising, and future advancements in EnKF techniques could eventually make high-resolution EnKF analyses the preferred analysis technique for convective storms.

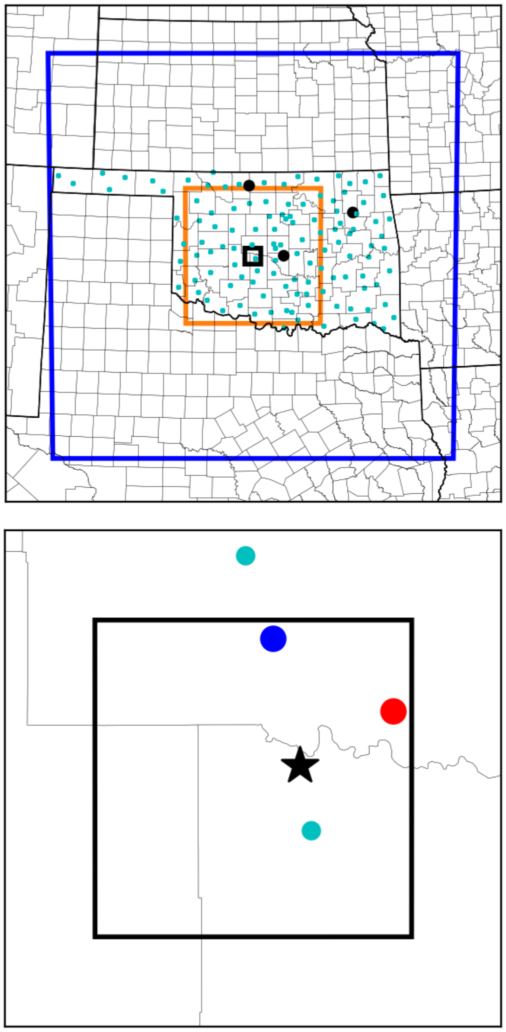

Figure 5.1: Domains used in the EnKF experiments (top). The blue square contains the outer domain for the WRF forecasts from the GEFS analyses that are used to calculate the initial ensemble perturbations. The orange square contains the outer domain for the EnKF experiments, and the black square contains the inner domain for the EnKF analyses. Locations of WSR-88Ds radars that have data assimilated at some point in the EnKF cycling are shown with black circles. The cyan circles show the locations of the Oklahoma Mesonet sites. The bottom plot is zoomed into the inner domain for the EnKF experiments. The red circle shows the location of RaXPol and the blue circle shows the location of the AIR. The SMART-R3 position is shown by a black star.

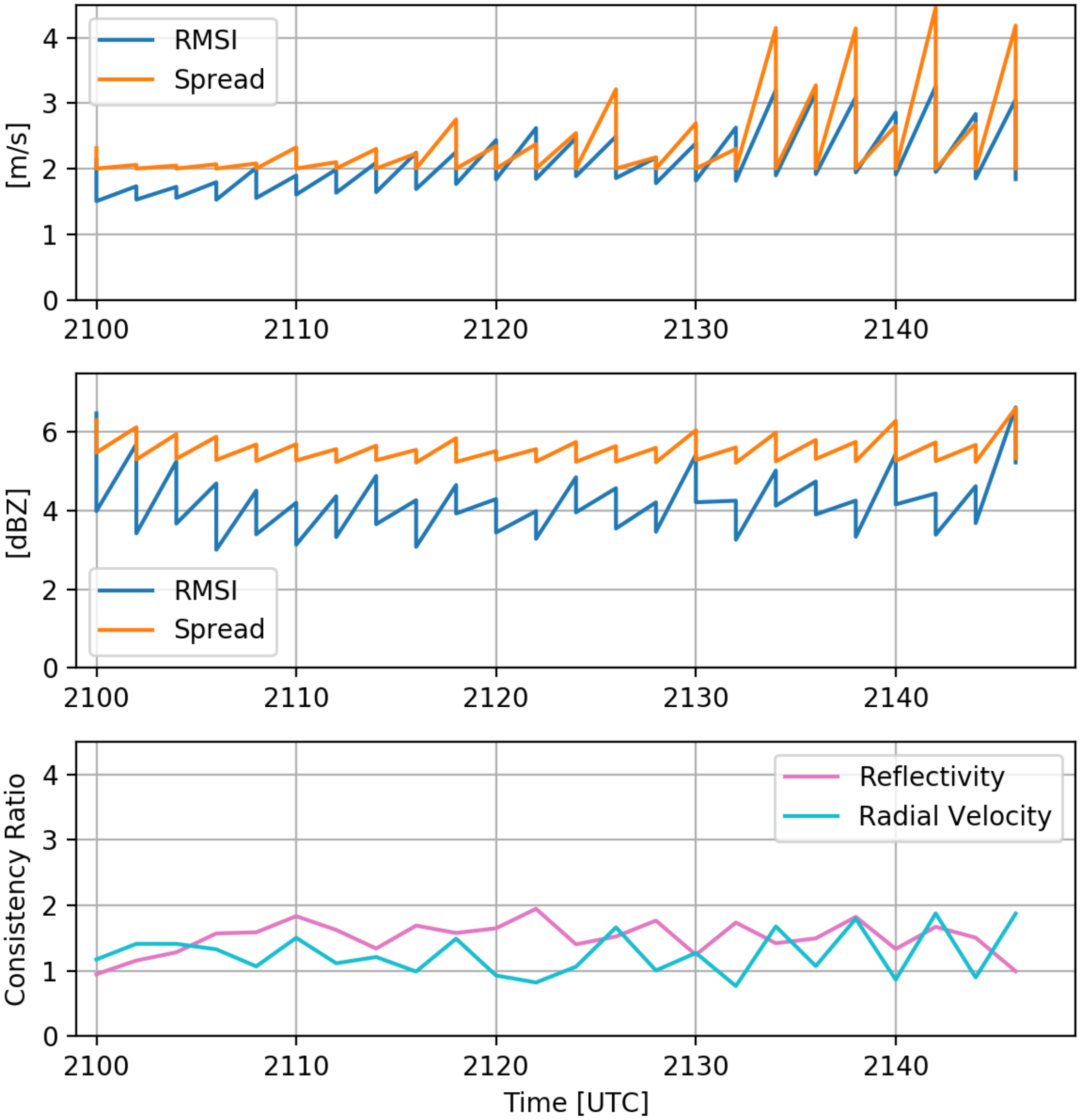

Figure 5.2: Forecast and analysis RMSI and total spread for (top) radial velocity and (middle) reflectivity for the 30-s volume scan EnKF experiment. The bottom plot shows the consistency ratios for radial velocity and reflectivity.

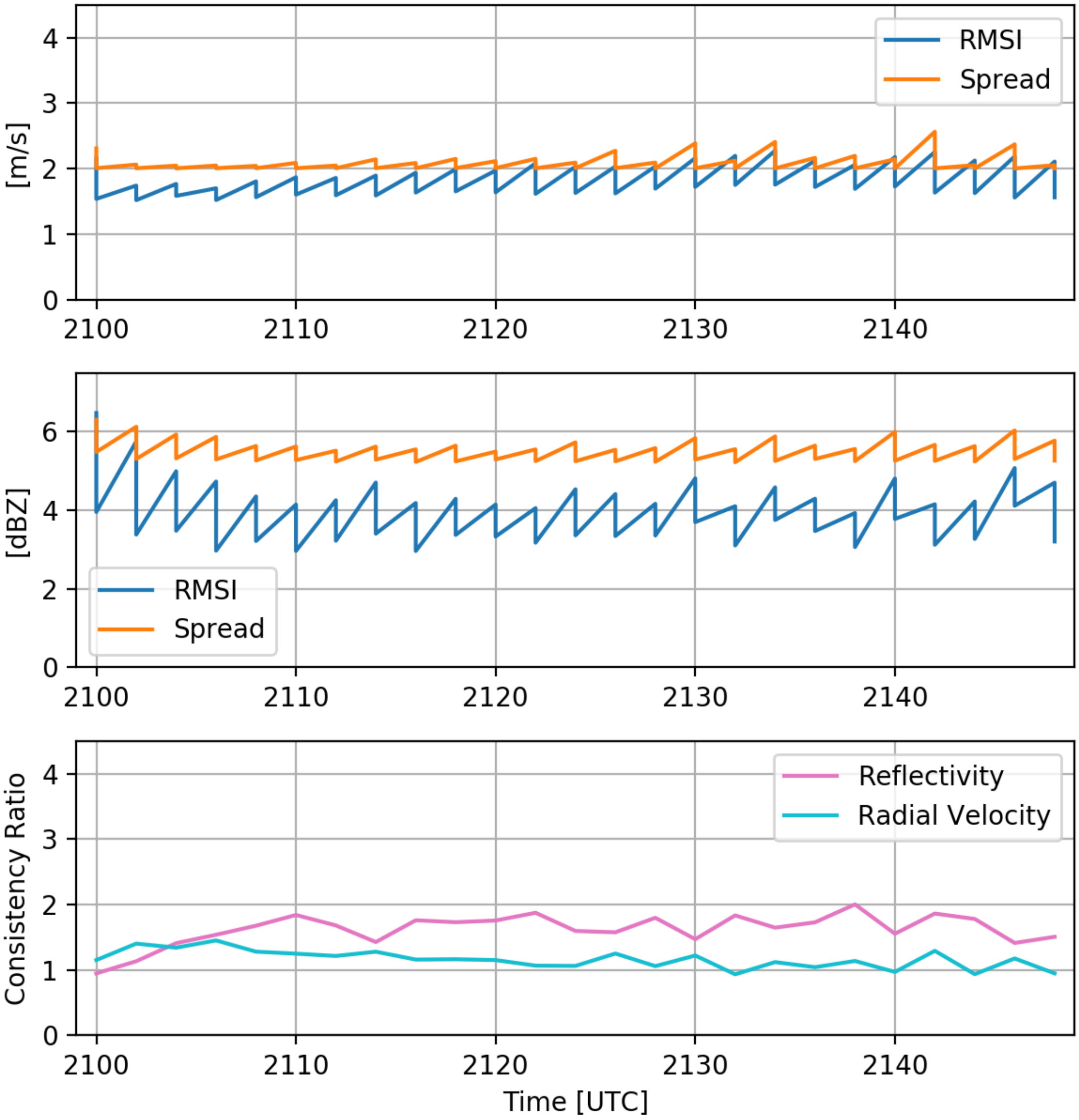

Figure 5.3: Same as Fig. 5.2 but for the 90-s volume scan EnKF experiment.

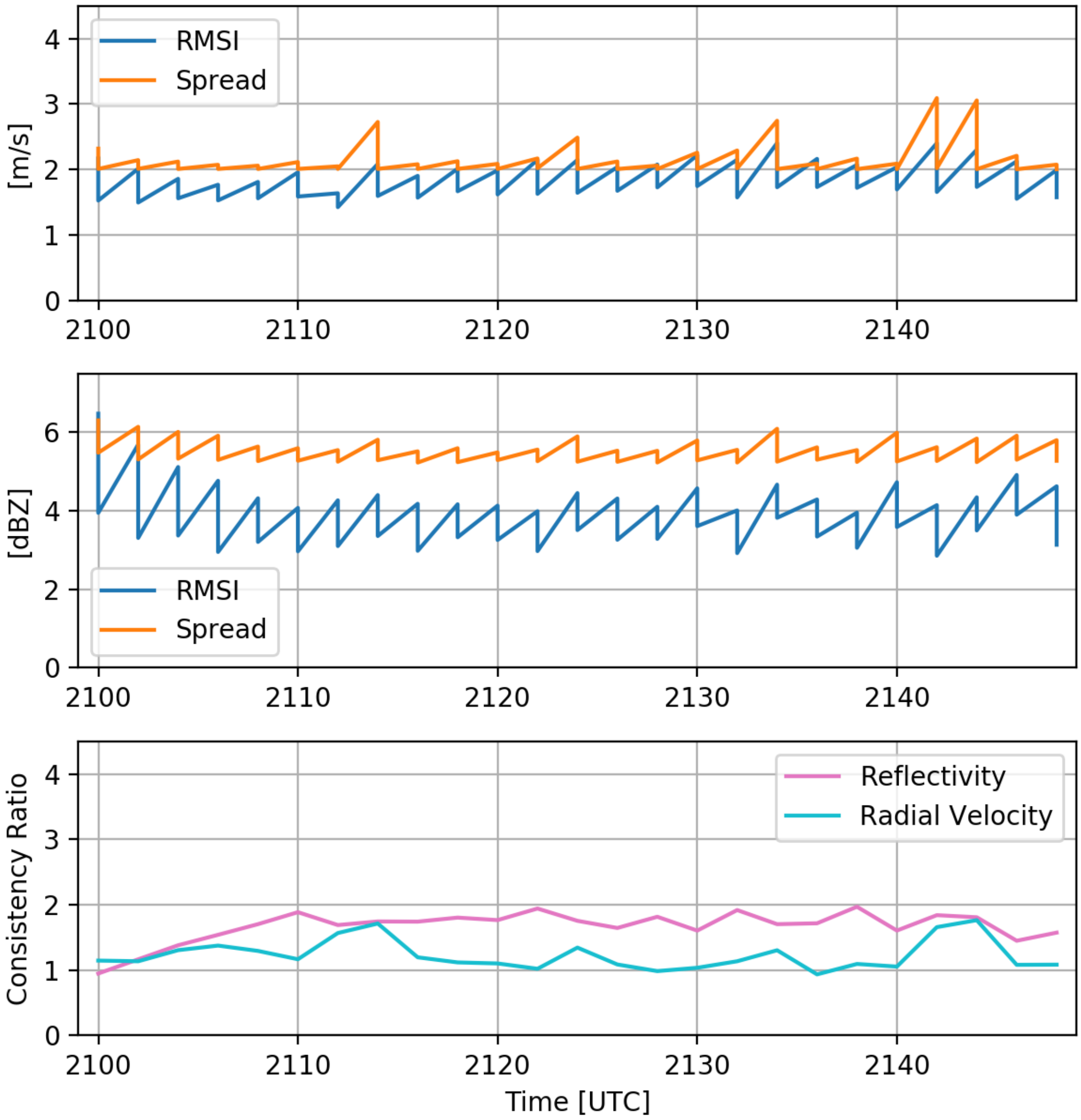

Figure 5.4: Same as Fig. 5.2 but for the 150-s volume scan EnKF experiment.

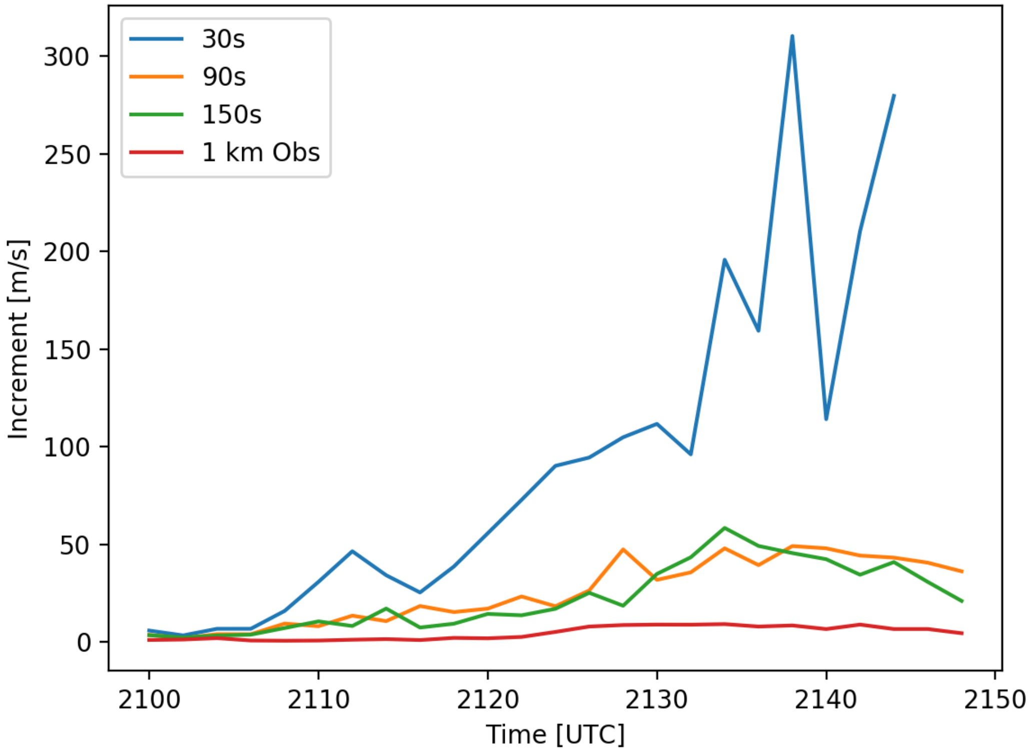

Figure 5.5: The maximum increment in vertical velocity for each cycle of the data assimilation.

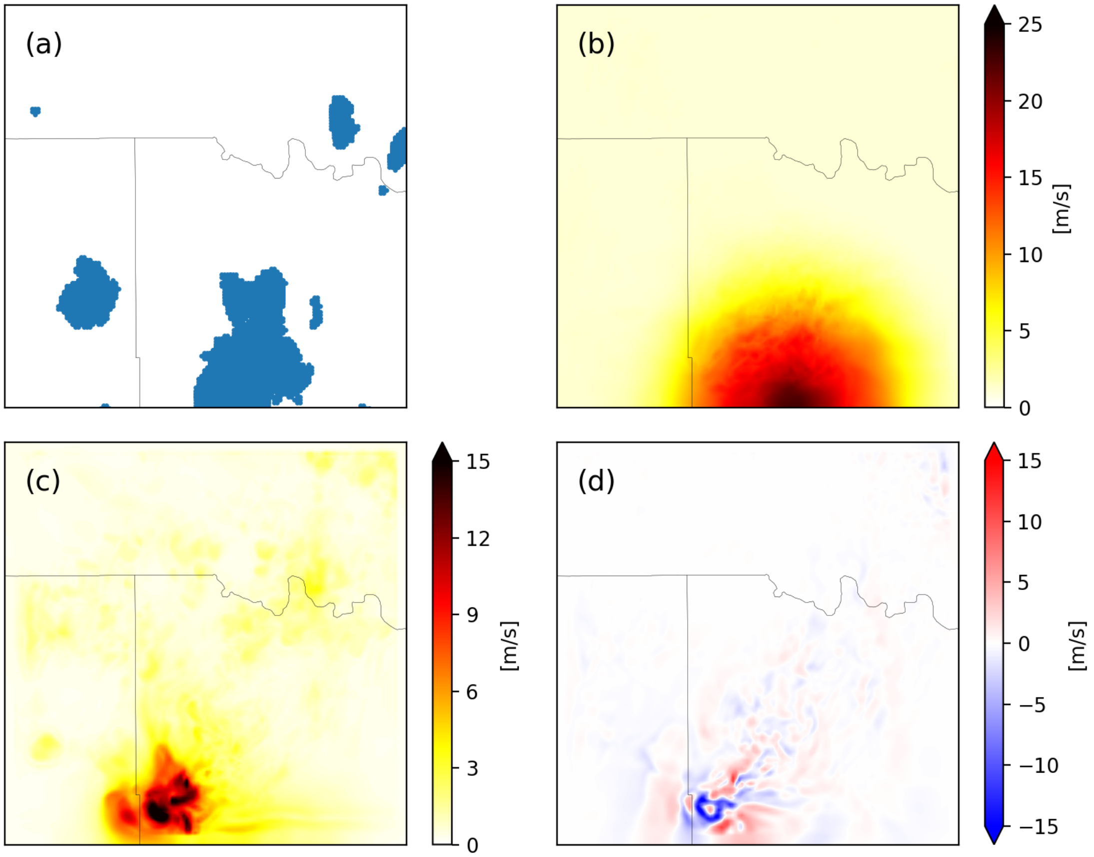

Figure 5.6: An overview of the catastrophic filter divergence problem using the 2110 UTC cycling time. (a) The locations that have a radial velocity observation from RaXPol in the column (shown in blue). (b) The maximum inflation values in the column prior to running the EnKF filter. (c) The maximum ensemble spread of vertical velocity in the column prior to assimilation. (d) The maximum vertical velocity increments applied to the analysis from the data assimilation.

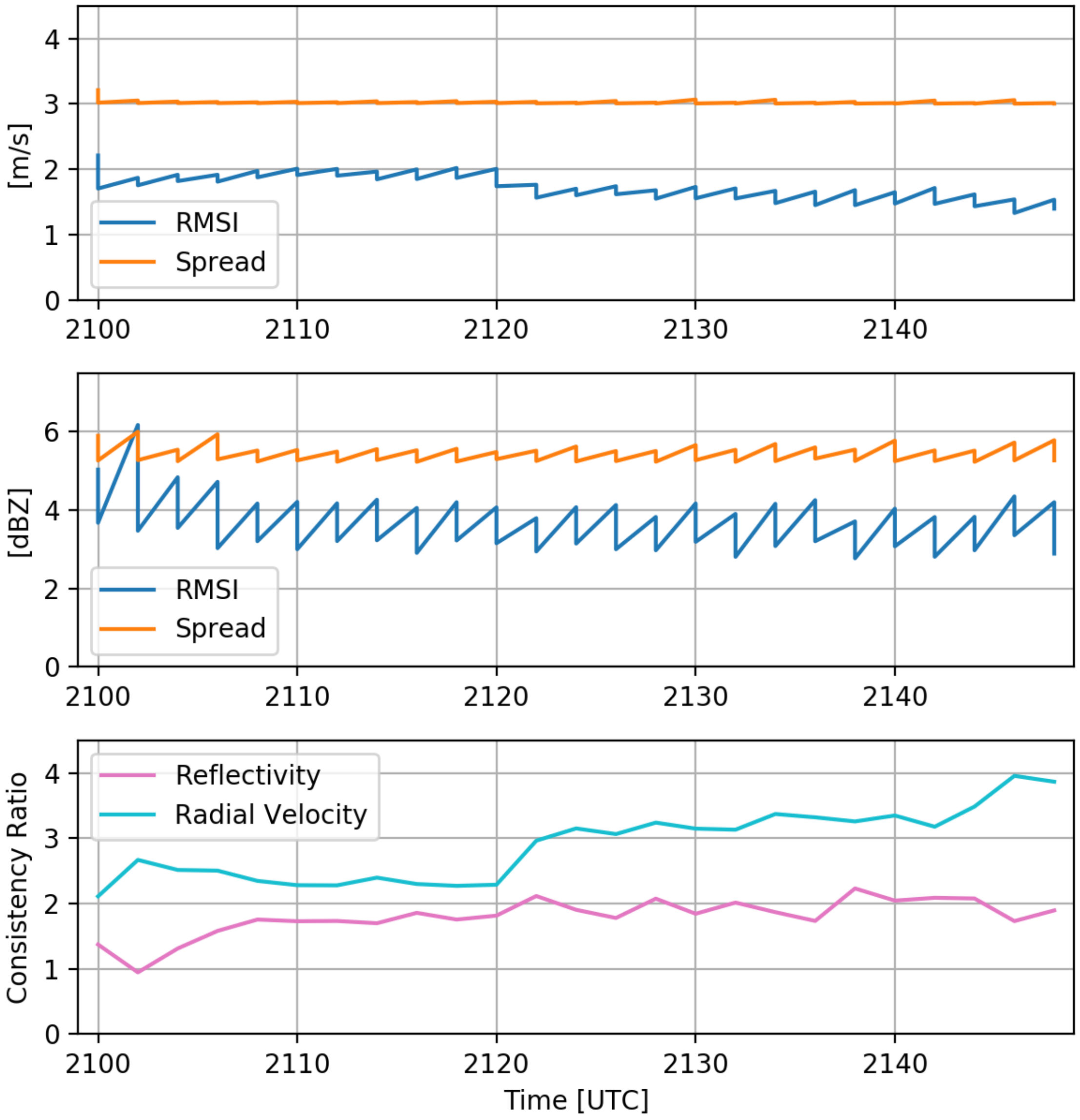

Figure 5.7: Same as Fig. 5.2 but for an EnKF experiment with 1-km spaced radial velocity observations and radial velocity observation error standard deviation set to 3 m s^{-1}.

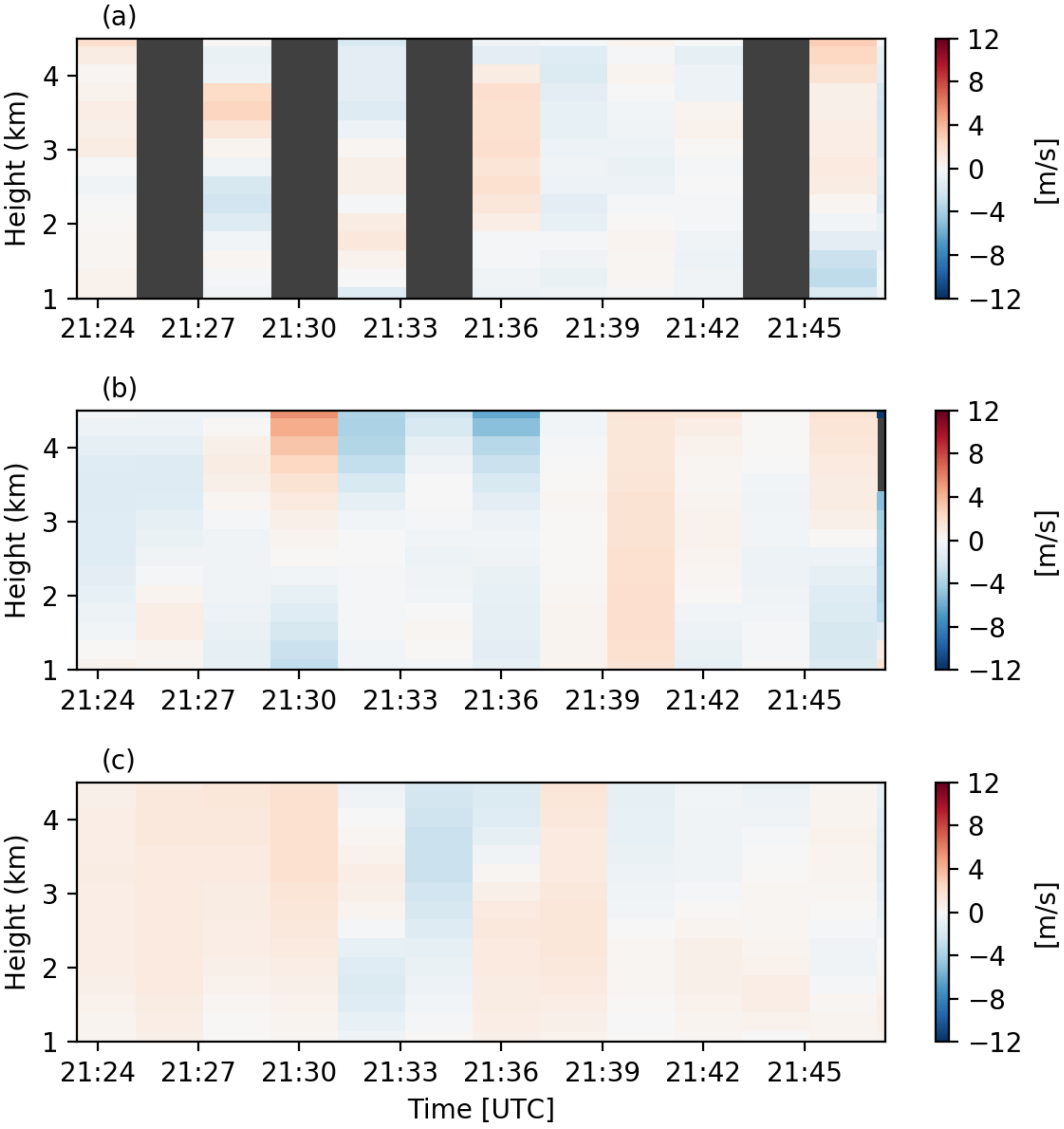

Figure 5.8: (a) The SMART-R3 vertical velocities interpolated to 250-m vertical resolution for the EnKF analysis times. (b) The 90s_VORT_3dADV DDA vertical velocities at the SMART-R3 verification point for the common analysis times with the EnKF analyses. (c) The probability-matched mean vertical velocities interpolated to the 250-m vertical resolution from the EnKF analyses that use 1-km spaced observations and higher observation error variance at the SMART-R3 verification point.

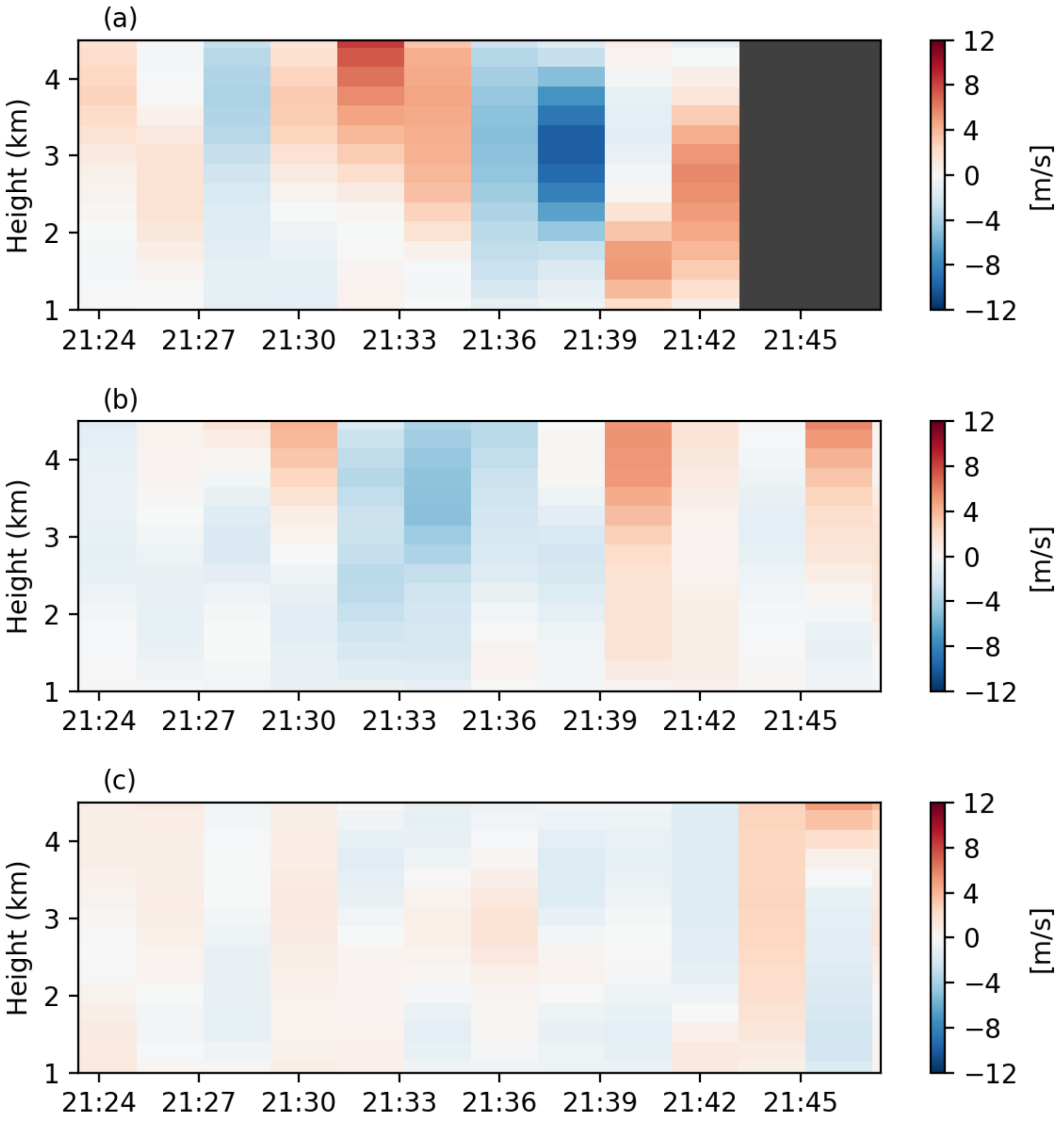

Figure 5.9: The EnKF probability-matched mean vertical velocities interpolated to 250-m vertical resolution at the SMART-R3 verification point for the (a) 30-s volume scan, (b) 90-s volume scan, and (c) 150-s volume scan experiments.

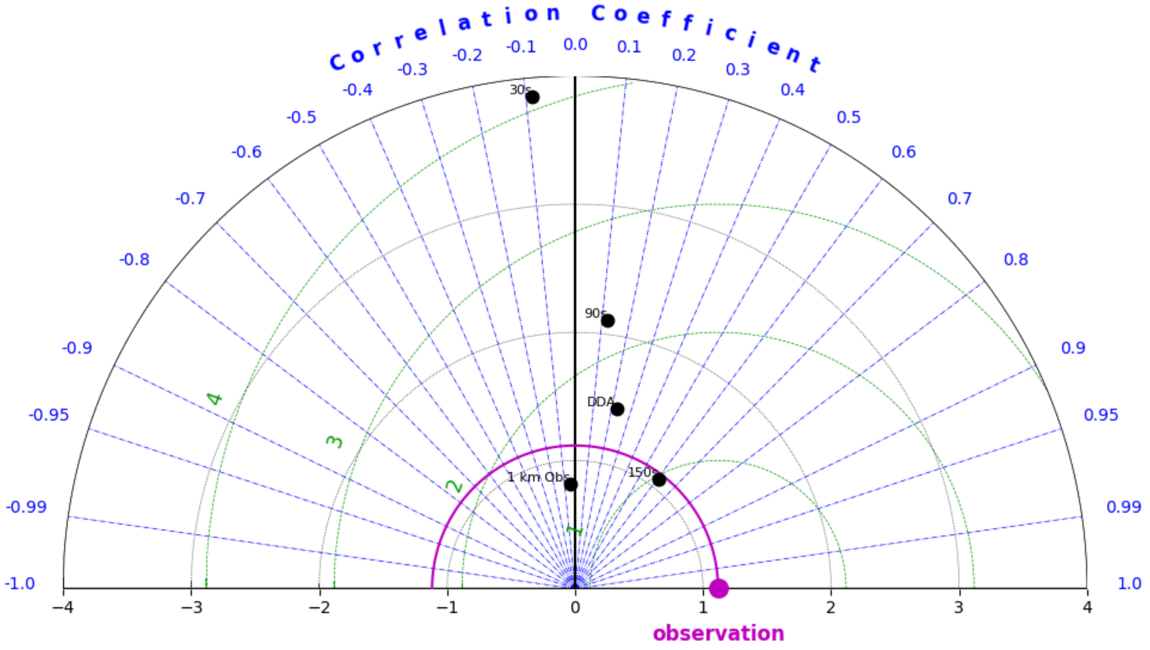

Figure 5.10: Taylor diagram for the EnKF vertical velocities at the SMART-R3 verification point. The diagram is similar to Fig. 4.11, but this diagram is two-sided due to the negative correlation coefficients in some of the experiments.

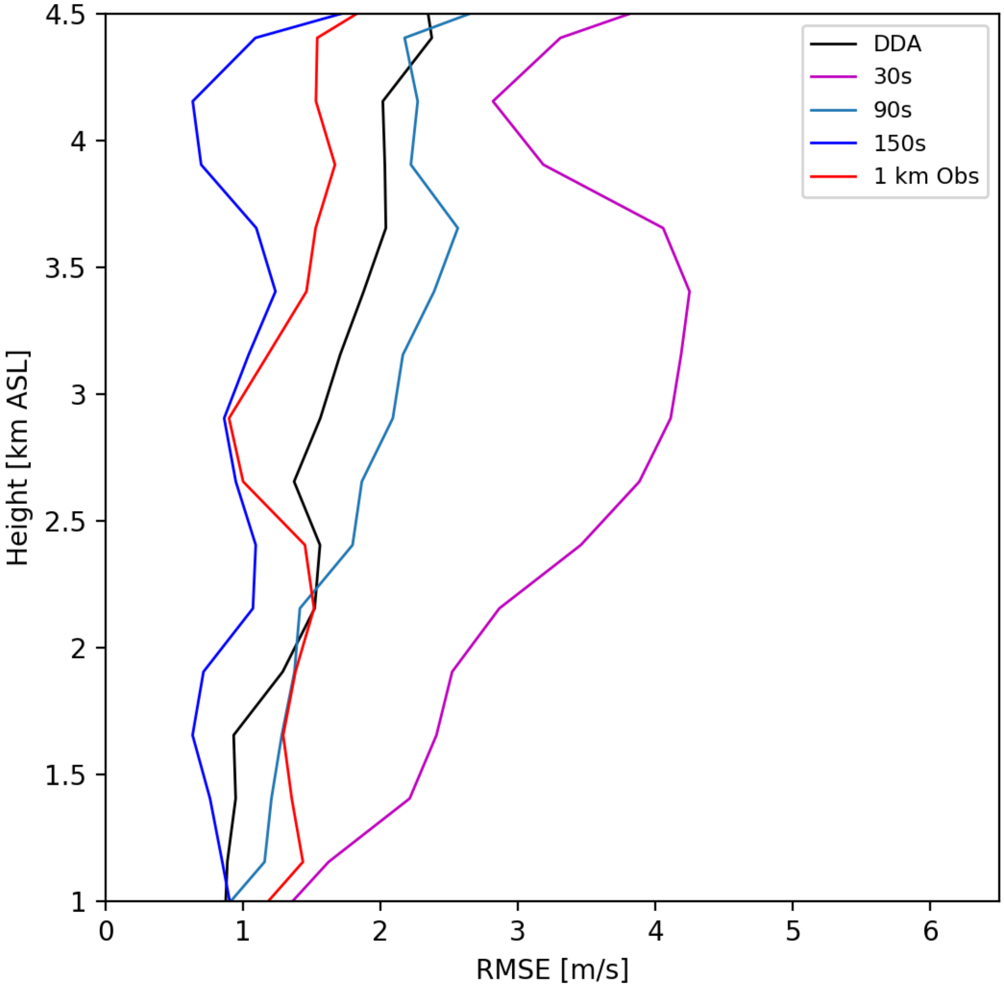

Figure 5.11: Profiles of EnKF vertical velocity RMSE at the SMART-R3 verification point.

Chapter 6

Conclusions

Kinematic analyses of convective storms are vital for further understanding of high impact weather events such as high winds, hail, tornadoes, and flash flooding. These analyses are often created using radial velocity observations from two or more radars. In these analyses, the vertical velocity component is the most difficult to accurately retrieve since radial velocity observations do not adequately observe the vertical component of motion. The deficiency of vertical velocity retrievals is troubling as the vertical component of motion is what is actually leading to the condensation and deposition of water vapor that essentially leads to the many impacts associated with convective storms. In supercell thunderstorms vertical motions are vitally important to the generation of vorticity due to tilting and stretching and are critical for the development of tornadoes. Therefore, poor vertical velocity analyses provide an incomplete and sometimes misleading picture of the kinematics of convective storms.

In this study, real rapid-scan radar data were used to evaluate the performance of a promising DDA technique that uses a vertical vorticity equation constraint in addition to the typical observation and mass conservation constraints. Prior OSSE studies found that this DDA technique produces more accurate vertical velocities than traditional DDA techniques when radar volume scan times are short. The dependence of the retrieval on radar volume scan time is due largely to the estimation of the vorticity tendency that is necessary when using the vorticity constraint.

Before this study, the vorticity constraint DDA technique had not been tested with actual rapid-scan radar data. Using RaXPol and the AIR, a dual-Doppler dataset was collected with a maximum volume scan time of 30 s. The vorticity constraint DDA performed as expected based on the previous OSSE results, but by testing with real radar data some additional features of the technique were discovered. In general, the vorticity equation constrained DDA produced more accurate vertical velocity retrievals when the time between volume scans was shorter, however, unlike in the OSSE studies, the vorticity constraint DDA produced more accurate vertical velocities even though there was a minimal data void between the lowest data level and the ground. An unexpected finding, however, was that the vorticity equation constrained DDA is less susceptible to radar data errors. This became apparent as vorticity equation constrained DDAs did not retrieve nonphysical downdrafts in a region with sidelobe contamination while DDA techniques that only used a mass conservation constraint and observations did. The differences in the wind retrievals between the vorticity constraint DDAs and those that did not use a vorticity constraint created significant differences in trajectory analyses from the retrieved wind fields. At some locations in the DDA domain, the height differences in a 5-minute trajectory were over 3 km for the 125-m resolution DDAs. This highlights that the vertical velocity retrievals can significantly affect subsequent analyses from the DDA-retrieved wind fields to the point where different conclusions could be made depending on the type of DDA technique used.

An accurate estimation of the vorticity tendency is necessary for the vorticity constraint DDA to be successful. A technique where the provisional wind retrievals are advection-corrected to times closer to the actual analysis time before calculating the vorticity tendency was found to be successful in OSSE studies. However, prior versions of this technique used two-dimensional advection correction. Such advection correction is applied to each data level independently so discontinuities in the advection components could occur. Additionally, the technique could not account for vertical advection. In an attempt to further improve the vorticity tendency calculation, a three-dimensional advection correction technique was developed. This technique was similar to the original two-dimensional technique, but in the three-dimensional technique an entire volume of data can be advection-corrected at one time and vertical advection is included. The effects of the three-dimensional advection correction on the vorticity tendency estimation and ultimately the vertical velocity retrievals were mixed. For 30 s between volume scans, the three-dimensional advection correction slightly degraded the vertical velocity retrievals, but for longer volume scan times it improved vertical velocity retrievals. The improvement in the vertical velocity retrievals with longer volume scans times is the more important result, as basic vorticity tendency estimation techniques, such as a simple centered difference, do well at short times between volume scans, but are exceptionally poor at longer volume scan times. Therefore, the three-dimensional advection correction technique could allow for the vorticity constraint DDA to be used with other datasets with less than rapid scanning. Of course, these results are limited to one case and further testing of the three-dimensional advection correction vorticity tendency calculation needs to be done with other datasets. While the three-dimensional advection correction was developed for the vorticity tendency calculation, it has uses beyond this application and can be applied in a similar manner to problems that already use advection correction techniques.

The EnKF portion of this study was unfortunately not as successful as the DDA component. The large number of observations associated with high-resolution rapid-scan radars created catastrophic filter divergence issues that degraded the analyses. While disappointing, the results still provide important information about potential problems that can arise when assimilating rapid-scan radar data. The filter divergence issue was partially delayed when the observations where temporally thinned to 150-s volume scans, but even with this aggressive thinning, catastrophic filter divergence was slowly developing in the ensembles. Spatially thinning the radar observations and increasing the radial velocity observation error variance prevented the filter divergence, but the resulting analyses were too smooth due to the significant underweighting of the observations.

The EnKF experiments that assimilated volume scans that were temporally thinned to 150-s intervals actually had better vertical velocity verification statistics than the best DDA. This is an interesting result as it supports the notion that EnKF analyses could be better than DDAs, but it also comes with the caveat that catastrophic filter divergence was developing in the ensemble and a longer cycling period would have had worsening results. At this time, due to the difficulties with assimilating rapid scan radar data, DDAs that include a vorticity constraint are likely the more reliable analysis for vertical velocity retrievals when using rapid scan radars. DDAs with rapid-scan radars can provide more analysis times than EnKF analyses and can also make use of all of the data provided by the radar to conduct analyses on a finer scale. The results of the 150-s volume scan experiments, however, indicate that when radar volume scans are less frequent, EnKF analyses may be preferred.

Additional research needs to be conducted on the vorticity constraint DDAs and EnKF analyses from radars that are not rapid scan now that vorticity tendency calculation techniques have improved. The results in this study may have been too favorable to the longer time between volumes scans since the actual volume was collected rapidly, so there were negligible advection errors when performing the DDAs and EnKF analyses. For EnKF analyses, the assimilation of a full volume of data in every assimilation cycle instead of partial volumes, as would occur if the volume scan time was truly 150 s, likely improved results. Assessing the skill of these analyses when advection errors are present should be a future priority because they are present in many existing datasets that could possibly benefit from the vorticity constraint DDA or EnKF analyses. Even though these datasets exist, a new dataset would likely be required for these tests due to the lack of vertical velocity verification.

Overall, the results of this study indicate that vertical velocity retrievals would benefit from the combination of rapid-scan radars and vorticity constraint DDAs. This is a result that supports the development of further rapid-scan radars and suggests that these radars should be used whenever possible for future field campaigns where wind retrievals are to be performed with the data, so the vorticity constraint DDA can easily be applied.

Reference List

Aksoy, A., D. C. Dowell, and C. Snyder, 2009: A multi-case comparative assessment of the ensemble Kalman filter for assimilation of radar observations. Part I: Storm-scale analyses. *Mon. Wea. Rev.*, **137**, 1805–1824.

Alford, A. A., M. I. Biggerstaff, and G. D. Carrie, 2019: Mobile ground-based smart radar observations and wind retrievals during the landfall of Hurricane Harvey (2017). *Geosci. Data. J.*, **6**, 205–213.

Anderson, J. L., 2001: An ensemble adjustment Kalman filter for data assimilation. *Mon. Wea. Rev.*, **129**, 2884–2903.

Anderson, J. L., 2009: Spatially and temporally varying adaptive covariance inflation for ensemble filters. *Tellus A*, **61**, 72–83.

Anderson, J. L., T. Hoar, K. Raeder, H. Liu, R. T. N. Collins, and A. Arellano, 2009: The Data Assimilation Research Testbed: A community facility. *Bull. Amer. Meteor. Soc.*, **90**, 1283–1296.

Armijo, L., 1969: A theory for the determination of wind and precipitation velocities with Doppler radars. *J. Atmos. Sci.*, **26**, 570–573.

Arnott, N., R. R., W. Y. P., J. M., and J. Lutz, 2003: A solar alignment technique for determining mobile radar pointing angles. *31st International Conference on Radar Meteorology*, Amer. Meteor. Soc, Seattle,WA, P3C.12, https://ams.confex.com/ams/32BC31R5C/techprogram/paper_64336.htm.

Atlas, D., R. C. Srivastava, and R. S. Sekhon, 1973: Doppler radar characteristics of precipitation at vertical incidence. *Rev. Geophys. Space Phys.*, **11**, 1–35.

Austin, P. M., 1987: Relation between measured radar reflectivity and surface rainfall. *Mon. Wea. Rev.*, **115**, 1053–1070.

Banghoff, J., D. Stensrud, and M. Kumjian, 2018: Convective boundary layer depth estimation from S-Band dual-polarization radar. *J. Atmos. Oceanic Technol.*, **35**, 1723–1733.

Benjamin, S. G., and Coauthors, 2016: A North American hourly assimilation and model forecast cycle: The Rapid Refresh. *Mon. Wea. Rev.*, **144**, 1669–1694.

Biggerstaff, M., and Coauthors, 2005: The Shared Mobile Atmospheric Research and Teaching Radar: A collaboration to enhance research and teaching. *Bull. Amer. Meteor. Soc.*, **86**, 1263–1274.

Biggerstaff, M. I., and R. A. Houze, 1993: Kinematics and microphysics of the transition zone of the 10-11 June 1985 squall line. *J. Atmos. Sci.*, **50**, 3091–3110.

Blaylock, B., J. Horel, and S. Liston, 2017: Cloud archiving and data mining of High Resolution Rapid Refresh model output. *Computers and Geosciences*, **109**, 43–50.

Bluestein, H., K. Thiem, J. Snyder, and J. Houser, 2018: The multiple-vortex structure of the El Reno, Oklahoma, tornado on 31 May 2013. *Mon. Wea. Rev.*, **146**, 2483–2502.

Bluestein, H. B., J. C. Snyder, and J. B. Houser, 2015: A multiscale overview of the El Reno, Oklahoma, tornadic supercell of 31 May 2013. *Wea. Forecasting*, **30**, 525–552.

Brandes, E. A., 1977: Flow in severe thunderstorms observed by dual-Doppler radar. *Mon. Wea. Rev.*, **105**, 113–120.

Brandes, E. A., R. P. Davies-Jones, and B. C. Johnson, 1988: Streamwise vorticity effects on supercell morphology and persistence. *J. Atmos. Sci.*, **45**, 947–963.

Brock, F. V., K. C. Crawford, R. L. Elliot, G. W. Cuperus, S. J. Stadler, H. L. Johnson, and M. D. Eilts, 1995: The oklahoma mesonet: A technical overview. *J. Atmos. Oceanic Technol.*, **12**, 5–19.

Brooks, H. E., and Coauthors, 2018: A century of progress in severe convective storm research and forecasting. *Meteorological Monographs*, **59**, 18.1–18.41.

Browning, K. A., 1964: Airflow and precipitation trajectories within severe local storms which travel to the right of the winds. *J. Atmos. Sci.*, **21**, 634–639.

Buban, M., C. Ziegler, E. Rasmussen, and Y. Richardson, 2007: The dryline on 22 May 2002 during IHOP: Ground-radar and in situ data analyses of the dryline and boundary layer evolution. *Mon. Wea. Rev.*, **135**, 2473–2505.

Cho, J. Y. N., and J. M. Kurdzo, 2019: Weather radar network benefit model for tornadoes. *J. Appl. Meteor. Climatol.*, **58**, 971–987.

Cho, J. Y. N., and J. M. Kurdzo, 2020: Weather radar network benefit model for flash flood casualty reduction. *J. Appl. Meteor. Climatol.*, **59**, 589–604.

Clark, A. J., 2017: Generation of ensemble mean precipitation forecasts from convection-allowing ensembles. *Wea. Forecasting*, **32**, 1569–1583.

Conrad, D. M., and K. R. Knupp, 2019: Doppler radar observations of horizontal shearing instability in quasi-linear convective systems. *Mon. Wea. Rev.*, **147**, 1297–1318.

Conway, J. W., and D. S. Zrnić, 1993: A study of embryo production and hail growth using dual-Doppler and multiparameter radars. *Mon. Wea. Rev.*, **121**, 2511–2528.

Cressman, G. P., 1959: An operational objective analysis system. *Mon. Wea. Rev.*, **87**, 367–374.

Crum, T. D., and R. L. Alberty, 1993: The WSR-88D and the WSR-88D Operational Support Facility. *Bull. Amer. Meteor. Soc.*, **74**, 1669–1687.

Crum, T. D., R. E. Saffle, and J. W. Wilson, 1998: An update on the NEXRAD program and future WSR-88D support to operations. *Wea. Forecasting*, **13**, 253–262.

Dahl, N. A., A. Shapiro, C. K. Potvin, A. Theisen, J. G. Gebauer, A. D. Schenkman, and M. Xue, 2019: High-resolution, rapid-scan dual-Doppler retrievals of vertical velocity in a simulated supercell. *J. Atmos. Oceanic Technol.*, **36**, 1477–1500.

Davenport, C., and M. Parker, 2015: Observations of the 9 June 2009 dissipating supercell from VORTEX2. *Wea. Forecasting*, **30**, 368–388.

Doviak, R. J., P. S. Ray, R. G. Strauch, and L. J. Miller, 1976: Error estimation in wind fields derived from dual-Doppler radar measurement. *J. Atmos. Oceanic Technol.*, **15**, 868–878.

Doviak, R. J., and D. S. Zrnić, 1993: *Doppler Radar and Weather Observations*. Academic Press, 562 pp.

Dowell, D. C., and H. B. Bluestein, 1997: The Arcadia, Oklahoma, storm of 17 May 1981: Analysis of a supercell during tornadogenesis. *Mon. Wea. Rev.*, **125**, 2562–2582.

Dowell, D. C., and A. Shapiro, 2003: Stability of an iterative dual-Doppler wind synthesis in Cartesian coordinates. *J. Atmos. Oceanic Technol.*, **20**, 1552–1559.

Dowell, D. C., and L. J. Wicker, 2009: Additive noise for storm-scale ensemble data assimilation. *J. Atmos. Oceanic Technol.*, **26**, 911–927.

Dowell, D. C., L. J. Wicker, and C. Snyder, 2011: Ensemble Kalman filter assimilation of radar observations of the 8 May 2003 Oklahoma City supercell: Influences of reflectivity observations on storm-scale analysis. *Mon. Wea. Rev.*, **139**, 272–294.

Dudhia, J., 1989: Numerical study of convection observed during the winter monsoon experiment using a mesoscale two-dimensional model. *J. Atmos. Sci.*, **46**, 3077–3107.

Evensen, G., 1994: Sequential data assimilation with a nonlinear quasi-geostrophic model using Monte Carlo methods to forecast error statistics. *J. Geophys. Res.*, **99**, 10 143–10 162.

Gal-Chen, T., 1978: A method for the initialization of the anelastic equations: Implications for matching models with observations. *Mon. Wea. Rev.*, **106**, 587–606.

Gal-Chen, T., 1982: Errors in fixed and moving frame of references: Applications for conventional and Doppler radar analysis. *J. Atmos. Sci.*, **39**, 2279–2300.

Gao, J., M. Xue, A. Shapiro, and K. K. Droegemeier, 1999: A variational method for the analysis of three-dimensional wind fields from two Doppler radars. *Mon. Wea. Rev.*, **127**, 2128–2142.

Gao, J., M. Xue, A. Shapiro, Q. Xu, and K. K. Droegemeier, 2001: Three-dimensional simple adjoint velocity retrieval from single Doppler radar. *J. Atmos. Oceanic Technol.*, **18**, 26–38.

Gaspari, G., and S. Cohn, 1999: Construction of correlation functions in two and three dimensions. *Quart. J. Roy. Meteor. Soc.*, **125**, 723–757.

Gerstner, E. M., and G. Heinemann, 2008: Real-time areal precipitation determination from radar by means of statistical objective analysis. *J. Hydrol*, **352**, 296–308.

Girardin-Gondeau, J., F. Baudin, and J. Testud, 1991: Comparison of coded waveforms for an airborne meteorological doppler radar. *J. Atmos. Oceanic Technol.*, **8**, 234–246.

Gottwald, G. A., and A. J. Majda, 2013: A mechanism for catastrophic filter divergence in data assimilation for sparse observation networks. *Nonlin. Processes Geophys.*, **20**, 705–712.

Griffin, C., D. Bodine, J. Kurdzo, A. Mahre, and R. Palmer, 2019: High-temporal resolution observations of the 27 May 2015 Canadian, Texas, tornado using the Atmospheric Imaging Radar. *Mon. Wea. Rev.*, **147**, 873–891.

Hane, C. E., R. B. Wilhelmson, and T. Gal-Chen, 1981: Retrieval of thermodynamic variables within deep convective clouds: Experiments in three dimensions. *Mon. Wea. Rev.*, **109**, 564–576.

Hersbach, H., and Coauthors, 2020: The ERA5 global reanalysis. *Quart. J. Roy. Meteor. Soc.*, In Press.

Heymsfield, G. M., 1978: Kinematic and dynamic aspects of the Harrah tornadic storm analyzed from dual-Doppler radar data. *Mon. Wea. Rev.*, **106**, 233–254.

Hong, S.-Y., S. Y. Noh, and J. Dudhia, 2006: Nonlocal boundary layer vertical diffusion in a medium-range forecast model. *Mon. Wea. Rev.*, **134**, 2318–2341.

Horn, B. K. P., and B. G. Schunck, 1981: Determining optical flow. *Artif. Intell.*, **17**, 185–203.

Houser, J. L., H. B. Bluestein, and J. C. Snyder, 2016: A finescale radar examination of the tornadic debris signature and weak-echo reflectivity band associated with a large, violent tornado. *Mon. Wea. Rev.*, **144**, 4101–4130.

Houtekamer, P. L., and F. Zhang, 2016: Review of the ensemble Kalman filter for atmospheric data assimilation. *Mon. Wea. Rev.*, **144**, 4489–4532.

Isom, B., and Coauthors, 2013: The Atmospheric Imaging Radar: Simultaneous volumetric observations using a phased array weather radar. *J. Atmos. Oceanic Technol.*, **30**, 655–675.

Johnson, A., X. Wang, J. Carley, L. Wicker, and C. Karstens, 2015: A comparison of multiscale GSI-based EnKF and 3DVar data assimilation using radar and conventional observations for midlatitude convective-scale precipitation forecasts. *Mon. Wea. Rev.*, **143**, 3087–3108.

Jung, Y., M. Xue, and M. Tong, 2012: Ensemble Kalman filter analyses of the 29–30 May 2004 Oklahoma tornadic thunderstorm using one- and two-moment bulk microphysics schemes, with verification against polarimetric radar data. *Mon. Wea. Rev.*, **140**, 1457–1475.

Kelly, D., A. J. Majda, and X. T. Tong, 2015: Concrete ensemble Kalman filters with rigorous catastrophic filter divergence. *Proc. Natl. Acad. Sci. USA*, **112**, 10 589–10 594.

Klazura, G., and D. Imy, 1993: A description of the initial set of analysis products available from the NEXRAD WSR-88D system. *J. Atmos. Sci.*, **74**, 1293–1312.

Knupp, K., J. Walters, and M. Biggerstaff, 2006: Doppler profiler and radar observations of boundary layer variability during the landfall of Tropical Storm Gabrielle. *J. Atmos. Sci.*, **63**, 234–251.

Kosiba, K., J. Wurman, Y. Richardson, P. Markowski, P. Robinson, and J. Marquis, 2013: Genesis of the Goshen County, Wyoming, Tornado on 5 June 2009 during VORTEX2. *Mon. Wea. Rev.*, **141**, 1157–1181.

Kosiba, K. A., and J. Wurman, 2014: Finescale dual-Doppler analysis of hurricane boundary layer structures in hurricane Frances (2004) at landfall. *Mon. Wea. Rev.*, **142**, 1874–1891.

Kurdzo, J., and Coauthors, 2017: Observations of severe local storms and tornadoes with the Atmospheric Imaging Radar. *Bull. Amer. Meteor. Soc.*, **98**, 915–935.

Lang, T. J., and S. A. Rutledge, 2002: Relationships between convective storm kinematics, precipitation, and lightning. *Mon. Wea. Rev.*, **130**, 2492–2506.

Lange, H., and G. C. Craig, 2014: The impact of data assimilation length scales on analysis and prediction of convective storms. *Mon. Wea. Rev.*, **142**, 3781–3808.

Laroche, S., and I. Zawadzki, 1995: Retrievals of horizontal winds from single-Doppler clear-air data by methods of cross correlation and variational analysis. *J. Atmos. Oceanic Technol.*, **12**, 721–738.

Leise, J. A., 1982: A multidimensional scale-telescoped filter and data extension package. NOAA Tech. Memo, ERL WPL-82, 19 pp.

Lhermitte, R., 1966: Probing air motion by doppler analysis of radar clear air returns. *J. Atmos. Sci.*, **23**, 575–591.

Li, L., W. Schmid, and J. Joss, 1995: Nowcasting of motion and growth of precipitation with radar over a complex orography. *J. Appl. Meteor.*, **34**, 1286–1300.

Mahoney, W. P., 1988: Gust front characteristics and the kinematics associated with interacting thunderstorm outflows. *Mon. Wea. Rev.*, **116**, 1474–1492.

Mahre, A., J. Kurdzo, D. Bodine, C. Griffin, R. Palmer, and T. Yu, 2018: Analysis of the 16 May 2015 Tipton, Oklahoma, EF-3 tornado at high spatiotemporal resolution using the Atmospheric Imaging Radar. *Mon. Wea. Rev.*, **146**, 2103–2124.

Mansell, E. R., C. L.Ziegler, , and E. C.Bruning, 2010: Simulated electrification of a small thunderstorm with two-moment bulk microphysics. *J. Atmos. Sci.*, **67**, 171–194.

Markowski, P., and Coauthors, 2012: The pretornadic phase of the Goshen County, Wyoming, supercell of 5 june 2009 intercepted by VORTEX2. Part I: Evolution of kinematic and surface thermodynamic fields. *Mon. Wea. Rev.*, **140**, 2887–2915.

Marquis, J., Y. Richardson, J. Wurman, and P. Markowski, 2008: Single- and dual-Doppler analysis of a tornadic vortex and surrounding storm-scale flow in the Crowell, Texas, supercell of 30 April 2000. *Mon. Wea. Rev.*, **136**, 5017–5043.

Matejka, T., and D. L. Bartels, 1998: The accuracy of vertical air velocities from doppler radar data. *Mon. Wea. Rev.*, **126**, 92–117.

McPherson, R. A., and Coauthors, 2007: Statewide monitoring of the mesoscale environment: A technical update on the oklahoma mesonet. *J. Atmos. Oceanic Technol.*, **24**, 301–321.

Mewes, J. J., and A. Shapiro, 2002: On use of the vorticity equation in dual-Doppler analysis of the vertical velocity field. *J. Atmos. Oceanic Technol.*, **19**, 543–567.

Miller, R. L., C. L. Ziegler, and M. I. Biggerstaff, 2020: Seven-Doppler radar and in situ analysis o the 25-26 June 2015 Kansas MCS during PECAN. *Mon. Wea. Rev.*, **148**, 211–240.

Mlawer, E. J., S. J. Taubman, P. D. Brown, M. J. Iacono, and S. A. Clough, 1997: Radiative transfer for inhomogeneous atmosphere: RRTM, a validated correlated-k model for the longwave. *J. Geophys. Res.*, **102**, 16 663–16 682.

Muth, X., M. Schneebeli, , and A. Berne, 2012: A sun-tracking method to improve the pointing accuracy of weather radar. *Atmos. Meas. Tech.*, **5**, 547– 555.

Nelson, S. P., and R. A. Brown, 1987: Error sources and accuracy of vertical velocities computed from multiple-Doppler radar measurements in deep convective storms. *J. Atmos. Oceanic Technol.*, **4**, 233–238.

Oye, R. C., C. Mueller, and S. Smith, 1995: Software for radar translation, visualization, editing, and interpolation. *27th Conference on Radar Meteorology*, Amer. Meteor. Soc, Vail, CO, 359–361.

O'Brien, J. J., 1970: Alternative solutions to the classical vertical velocity problem. *J. Appl. Meteor.*, **9**, 197–203.

Pazmany, A., J. Mead, H. Bluestein, J. Snyder, and J. Houser, 2013: A mobile rapid-scanning X-band polarimetric (RaXPol) Doppler radar system. *J. Atmos. Oceanic Technol.*, **30**, 1398–1413.

Potvin, C. K., D. Betten, L. J. Wicker, K. L. Elmore, and M. I. Biggerstaff, 2012a: 3DVAR versus traditional dual-Doppler wind retrievals of a simulated supercell thunderstorm. *Mon. Wea. Rev.*, **140**, 3487–3494.

Potvin, C. K., A. Shapiro, and M. Xue, 2012b: Impact of a vertical vorticity constraint in variational dual-doppler wind analysis: Tests with real and simulated supercell data. *J. Atmos. Oceanic Technol.*, **29**, 32–49.

Potvin, C. K., and L. J. Wicker, 2012: Comparison between dual-Doppler and EnKF storm-scale wind analyses: Observing system simulation experiments with a supercell thunderstorm. *Mon. Wea. Rev.*, **140**, 3972–3991.

Protat, A., and I. Zawadzki, 1999: A variational method for real-time retrieval of three-dimensional wind field from multiple-Doppler bistatic radar network data. *J. Atmos. Oceanic Technol.*, **16**, 432–449.

Rasmussen, E. N., and S. A. Rutledge, 1993: Evolution of quasi-two-dimensional squall lines. Part I: Kinematic and reflectivity structure. *J. Atmos. Sci.*, **50**, 2584–2606.

Rasmussen, E. N., and S. A. Rutledge, 1995: Single-Doppler velocity retrievals with Phoenix II data: clear air and microburst wind retrievals in the planetary boundary layer. *J. Atmos. Sci.*, **52**, 1265–1287.

Ray, P. S., and K. K. Wagner, 1976: Multiple Doppler radar observations of storms. *J. Geophys. Res.*, **3**, 189–191.

Ray, P. S., C. L. Ziegler, W. Bumgarner, and R. J. Serafin, 1980: Single- and multiple-Doppler radar observations of tornadic storms. *Mon. Wea. Rev.*, **108**, 1607–1625.

Rico-Ramirez, M., Gonzalez-Ramirez, I. E., Cluckie, and D. Han, 2009: Real-time monitoring of weather radar antenna pointing using digital terrain elevation and a Bayes clutter classifier. *Met. Apps.*, **16**, 227–236.

Rinehart, R. E., and E. T. Garvey, 1978: Three-dimensional storm motion detection by conventional weather radar. *Nature*, **273**, 287–289.

Sakov, P., G. Evensen, and L. Bertino, 2010: Asynchronous data assimilation with the enkf. *Tellus*, **62A**, 24–29.

Sasaki, Y., 1970: Some basic formalisms in numerical variational analysis. *Mon. Wea. Rev.*, **98**, 875–883.

Shapiro, A., C. K. Potvin, and J. Gao, 2009: Use of a vertical vorticity equation in variational dual-Doppler wind analysis. *J. Atmos. Oceanic Technol.*, **26**, 2089–2106.

Shapiro, A., P. Robinson, J. Wurman, and J. Gao, 2003: Single-Doppler velocity retrieval with rapid scan radar data. *J. Atmos. Oceanic Technol.*, **20**, 1758–1775.

Shapiro, A., K. M. Willingham, and C. K. Potvin, 2010: Spatially variable advection correction of radar data. Part I: Theoretical considerations. *J. Atmos. Sci.*, **67**, 3457–3470.

Simmons, K. M., and D. Sutter, 2005: WSR-88D Radar, tornado warnings, and tornado casualties. *Wea. Forecasting*, **20**, 301–310.

Skamarock, W. C., and Coauthors, 2008: A description of the Advanced Research WRF Version 3. *NCAR Tech. Note NCAR/TN-475+STR*, 113 pp.

Skinner, P. S., C. C. Weiss, L. J. Wicker, C. K. Potvin, and D. C. Dowell, 2015: Forcing mechanisms for an internal rear-flank downdraft momentum surge in the 18 May 2010 Dumas, Texas, supercell. *Mon. Wea. Rev.*, **143**, 4305–4330.

Snook, N., M. Xue, and Y. Jung, 2011: Analysis of a tornadic mesoscale convective vortex based on Ensemble Kalman filter assimilation of CASA X-Band and WSR-88D radar datas. *Mon. Wea. Rev.*, **139**, 3446–3468.

Snook, N., M. Xue, and Y. Jung, 2015: Multiscale EnKF assimilation of radar and conventional observations and ensemble forecasting for a tornadic mesoscale convective system. *Mon. Wea. Rev.*, **143**, 1035–1057.

Snyder, C., and F. Zhang, 2003: Assimilation of simulated Doppler radar observations with an ensemble Kalman filter. *Mon. Wea. Rev.*, **131**, 1663–1677.

Stratman, D. R., N. Yussouf, Y. Jung, T. A. Supinie, M. Xue, P. S. Skinner, and B. J. Putnam, 2020: Optimal temporal frequency of NSSL Phased Array Radar observations for an experimental Warn-on-Forecast system. *Wea. Forecasting*, **35**, 193–204.

Sun, J., and N. A. Crook, 1994: Wind and thermodynamic retrieval from single-doppler measurements of a gust front observed during Phoenix II. *Mon. Wea. Rev.*, **122**, 1075–1091.

Sun, J., and N. A. Crook, 2001: Real-time low-level wind and temperature analysis using single WSR-88D data. *Wea. Forecasting*, **16**, 117–132.

Supinie, T. A., N. Yussouf, Y. Jung, M. Xue, J. Cheng, and S. Wang, 2017: Comparison of the analyses and forecasts of a tornadic supercell storm from assimilating phased-array radar and WSR-88D observations. *Wea. Forecasting*, **32**, 1379–1401.

Tanamachi, R. L., L. J. Wicker, D. C. Dowell, H. B. Bluestein, D. T. Dawson, and M. Xue, 2013: Enkf assimilation of high-resolution, mobile Doppler radar data of the 4 May 2007 Greensburg, Kansas, supercell into a numerical cloud model. *Mon. Wea. Rev.*, **141**, 625–648.

Tanamachi, R. L., L. J. Wicker, D. C. Dowell, H. B. Bluestein, D. T. Dawson, and M. Xue, 2014: Numerical simulations of lightning and storm charge of the 29–30 May 2004 Geary, Oklahoma, supercell thunderstorm using EnKF mobile radar data assimilation. *Mon. Wea. Rev.*, **142**, 3977–3997.

Taylor, G. I., 1938: The spectrum of turbulence. *Proc. Roy. Soc. London*, **164A**, 476–490.

Taylor, K. E., 2001: Summarizing multiple aspects of model performance in a single diagram. *J. Geophys. Res.*, **106**, 7183–7192.

Tuttle, J. D., and G. B. Foote, 1990: Determination of the boundary layer airflow from a single doppler radar. *J. Atmos. Oceanic Technol.*, **7**, 218–232.

Wang, G., W. Wong, L. Liu, and H. Wang, 2013a: Application of multi-scale tracking radar echoes scheme in quantitative precipitation nowcasting. *Adv. Atmos. Sci.*, **30**, 448–460.

Wang, S., M.Xue, , and J.Min, 2013b: A four-dimensional asynchronous ensemble square-root filter (4DEnSRF) algorithm and tests with simulated radar data. *Quart. J. Roy. Meteor. Soc.*, **139**, 805–819.

Wheatley, D. M., K. H. Knopfmeier, T. A. Jones, and G. J. Creager, 2015: Storm-scale data assimilation and ensemble forecasting with the NSSL Experimental Warn-on-Forecast System. Part I: Radar data experiments. *Wea. Forecasting*, **30**, 1795–1817.

Wienhoff, Z., H. Bluestein, L. Wicker, J. Snyder, A. Shapiro, C. Potvin, J. Houser, and D. Reif, 2018: Applications of a spatially variable advection correction technique for temporal correction of dual-doppler analyses of tornadic supercells. *Mon. Wea. Rev.*, **146**, 2949–2971.

Wurman, J., Y. Richardson, C. Alexander, S. Weygandt, and P. F. Zhang, 2007: Dual-Doppler and single-Doppler analysis of a tornadic storm undergoing mergers and repeated tornadogenesis. *Mon. Wea. Rev.*, **135**, 736–758.

Yussouf, N., E. R. Mansell, L. J. Wicker, D. M. Wheatley, and D. J. Stensrud, 2013: The ensemble Kalman filter analyses and forecasts of the 8 May 2003 Oklahoma City tornadic supercell storm using single- and double-moment microphysics schemes. *Mon. Wea. Rev.*, **141**, 3388–3412.

Zhang, F., C. Snyder, and J. Sun, 2004: Impacts of initial estimate and observation availability on convective-scale data assimilation with an ensemble Kalman filter. *Mon. Wea. Rev.*, **132**, 1238–1253.

Zhang, Y., F.Zhang, and D. J.Stensrud, 2018: Assimilating all-sky infrared radiances from GOES-16 ABI using an ensemble Kalman filter for convection-allowing severe thunderstorms prediction. *Mon. Wea. Rev.*, **146**, 3363–3381.

Zhang, Y., D. J. Stensrud, and F. Zhang, 2019: Simultaneous assimilation of radar and all-sky satellite infrared radiance observations for convection-allowing ensemble analysis and prediction of severe thunderstorms. *Mon. Wea. Rev.*, **147**, 4389–4409.